Development Of a Novel Multi-disciplinary Design Optimization Scheme For Micro Compliant Devices

by

Mehrnaz Motiee

A thesis

presented to the University of Waterloo

in fulfillment of the

thesis requirement for the degree of

Doctor of Philosophy

in

Mechanical Engineering

Waterloo, Ontario, Canada, 2008

Author's Declaration

I hereby declare that I am the sole author of this thesis. This is a true copy of the thesis, including any required final revisions, as accepted by my examiners.

I understand that my thesis may be made electronically available to the public.

Abstract

The focus of this research is on the development of a novel multi-disciplinary design optimization scheme for micro-compliant devices. Topology optimization is a powerful tool that can address the need for a systematic method to design MEMS. It is expected that systematic design methods will make the design of micro devices transparent to the user and thus spur their use. Although topology optimization of MEMS devices with embedded actuation has received a great deal of attention among researchers recently, there is not a significant amount of literature available on the subject. The limited literature available addresses multi-physics topology optimization, which employs the homogenization method. However, the products of this method inherit the drawbacks of homogenized material discretization, including checkerboard pattern, gray-scale material and narrow flexural hinges in the optimum solution. In this thesis, a new topology optimization scheme is introduced that addresses the specific needs of MEMS domain. A new discretization approach with frame-ground structure is introduced. This approach offers significant conceptual and practical advantages to the compliant MEMS optimization problem, including compatibility with MEMS fabrication processes. The design spaces of compliant mechanisms are non-convex and it is critical to employ an algorithm capable of converging to the global optimum without the need to evaluate gradients of objective function. In this thesis, an efficient real-coded genetic algorithm is implemented, which shows a better repeatability and converges to very similar solutions in different runs. This new method of optimization facilitates the use of a coarse subdivision of the design domain rather than the homogenized material method, for the same resolution of shape definition. Therefore, the topology optimization scheme developed in this thesis significantly reduces the computational burden without compromising the sharpness of the shape definition. As the problem of compliant mechanism design is posed as a set of conflicting objectives, a well-posed multi-criteria objective function is introduced which avoids one objective dominating the solution. Moreover, the formulation is modified to incorporate electro-thermal boundaries and enables the optimization of the compliant mechanisms to transfer maximum motion or maximum force at the output. A number of design examples are used to demonstrate the ability of the procedure to generate non-intuitive topologies. Their performance is verified using ANSYS and compared with results from the homogenization method and designs reported in the available literature.

Acknowledgments

I would like to express my gratitude to and respect for Professors Amir Khajepour and Raafat R. Mansour for their professional supervision and patient guidance during the different phases of my research in addition to their meticulous reading of this thesis and setting me straight when I went wrong. I would like to especially thank them for teaching me the majority of the knowledge I have acquired in the field of MEMS.

I would also like to thank the members of my comprehensive exam and thesis defense committee for their time, support, and constructive comments. Of equal importance are my thanks to Professor Donald. E Griesrson, Professor Patricia Nieva, Professor Siva Sivoththaman and Professor Ridha Ben Mrad.

The financial support of Natural Sciences and Engineering Research Council of Canada is acknowledged.

My thanks to friends, colleagues, officemates and labmates in University of Waterloo for making my graduate studies a joyful journey to remember.

Finally, I would like to thank my parents, Mehrnagiz and Iraj and my brothers, Mehrtash and Mehrdad, for their never-ending support, unconditional love, encouragement, and for making the world a much happier place for me.

Dedications

This thesis is dedicated to the ones who gave me their unconditional love...

the strength and courage...

who are my inspiration in life...

and without them this could not be a reality...

To my beloved parents...

Dr. Iraj Motiee and Mehrangiz Khodayari

Contents

List of Tables

List of Figures

Nomenclature

C_C	bound on the mean compliance
ε	strain tensor
ξ	normalized weight parameter
E	Young's modulus of elasticity
F_{in}	input force
F_d	unit dummy load
σ	stress tensor
σ^d	stress field due to the dummy load
Λ_L	lagrange multiplier
Γ_L	lagrange multiplier
Γ	boundary of design domain
Γ_{ED}	natural electrical boundary condition
Γ_{MD}	natural mechanical boundary condition
Γ_{TD}	natural thermal boundary condition
Γ_{EN}	essential electrical boundary condition
Γ_{MN}	essential mechanical boundary condition
Γ_{TN}	essential thermal boundary condition
GUI	graphical user interface
I	moment of inertia
L	length of the beam
k_s	workpiece resistance
K	stiffness matrix
M	moment due to the actual loading
M^d	moment due to the virtual loading
MSE	mutual strain energy
SE	strain energy
Ω	design domain
SLP	sequential linear programming
FEA	finite element analysis

SQP	sequential quadratic programming
T	temperature
U	nodal displacement vector
u	displacement field
V	voltage
k_e	electrical conductivity
i_E	internal current source per unit volume
$\hat{n}$	unit vector normal to the surface
k_t	thermal conductivity
q_j	heat generation rate per unit volume
F_b	body force
C	elasticity tensor
α	thermal expansion coefficient
$\bar{F}$	traction force at boundary
A	cross section area
λ, μ	Lamė elastic constants
ν	Poison's ratio
δ_{ij}	Kronecker delta function
$\{u^n\}$	local nodal displacements vector
$\{u\}$	global nodal displacements vector
N	interpolation shape function
x_i	design variable
x_{upper}	upper limit on design variable
x_{lower}	lower limit on design variable
t	out of plane thickness
w	in plane width
Δ	direction of output deflection
R_e	equivalent electrical resistance
ρ_0	electrical resistivity
ξ	temperature coefficient of electrical resistivity
I_e	current through element e

MNA	modified nodal analysis
Q_e	internal heat generation in element e
R_a	Raleigh number
g	acceleration due to gravity
δ	vertical spacing between the beam and the substrate
h	convection heat transfer coefficient
f_Q	heat flux vector due to internal heat generation
f_s	heat flux vector due to conduction
f_T	reaction heat flux due to specified temperatures
K_c	conductive thermal stiffness matrix
ε_{th}	thermal strain
ε_m	mechanical strain
F_T	thermal force vector
$\Delta\bar{T}$	average temperature change in the element
P_E	Euler's buckling limit
$\bar{P}$	transverse shear buckling limit
G	shear modulus
Δ_f	filtering factor
MEMS	MicroElectroMechanical Systems

Chapter 1

Introduction

Compliant mechanisms offer great promise in providing new and better solutions to many mechanical-design problems. A compliant mechanism is a single-piece flexible structure in which the structural deformation is utilized to transmit force or deliver motion due to an input actuation. It works as a transmission that is designed to have the desirable characteristics between the input actuation and the output to the environment. Since compliant mechanisms are jointless, they have many desirable features, such as no assembly, no backlash, low cost, and low maintenance.

Compliant mechanisms attain their mobility from flexibility of their constituents as opposed to their rigid-body counterparts, which attain their mobility from hinges, bearings and sliders. The main advantages of compliant mechanisms are that they can be built using fewer parts, require little assembly and need no lubrication [15].

An important application of compliant mechanisms lies in MicroElectroMechanical Systems (MEMS), which cannot be manufactured using typical assembly processes and can not make use of hinges and bearings since friction dominates at small scales. The most common method for MEMS fabrication uses planar layers of material. Surface micromachining uses multiple layers of material that are deposited, then patterned using planar lithography. The constraints introduced by the planar nature of MEMS fabrication and the difficulty of parts assembly in micro-scale introduces a number of challenges in constructing mechanical devices at the micro-level. Compliant mechanisms offer solutions to many of these problems [15]. This field is expected to grow dramatically in the near future. The advantages of compliant mechanisms at

the micro-level are that they:

- can be fabricated in a plane;
- require no assembly;
- require less space and are less complex;
- have less need for lubrication;
- have reduced friction and wear;
- have less clearance due to pin joints, resulting in higher precision; and
- integrate energy storage elements (springs) with other components.

Tests have demonstrated that compliant components can be very robust at the micro-level and often last longer than components that use pin joints or other elements that induce wear. Micro-compliant devices are predominantly utilized at the micro-scale as feasible solutions for the realization of force/motion transmission [3]. Microsensors [16] (e.g. accelerometers for automobile crash detection and pressure sensors for biomedical applications) and microactuators [17] (e.g. for moving arrays of micromirrors in projection systems, for position manipulation of micro-objects and for tuning MEMS filters) are examples of commercial applications of MEMS.

Typical compliant mechanism synthesis involves the use of a homogenization method [18] or of truss/beam ground structures [19] originally seen in structural optimization. These methods can be incorporated with different objective functions to design compliant mechanisms for various purposes, such as compliant grippers for object manipulation [17], compliant motion amplifiers in MEMS [20], and compliant end-effectors for minimally invasive surgery [21].

This thesis addresses the present difficulties in systematic synthesis of compliant micro mechanisms. With a focus on novel applications in MEMS actuator design, existing methods are improved and a new method for the systematic design of micro-compliant mechanisms with multi-physics boundary conditions is introduced.

1.1 Motivation for this thesis

Due to the lack of a systematic design method, typical MEMS design procedures rely on trial and error and are based on designer intuition. Obviously, such structures cannot be optimum and better design methodologies are needed to arrive at optimum design solutions. The feasibility of using Electro-Thermo-Compliant (ETC) devices in microsystems, as demonstrated by many intuitive designs described in the literature [16, 22, 23, 24, 21], drives the need for a systematic method to design these devices. It is expected that systematic design methods will make the design of micro-devices transparent to the user and therefore spur their use.

A method that is able to solve some of above-mentioned problems is the topology optimization method [25]. Any topology optimization process involves discretization of the design domain into elements. The optimization process selectively removes elements from the domain to define an optimal topology for the design objective without relying upon human intuition. It is a powerful method to determine the best design of a structure in a given design domain, for a given loading and output condition.

The possible applications of topology optimization in multi-physics problems are numerous, however one very interesting application is in the systematic design of MEMS [9]. Synthesis of compliant mechanisms for MEMS has typically been based on modifications of rigid-body mechanisms with similar functionality [15]. Although the topology optimization method has been around since 1970 [26], the first applications of topology optimization methods to compliant mechanism synthesis appeared in literature in 1996 [5]. Since then, an increasing number of researchers are working on theoretical development of compliant mechanism and MEMS synthesis algorithms, but there is still not a wide-spread knowledge of the method. This may partly be due to the fact that the programming of a topology optimization code seems to be an overwhelming problem to a newcomer in this field [27]. Because of this, there is a high need to improve the synthesis method and modify the algorithms to address the need of todays research. For instance, in MEMS design, actuation principles for micro-actuators may be thermal, electro-thermal, piezoelectric, electrostatic and many others. Compliant mechanism synthesis procedures must therefore be extended to take such possibilities into account.

Although developing a systematic approach to design optimum MEMS devices has recently received a great deal of attention among researchers, there is not a significant amount of liter-

ature available on the subject. The majority of the literature in this field addresses the single physics problems using force or displacement, as an input similar to optimization of mechanical structures with constraint on structural weight [28, 29, 30, 31, 32]. However, applying mechanical actuation in the micro-domain is not very easy and sometimes impossible. However, the recent developments in theory, computational speed and large-scale optimization algorithms, such as genetic algorithms, allow for extensions of the topology optimization method to problems involving multi-physics and multiple constraints.

The limited literature available addresses the multi-physics topology optimization, which employs the homogenization method [33, 13, 34, 10, 9, 35]. The homogenized material method uses a fictitious material density as the design variable and optimizes the material density at each cubic element [36]. Optimization methods based on homogenized material distribution often produce solutions with checkerboard areas, which cause discontinuity in the material in the final solution. Moreover, the optimum solution consists of several flexural hinges with narrow and long slender sections that are prone to failure. The final topologies resulting from the homogenization method usually need extensive post-processing to filter out the checkerboard pattern and interpret the layout of physical device and therefore, are computationally extensive [37]. Thus a new optimization scheme is required for MEMS compliant devices.

The feasibility of using ETC devices in microsystems, as demonstrated by numerous intuitive designs, drives the need for a systematic method to design these devices [24, 9]. This research is motivated by understanding the critical role of electro-thermo-mechanical compliant mechanisms in MEMS design and the need to develop a topology optimization method which can address the specific problems of MEMS, including enabling multi-physics on-chip actuation and compatibility with available fabrication processes. It is expected that systematic design methods will make the design of electro-thermo-mechanical devices transparent to the user and thus spur their use in MEMS.

1.2 Objectives

This research is focused on the development of a novel multi-disciplinary design optimization scheme for micro-compliant devices, which includes:

- Developing a new, fully coupled analysis method capable of solving multi-physics domains efficiently. The solver addresses the micro-domain physics and the coupled field of the electro-thermo-mechanical domain.

- Employing a new frame ground structure to address the shortcomings of previous methods, which are based on homogenized material optimization, to generate feasible to fabricate designs. The motivation for using the frame-ground structure approach stems from the advantages it brings to the ETC optimization problem. The advantages of frame-ground structure are:

  - It allows for a coarser subdivision of the design domain than the continuum element approach for the same resolution of shape definition. Therefore, the frame-element-based formulation reduces the computational burden for the synthesis procedure without compromising sharpness of the shape definition.
  - The resulting geometry adheres to the original discretization and therefore is clean and easy to fabricate using photolithography-based microfabrication processes.
  - It is not necessary to interpolate thermophysical properties between existing and nonexisting states in the frame ground structure approach, unlike in the material distribution approach. The use of frame element cross section area as the design variable obviates the use of a constitutive model for interpolating electrical and thermal properties as a function of a fictitious density.
  - It helps to model surface heat transfer more easily than the material distribution approach. It is difficult to model surface heat transfer accurately in the continuum element approach because the number, shape, and size of holes are not specified initially as new faces arise and disappear during the iterative optimization procedure. The frame-ground structure approach avoids these difficulties elegantly. The location and length of all the elements are specified in advance. The heat transfer from surfaces is properly accounted for at every step of the optimization process.

- Developing a novel optimization scheme with multi-disciplinary boundary conditions.

The actuation scheme plays an important role in MEMS devices. As mechanical boundaries, such as force and displacement, are not very easy or sometimes impossible to apply in micron dimensions, the compliant mechanism optimization for MEMS devices should be able to account for multi-disciplinary inputs. Electro-thermal is the most commonly used actuation scheme in MEMS. This thesis addresses the extension of compliant mechanism synthesis procedures to take into account the possibility of electro-thermal boundary conditions. The novel optimization scheme includes:

- Implementation of a new element removal policy to impose the MEMS fabrication constraints and lithography tolerances to the optimization procedure and upper and lower limits on design variables.

- Addressing the failure criterion of the optimized designs by imposing new strength constraints on the optimization problem. The goal is to ensure a fully distributed compliance throughout the mechanism and to prevent the appearance of long, slender elements prone to failure and narrow hinges with high stress concentration in the optimized design, which are often seen in lumped compliant design.

- The non-convexity of the design spaces of compliant mechanisms is noted in the literature [38, 39]. The optimization problem is posed as a balance between stiffness and flexibility of the design. When the number of elements and design variables increase, the number of design possibilities increases exponentially and conventional gradient-based optimization techniques can not be used effectively. For some local optima, compliant topologies may either be overly stiff or overly flexible and therefore, do not achieve the desired balance between the two criterion. It is critical therefore, to employ an algorithm capable of searching noisy spaces and converging to global optimum without the need to evaluate gradients of objective function. This is addressed by:

  - Implementing an effective real-coded genetic algorithm with elitism, which shows a better repeatability i.e. it converges to very similar solutions in different runs, compared with Sequential Linear Programming (SLP) or Sequential Quadratic Programming (SQP), in which the solutions are strongly dependent on an initial guess [19].

  - Introducing a multi-criteria objective function to address the current difficulties in behavior of objective functions. The goal is to avoid one objective dominating the solution [27].
  - Improving the formulation to provide the option to design the compliant mechanisms specifically for transfer of maximum motion or maximum force at the output.

- Designing a user friendly Graphical User Interface (GUI) for the optimization scheme to make the developed method available to the MEMS design community.

1.3 Outline of the dissertation

Following the motivations and objectives given in Chapter 1 of this thesis, Chapter 2 presents an overview of the different methods available for synthesis of compliant mechanisms and the limitations of these methods. Different discretization methods and solution techniques described in the literature are reviewed and their shortcomings are highlighted. The necessity of developing a new optimization scheme for MEMS applications is emphasized.

Chapter 3 introduces the general problem. A modified objective function and a custom coded genetic algorithm are introduced to address the convergence and computational cost difficulties. Also, frame-ground structures are verified as a suitable solution to generate feasible to fabricate optimal designs for MEMS. A base optimization scheme with GUI and compatible with specific needs of MEMS applications is developed. The superiority of the optimization scheme is validated by comparing its results with examples from the available literature. This optimization scheme serves as a basis for extending the proposed synthesis method to multi-disciplinary domains.

In Chapter 4, the extension of the optimization scheme continues with the development of a new analysis method for micro-electro-thermo-mechanical domain. A new, fully coupled formulation is developed, which sequentially solves electrical, thermal and thermo-elastic domains. An algorithm is proposed that builds a resistive circuit model of electrical domain with Modified Nodal Analysis (MNA) and effectively couples its matrix equations to a finite element model of thermo-elastic domain. The finite element analysis (FEA) includes the micro-physics effects and is implemented in a complete package with GUI. This FEA serves as the main solver

in the optimization scheme. The performance and accuracy of the proposed coupled FEA is verified with examples.

In Chapter 5, the topology scheme is extended to multi-physics domain, employing the finite element solver developed in Chapter 4 as the core solver. Since the design variables can have any real value inside the bounds, the solution technique is further improved by a real-coded genetic algorithm. The complete optimization package includes a GUI, postprocessing option and a filtering scheme to impose the MEMS fabrication limits and lithography tolerances on the optimal solution. Also, a new buckling constraint is introduced and implemented in the scheme that effectively generates optimum solutions with strength considerations.

In Chapter 6, examples of optimized actuators resulting from the optimization scheme are presented and verified. The result of this optimization package is verified by comparing its results with examples from the literature and simulations in ANSYS.

Chapter 7 concludes the thesis, highlights the contributions and discusses the future research expansions.

Chapter 2

Background and Literature Review

In this chapter, the current research in systematic synthesis of compliant mechanisms is reviewed and the difficulties are addressed.

2.1 Compliant Mechanisms

Compliant mechanisms are mechanical devices that rely on elastic deformation to achieve force and motion transmission. compliant mechanisms are joint-free monolithic substitutes for multi-membered rigid-body mechanisms. Compliant mechanisms derive their name from the fact that they achieve mobility, at least in part, through compliance, i.e. elastic deformations of one or more links or joints, rather than exclusively through relative motion at joints, as in traditional rigid-link mechanisms. Compliant mechanisms function as a synergistic combination of a structure and a mechanism, or as a structure with mobility.

Compliant mechanisms are important in mechanical design because they offer distinct advantages over conventional rigid-link mechanisms. An advantage of a compliant mechanism is the potential for a dramatic reduction in the total number of parts required to accomplish a specific task. The reduction in number of parts may reduce manufacturing and assembly time and cost. Compliant mechanisms also have fewer movable joints, such as pin and sliding joints; this results in reduced wear and need for lubrication. These are valuable characteristics for applications in which the mechanism is not easily accessible, or for operation in harsh environments that may adversely affect joints. Reducing the number of joints can also increase mechanism

precision, as backlash may be reduced or eliminated. It is also possible to realize a significant reduction in weight by using compliant mechanisms rather than their rigid-body counterparts. This may be a significant factor in aerospace and other applications. Another advantage of compliant mechanisms is the ease with which they are miniaturized. Simple microstructures, actuators, and sensors are experiencing wide usage, and many other MEMS show great promise. The reduction in the total number of parts and joints offered by compliant mechanisms is a significant advantage in the fabrication of micromechanisms [15]. As flexure is permitted, compliant mechanisms can be readily integrated with non-mechanical actuation schemes, such as thermal and electro-thermal effects.

Due to the many advantages they offer, the field of compliant mechanisms has received a great deal of attention in recent years. Compliant mechanisms have been designed for shape reconfiguration in aerodynamic applications, such as aerofoil adaptive mechanisms, where a flexible member adapts a desired shape for specific loading [40]. They find numerous applications in product design as compliant clutches [41] and fishing pliers [17]. Compliant parallel guiding mechanisms [42], constant force mechanisms [43], single piece staplers [44], disk drive loading mechanisms [45], and mechanisms with bistable behavior [46] are some notable examples where flexibility in members is desired for special objectives. As friction and backlash losses are negligible, compliant mechanisms are ideal for high precision instrumentation [47].

2.1.1 Lumped versus distributed compliance

Compliant mechanisms can be classified into several categories. The main classification, as described in [48], is that of fully compliant versus partially compliant. A partially compliant mechanism employes rigid-body joints, rigid members and elastically deforming flexible members for accomplishing a force/motion transmission task. A fully compliant mechanism on the other hand, uses only the preferred elastic deformation of its flexible members; they have no rigid-body joints. Fully compliant mechanisms are preferred where assembly part manufacturing is difficult and friction is dominant, e.g. in MEMS applications.

Compliant mechanisms may also be classified as non-monolithic and monolithic or lumped and distributed.

In lumped compliant mechanisms, the flexibility is concentrated in localized areas, usually

at flexural hinges. A compliant mechanism with a discrete number of flexural pivots is said to possess lumped compliance. The drawback with flexural joints include high stress concentration, low static and fatigue strength, and difficultly in manufacturing very thin and thick sections. Lumped compliance can cause high stress concentrations at the flexural hinges. These areas of high stress are prone to fatigue and/or failure.

In distributed compliant mechanisms, the flexibility is not concentrated in specific areas, but is distributed throughout the mechanism over a range of segment. The mechanism as a whole is flexible and there are no joints; it is a monolithic fully compliant mechanism. Such mechanisms are called fully compliant mechanisms with distributed compliance. Distributed compliance should offer superior performance and reliability compared to lumped compliance because deformation is not concentrated in a few regions; stress concentrations are therefore avoided.

In distributed compliance mechanisms, it is the topology and shape of the material continuum that give these mechanisms the ability to deform and, therefor, the motion and the force transmission capability. Compliant mechanical devices can provide distinct advantages over conventional rigid-link devices; however, including compliance complicates the design process. The design of monolithic electro-thermo-mechanical artifacts, based on the topology synthesis of compliant mechanism with distributed compliance, is the primary focus of this research.

2.1.2 Micro-Compliant Mechanisms

Compliance in design leads to jointless, no-assembly, monolithic mechanical devices and is particularly suited for applications with small range of motions. Although simple deformable structures, such as beams and diaphragms, have performed adequately in many micro-devices, more sophisticated micromechanical functions can be realized by fully exploiting the preferred use of elastic deformation via compliant mechanisms. The small scale and high aspect ratio of micromechanical structures makes them inherently flexible. Therefore, in MEMS, a compliant design that needs no assembly is not merely a prudent choice, it is a necessity [21].

In recent years, several applications of compliant mechanisms in MEMS have been introduced. Single piece devices can be used in motion sensing as accelerometers [16], gyroscopes [22] and as micro-actuators for position manipulation of micro objects [23]. Compliant mechanisms

have also been designed for displacement manipulation tasks, such as displacement amplifiers [24] and inverters [49].

Micro-actuators that are responsible for movement play a crucial role in MEMS. Electro-thermo-compliant (ETC) microdevices provide arbitrary in-plane displacements through non-uniform Joule heating by virtue of their specially designed topology and shape. In addition to the advantages of embedded actuation, large forces and displacements, and ease of microfabrication, one more attractive feature of ETC devices is their suitability for systematic synthesis directly from behavioral specifications [9].

In MEMS design, since electro-thermal actuation is a very common actuation principle, compliant mechanism synthesis procedures must be extended to take such possibilities into account. Design of ETC for MEMS is a new era in topology optimization and no effort to include electro-thermal actuation into existing topology optimization schemes with discrete ground structure has been reported in the literature to date.

2.1.3 Background of compliance theory

In compliant mechanisms, flexibility and deflections are of utmost concern. This section discusses a useful method to determine the deflections of structural systems. This method is used in the compliant mechanism design problem formulation.

Unit dummy load method

The "*unit dummy load*" method is based on the principles of virtual work, where a special case of the principle of virtual forces is used to evaluate the displacements of a deformable body. Specifically, the value of the displacement of a deformable body at a particular point can be determined by applying a fictitious or "dummy" load at that point in a particular direction. The magnitude of this force is arbitrary, so for simplicity it is assumed unity. It is for this reason that the procedure is called the unit dummy load method. A general statement is given as follows [50]:

" The true displacement Δ_i of a point i in a deformable body in a given direction is equal to the integral over the volume of the body of the product of the true strains, ε and the virtual stresses produced by a unit virtual force at i in the direction of Δ_i. Physically, Δ_i is a measure

of the flexibility of the structure."

In mathematical terms:

$$\Delta_i = \int_V \varepsilon \sigma^d dV \tag{2.1}$$

where ε is the true strain field and σ^d is the virtual stress due to the dummy load.

For example, consider a linear elastic beam with negligible shear deformation. To determine the beam deflection at a particular point, a unit dummy load is applied at the point of interest, and the resulting moment distribution due to this loading is calculated. The deflection at the point of interest is given by [25]:

$$\Delta = \int_0^L \frac{M M^d}{EI} dx \tag{2.2}$$

where Δ is the deflection at desired point, L is the length of the beam, M is the moment due to the actual loading, M^d is the moment due to the virtual loading, E is the modulus of elasticity, and I is the area moment of inertia of the cross section.

Beam Design for Required Deflection

The unit dummy load method has been used in conjunction with optimal design methods for problems in which the goal is to achieve the minimum weight design with a specified deflection at a certain point [51], [26]. These types of optimal design problems can be called "design for required deflection" problems. This design for required deflection problem was considered for a linear elastic beam by Barnett [51] and Shield and Prager [26]. This beam problem provides valuable insight into the requirements for compliant mechanism design problem. Consider a simply supported linear elastic beam, as shown in Figure 2-1. The objective is to predict the optimal beam width that minimizes the material volume while achieving the specific deflection Δ at point x^* when subject to the loading $P(x)$. In this case, the topology (a single segment) and shape (a straight line) are known, and it is the size that is optimized. The optimization

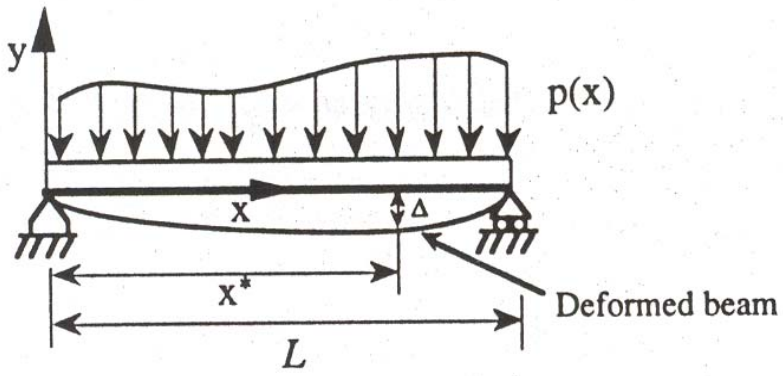

Figure 2-1: Design of a beam for specified deflection.

problem then is [25]:

$$\begin{aligned} Minimize \quad &: \quad Volume = \int_0^L A(x)dx \\ subject\ to \quad &: \quad \Delta = \int_0^L \frac{M(x)M^d(x)}{EI(x)}dx \\ &\qquad \text{equilibrium equations for } M \text{ and } M^d \end{aligned} \tag{2.3}$$

Assuming that the beam has a rectangular cross-section with constant height, h, the problem can be written as follow where, $I(x) = \varrho A(x)$ and $\varrho = \frac{h^2}{12}$:

$$\begin{aligned} Minimize \quad &: \quad Volume = \int_0^L A(x)dx \\ subject\ to \quad &: \quad \int_0^L \frac{M(x)M^d(x)}{E\varrho A(x)}dx - \Delta = 0 \end{aligned} \tag{2.4}$$

Using the calculus of variation and Lagrange multipliers, the unconstraint optimization problem is [25]:

$$Minimize : \pounds(A(x), \lambda) = \int_0^L A(x)dx + \lambda \left(\int_0^L \frac{M(x)M^d(x)}{E\varrho A(x)}dx - \Delta \right) \tag{2.5}$$

The optimal distribution of the cross-section is:

$$A^*(x) = \frac{1}{E\varrho\Delta}\left(\int_0^L \sqrt{M(x)M^d(x)}dx\right)\sqrt{M(x)M^d(x)} = \frac{1}{E\varrho}\sqrt{\Lambda_L M(x)M^d(x)} \tag{2.6}$$

where Λ_L is the Lagrange Multiplier and $\frac{1}{\Delta}\int_0^L \sqrt{M(x)M^d(x)}dx = \Lambda_L^{1/2}$ is a constant.

Notice that when the quantity $M(x)M^d(x)$ becomes less than zero anywhere in the design domain, the value of $A^*(x)$ will be imaginary and there is, therefore, no solution. This implies that the design problem is not well posed. One way to solve this problem is to introduce a constraint on the mean compliance. The *mean compliance* or stiffness of a linearly elastic structure is defined as the work done by the applied loads on the displacements they produce [26]. This constraint for a beam is shown as:

$$\int_0^L \frac{M^2(x)}{E\varrho A(x)}dx - C_C = 0 \tag{2.7}$$

and in Lagrangian form as:

$$\Gamma_L\left(\int_0^L \frac{M^2(x)}{E\varrho A(x)}dx - C_C\right) = 0 \tag{2.8}$$

where Γ_L is the Lagrange Multiplier and C_C is the bound on the mean compliance. With the addition of this constraint to Equation (2.4), the optimal beam cross section is:

$$A^*(x) = \frac{1}{E\varrho}\sqrt{\Lambda_L M(x)m(x) + \Gamma_L M^2(x)} \tag{2.9}$$

The Lagrange Multipliers Λ_L and Γ_L, both non-negative, can be found from the two constraints. By choosing an appropriate value for C_C in Equation (2.7), the value of Γ_L can be controlled, thereby avoiding a situation where there is a negative quantity underneath the square root sign. Therefore, a solution is guaranteed for any load condition.

As this beam example illustrates, including a deflection constraint alone is not sufficient for design for required deflection problems. An additional constraint on the mean compliance or "stiffness" is necessary to guarantee a well-posed problem. The physical interpretation of

this notion is that both the flexibility (deflection constraint) and stiffness (mean compliance constraint) must be considered simultaneously [19].

The next section discusses a method in which control over the deflection or flexibility is incorporated with control over the stiffness in the design of compliant mechanisms, which leads to a multicriteria formulation.

2.2 Review of Compliant Mechanism Design

An introduction and a historical background of topology optimization can be found in the book by Bendsoe [36]. Topology optimization is a method to find the best design of a structure in a given design domain Ω, for a given loading and output condition.

In general, closed-form analytical solutions are not possible for irregular geometries. Therefore, these equations are solved using numerical methods such as finite element method, finite difference method, boundary element method, chain algorithm and so on. In this thesis, the finite element method is used when the design of compliant mechanisms is considered.

Two main approaches have been developed thus far for systematic synthesis and design of compliant mechanisms. The first is *kinematics based* or the *pseudo rigid-body model* approach, wherein a compliant mechanism is presented by an equivalent rigid-link mechanism, which can be synthesized using well established kinematic techniques. The second is the continuum based approach, which employs structural optimization techniques to determine a suitable topology, shape and size of a compliant mechanism for desired specifications. These approaches are described in the following sections.

2.2.1 Methods based on rigid-link mechanisms

The elastic deformation in a compliant mechanism can be limited only to a small portion as in mechanisms with flexural hinges. Such mechanisms are called lumped compliant mechanisms and they can be analyzed and designed using rigid-body kinematic techniques.

The kinematic approach for synthesis and design of compliant mechanisms involves methods developed by Midha and his associates [15]. The purpose of the pseudo rigid-body model is to provide a simple method for analyzing systems that undergo large, nonlinear deflections. The

pseudo rigid-body model concept is used to model the deflection of flexible members using rigid-body components that have equivalent force-deflection characteristics. Rigid link mechanism theory may then be used to analyze the compliant mechanism.

Different types of segments require different models. Pseudo rigid-body models have been derived for flexural pivots [52], straight slender beams with tip forces [53] and initially curved beams with tip forces [54]. In [55] a pseudo rigid-body model for cantilever beams with tip loads comprising positive end moments is developed. For each flexible segment, a pseudo rigid-body model predicts the deflection path and force-deflection relationships. The motion is modeled by rigid links attached at pin joints. Springs are added to the model to accurately predict the force-deflection relationship. The key for each pseudo rigid-body model is to decide where to place the pin joints and what value to assign the spring constant [15]. This method begins with a known rigid-link mechanism and an iterative process generates an appropriate compliant mechanism design. Further study of rigid-link compliant mechanisms is out of the scope of this thesis, since the focus is on topology optimized MEMS structures with distributed compliance throughout the structure.

2.2.2 Methods based on structural optimization

The region in which the mechanism to be designed must fit is called the design domain. The design domain is modelled by a ground structure. The ground structure can be discretized by different kinds of finite elements, e.g. continuum, truss and beam elements. Only the most vital members are retained to optimize with respect to prescribed loadings and performance criteria. In the ground structures, the height, the thickness or the area of the element can be chosen as the design variable. The unique feature of this design method is that optimal solutions of compliant mechanisms can be generated automatically to obtain the desired input-output behavior and the mechanism topology is not known in advance.

Ananthasuresh [56] and colleagues [57, 58, 59] developed a methodology for the synthesis of compliant mechanisms with distributed compliance using continuum mechanics and a structural optimization technique called the homogenization method. The homogenization method is a numerical optimization technique originally developed by Bendsoe and Kikuchi [18] to obtain topologies for the stiffest possible structures to satisfy given boundary conditions and resource

constraints. In adopting this technique for compliant mechanisms, the formulation of the original objective in the homogenization was the key issue in the synthesis approach developed by Ananthasuresh [56].

Frecker and colleagues [5, 19, 1] extended the topological synthesis work of compliant mechanism by modifying the objective expression in the multicriteria model attempted by Ananthasuresh [56]. Furthermore, to improve the convergence of optimization routine, two more modifications were implemented: (a) use of an initial design domain compromising a framework of truss elements, wherein every node in the structure is connected to every other node instead of a continuum domain used in [56], and (b) initiation of the optimization by biasing the design variables such that the initial guess topology is that of a rigid link mechanism suitable for the task on the basis of kinematic design intuition. The continuum mechanics approach for design of compliant mechanisms was later explored by Sigmund [49] and Larsen [60] by modifying the design objective of the optimization scheme.

Over the past two decades techniques for both continuum and discrete ground structure topology optimization have been actively investigated. Is either method clearly superior to the other for design of compliant mechanisms? What are the relative strengths/weaknesses of the two approaches?

In this thesis, a discrete ground structure which consists of beam elements with rectangular cross sections is chosen. The beam elements can transfer both longitudinal forces and bending moments and the beams are connected by stiff joints; therefore the optimized structure ends up being a frame.

There are several reasons for choosing a ground structure consisting of discrete beam elements in this thesis instead of continuum elements. The most important advantage of this method is that it produces structures which are feasible for MEMS fabrication. The main disadvantage is that when the number of members and discrete design variable values increases, the number of design possibilities quickly increases towards infinity. Consequently, only problems with coarse node distributions and few sectional possibilities can currently be solved. This problem is addressed by adopting evolutionary algorithms to search for a global optimum. Continuum based solutions sometimes generate a checkerboard problem, which causes a discontinued distribution of material in the final solution. Also, sometimes the optimum solution

consists of several flexural hinge-like regions with narrow sections and high stress concentrations. Discrete type solutions allow modelling of cross-sections, which are more suitable for MEMS applications. The resulting structures from discrete optimization need no interpretation or post-processing and can be directly mapped for fabrication.

The conclusion is that discrete methods seem more naturally suited to MEMS compliant structures using beam/frame type structural members.

2.3 Review of discrete topology optimization methods for mechanical domain

Figure 2-2(a) shows the optimization domain Ω with mechanical boundary conditions at input and output ports. In Figure 2-2 P_1 is the point of application of the input force F_{in}, and Δ_{out} is the direction of desired output deformation at output point P_2. An analytical expression for Δ_{out} is obtained by applying a virtual force at the point of interest P_2 along the desired direction. This unit dummy load is denoted by F_d and is shown in Figure 2-2(b) for a general design domain subject to F_{in} at point P_1 and some specified mechanical boundary conditions.

The general problem statement is:

$$\begin{aligned} Maximize \quad &: \quad \Delta_{out} && (2.10) \\ subject\ to \quad &: \quad \text{lower and upper bounds on design variables} \\ &\quad\ \ \text{flexibility constraints} \\ &\quad\ \ \text{stiffness constraints} && (2.11) \end{aligned}$$

Now it is important to obtain analytical measures for flexibility and stiffness of the domain subject to applied force and boundary conditions.

2.3.1 Flexibility requirement

To facilitate the use of variational calculus, the virtual work principle is employed to compute the output displacements as the mutual strain energy. The unit dummy load method is used to specify the deflection at a particular point, which serves as a measure of the flexibility.

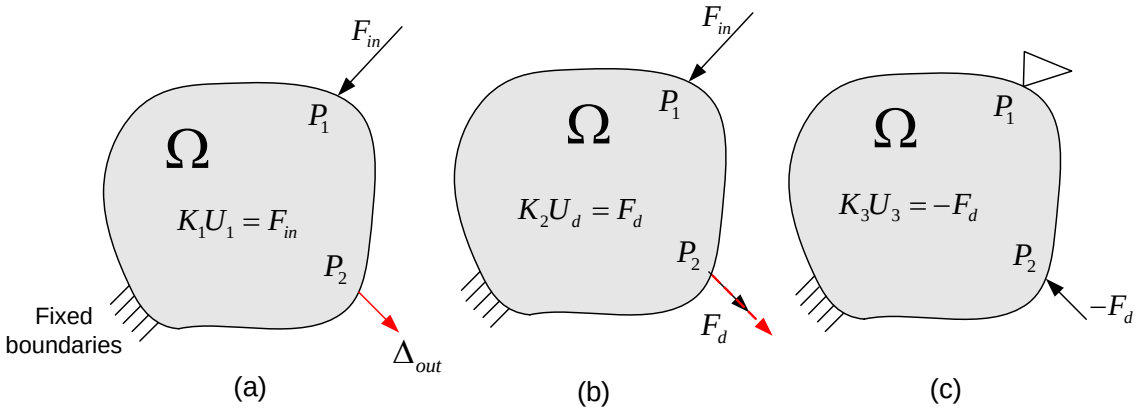

Figure 2-2: (a) Design domain Ω with input force and desired output direction Δ (b) set of loading for measure of flexibility, MSE and (c) set of loading for measure of stiffness, SE.

The output deflection can be expressed as the "mutual strain energy" MSE. Maximizing the deflection at boundary P_2 in the direction of Δ is equivalent to maximizing the MSE at port P_2. For given design specifications, from Equation (2.1) [19]:

$$MSE = \Delta_{out} = \int_{\Omega} \varepsilon \sigma^d d\Omega \tag{2.12}$$

where ε is the strain field when only the actual input force is applied and σ^d is the stress field in the continuum when only the unit dummy load is applied.

The concept of mutual strain energy, MSE, was proposed in [51], [26] and [61], and is simply the mutual energy of a structural system resulting from two sets of loadings. Assuming that the problem is linear elastic, the continuum can be approximated using a finite element model. In such a set up:

$$MSE = F_d U_1 = U_d^T K_2 U_1 \tag{2.13}$$

where K_1 is the global symmetric stiffness matrix, U_1 is the nodal displacement vector due to F_{in}, $K_1U_1 = F_{in}$ and U_d is the nodal displacement due to the dummy load F_d, as seen in Figure 2-2(b), and $K_2U_d = F_d$. The maximization of output displacement is posed as a maximization

of the MSE:

$$\begin{aligned} Maximize &: MSE = U_d^T K_2 U_1 \\ subject\ to &: K_1 U_1 = F_{in} \\ &\quad K_2 U_d = F_d \end{aligned} \tag{2.14}$$

2.3.2 Stiffness requirement

Now the stiffness requirements need to be imposed on the design. Control over the stiffness of the structure is equivalent to control over the mean compliance. The principal of virtual work states that if the point of interest is given a virtual displacement in the direction of load, the position of all the other loads (P_1) must be considered fixed. The point P_1 is considered fixed and the load F_d is applied at point P_2 in the opposite direction of Δ as shown in Figure 2-2(c). Maximizing the stiffness of the structure is equivalent to minimizing the Strain Energy SE throughout the domain [19]:

$$SE = \frac{1}{2} \int_{\Omega} \varepsilon \sigma d\Omega \tag{2.15}$$

where σ is the stress field due to the actual input force. In finite element form:

$$\begin{aligned} Minimize &: SE = \frac{1}{2} U_3^T K_3 U_3 \\ Subject\ to &: K_3 U_3 = -F_d \end{aligned} \tag{2.16}$$

where U_3 and K_3 are the nodal displacement vector and stiffness matrix, respectively, resulting from this set of loading, as shown in Figure 2-2(c). Now that the two criteria are modelled in terms of potential energies, they must be combined in some way. In the following section, the proposed multicriteria objective functions described in the literature are reviewed.

2.3.3 Review of multi-criteria objective functions

For topology synthesis of compliant mechanisms, Ananthasuresh et. al. [59] have posed the deformation requirements as maximizing the displacement at the output port along a given direction. Linear elasticity and small deformation theories are used for function evaluation.

Strain energy, which is inversely proportional to the stiffness of the mechanism, is simultaneously minimized to enable the mechanism to sustain loads. The two objectives are mutually complementary, i.e. an increase in the output deformation results in lowering the overall stiffness of the compliant continuum and vice versa. To obtain an optimum balance between the flexibility and stiffness objectives, based on the notion that a compliant mechanism needs to satisfy the flexibility (MSE) and the stiffness (SE) requirements simultaneously, a flexibility-stiffness multicriteria formulation was proposed in [56] and [59]. This formulation involves maximizing their weighted linear combination using the optimality criteria approach, as described by:

$$Maximize : \xi MSE + (1 - \xi)SE \tag{2.17}$$
$$0 \leq \xi \leq 1$$

where ξ is a user-specified control parameter that assigns relative weights to the two objectives. Quite often in this formulation, the orders of magnitude of the two objectives may not be comparable and one of the objectives may dominate the other. This effect can be compensated for by choosing an appropriate weighting factor, which may vary from one problem to another. In general, choosing a value of the normalized weight, ξ, in the global sense is very difficult.

One way to avoid problems of selecting parameters in linear combinations is by using a ratio. An alternative multicriteria objective of maximizing the ratio of the mutual strain energy (the output displacement of the mechanism) and the strain energy (the stiffness between the input and output port) was proposed in [19, 1], with a Sequential Linear Programming (SLP) approach and a truss ground structure. In other words,

$$Maximize : \frac{MSE}{SE} \tag{2.18}$$

Also, in [62] the two criteria were posed as a ratio; however, the homogenization approach was also used and expanded the formulation for plural multi-flexibility cases. This multicriteria objective improves the convergence behavior in optimization. This problem formulation results in mechanisms optimized for efficiency (i.e. minimum input energy lost in the mechanism); however, the formulation gives no control over output/input behavior, such as geometrical or mechanical advantages. For example, it is not possible to specify whether a mechanism should

produce a force or a displacement amplification. In this regard, it should be noted that later in [63] a more sensible objective function, including geometrical and mechanical advantages, has been defined. The latter formulation has been applied to shape design of mechanisms.

The energy-based multicriteria function proposed in [64] uses the ratio of squared output displacement and the strain energy. This work employs Sequential Quadratic Programming (SQP) as the optimization routine. The notion here is that a compliant mechanism can reconfigure itself to deliver maximum available energy at the output port while storing minimum energy within its deformed continuum. Mathematically, the energy based objective can be posed as:

$$Maximize : sign(MSE)\frac{\frac{1}{2}k_s MSE^2}{SE} \tag{2.19}$$

where k_s is a spring at output port that models the resistance or contact at output and $\frac{1}{2}k_s MSE^2$ is the energy stored in the output spring k_s. The term, $sign(MSE)$ is introduced to restore the direction of the output deformation, which is lost in the squared term in the numerator.

While past work has provided much insight into fundamentals for designing compliant mechanisms, the main drawback of these approaches is that the flexibility of a structure is theoretically unbounded. Formulations that maximize flexibility have been shown to be ill-formulated for compliant mechanism optimization [65]. As a solution, stress constraints were employed to count for failure modes in [66]. In this thesis, realizing that the stiffness objective may yield overly stiff topologies and that it may also be inadequate to model the failure criteria directly, a buckling instability constraint is employed while maximizing the output displacement. This proposed formulation with buckling constraint prevents long slender beams in final optimized solutions and addresses the strength of the solution, which is a major concern in the current methods.

2.3.4 Review of ground structures

Since the most common element used in the literature is truss elements, theories and existing approaches to truss-ground structure optimization are reviewed here. In [67], Kirsch and Rosvany pointed out that truss structures by their very nature are most suitable for topology optimization problems. They comment on a truss structure:

"*It possesses unusually many nodes and elements that can be deleted or retained without affecting the functional requirements. In addition, a truss is a relatively simple yet nontrivial structure. It is therefore an ideal system for the investigation of some properties and characteristics associated with optimal topologies.*"[67]

Although truss elements can support only tension and compression modes of loading, they were chosen by many researchers as finite elements because of their simplicity [19, 5, 1].

Frecker, in [19], noted that it is very important to incorporate bending modes of loading when modelling compliant mechanisms. In [19] and [68], it is noted that a sufficient number of truss elements must be used to indirectly account for the mechanics of bending. For instance, a pair of truss elements can simulate a beam in bending, where one element acts as the portion of the beam in tension, and the other beam acts as the portion of the beam in compression. Certain shortcomings were found with this approach, as described below:

1. In a truss ground structure, the needs of individual truss elements are constrained from x and y displacements but are free to rotate at the joints. Therefore, when a truss ground structure is the reference structure, the resulting compliant mechanisms tend to have relatively thinner segments at the joints. This will result in lumped compliance and higher stress distribution at the joints.

2. Because the function of a compliant mechanism relies on bending of constituent elements, it is more natural to employ beam elements than truss elements. Although two truss elements do simulate the bending of a beam, use of beam elements more directly mimics the function of a compliant mechanism.

3. The results from two different reference structures may look similar, however, the deformation mechanism is totally different. In a compliant mechanism based on a truss element ground structure, the motion is generated from deflection at the joints as well as deformation of the elements. In a compliant mechanism based on a beam-element ground structure, however, the motion is generated from the deformation of elements alone, regardless of the extent of deflection.

4. In practice, truss ground structure results in large number of nodes and elements for accurate analysis of compliant mechanisms. Also elements are overlapping each other

which makes the solutions infeasible to fabricate through planar fabrication.

The conclusion is that frame ground structures are more naturally suited to topology optimization of micro compliant structures.

2.3.5 Review of Solution Techniques

The sequential linear programming (SLP) and sequential quadratic programming (SQP) methods for constrained optimization are the most popular methods used for multi-criteria topology optimization problems. Generally, the topology of the optimal solution is dependent on the starting point and/or the value of the constraints, indicating that there are several possible solutions or local maxima. Further, the design objective, which is a ratio of two convex functions, is not itself a convex function. One can conclude, therefore, that there are many solutions for this problem, and that the solution obtained by starting with an unbiased initial guess is not unique. SQP provides a faster convergence; however, considering the fact that objective function is a ratio of two convex functions, it may not be adequately approximated by a quadratic function. On the other hand, SLP provides a conservative approximation to the objective function and requires many algorithm iterations. Also, in discrete optimization, when the number of members and discrete design variable values increases, the number of design possibilities quickly increases towards infinity.

Despite their computational efficiency, calculus-based optimization procedures ([69, 70]) have two primary shortcomings. First, they require the design variables to be continuous. This is because they rely on the gradient information to guide their search towards an optimal solution. Second, they are sensitive to an initial guess and quite often converge to a nearby local optimum. Evidently, for optimization problems that require the variables to be strictly discrete, calculus-based search procedures are unsuitable. An alternative is to employ procedures that rely only on the zero-order function information.

Also, for problems where design spaces are non-convex and where some local optima may not be acceptable, gradient-based algorithms may not be a good choice. In the case of compliant mechanisms, Saxena and Ananthasuresh [38, 39] have demonstrated the non-convexity of the design spaces. For some local optima, compliant topologies may be either overly stiff or overly flexible and, therefore, do not achieve the desired balance between the two. It then becomes

necessary to choose a procedure that is capable of converging to a global optimum as well.

Genetic algorithm [71], a stochastic approach, meets the aforementioned requirement and, therefore, can be applied in the topology design of compliant mechanisms with discrete finite element parametrization. A genetic algorithm simulates nature's mechanism of natural selection and survival of the fittest and is inherently parallel, dealing with a large number of solutions simultaneously, as opposed to the hill-climbing approaches that employ a point to point search. This gives the algorithm the ability to search noisy spaces comprising local optima and subsequently employs the payoff or fitness values to guide its search towards the global optimum.

In this thesis, genetic algorithms are developed to solve the stated optimization problems. The genetic algorithm (GA) is beneficial, as the design spaces for compliant mechanisms are often multi-modal.

2.4 Topology optimization methods for multi-physics domains

In recent years, applications of topology optimization for MEMS design have received a great deal of attention from researchers. However, the majority of the research focuses on improving the homogenization method for a single-physics case of mechanical domain [28, 29, 30, 31, 32].

Structural optimization techniques have only recently been applied to automate multi-physics, micro-compliant mechanism design and there is not a significant amount of literature available on the subject. The previous research involves employing the homogenization method or distributed material method. The idea was first introduced by Sigmund [33] and followed by him using homogenization method [13, 34, 10]. Also, topology optimization of thermally and electro-thermally actuated compliant micromechanisms has been addressed using a modified form of the homogenization method [9, 35] and some numerical examples were presented. However, the presented method contains the addressed difficulties and disadvantages of homogenization method.

Topology optimization with homogenization method does not provide any control over minimum length scale of the optimized design. In [14], fabrication yield of topology optimized electro-thermal actuator with homogenization method was studied. It is shown that the major hurdle in applying the topology optimization method in MEMS design is the difficulty to control

production yield rate. The production yield rate is primarily related to the minimum length scale of the optimized layout by the topology optimization. The success yield was reported to be less than 10% in [14]. The failure was mostly due to residual stress developed during the MEMS process, especially prevalent at the narrow thin parts of the actuator. From the failed results it was concluded that design optimization targeted only at performance hardly produces actuators at a high yield rate. Therefore, it is needed to consider the issue of production rate either directly or indirectly in design optimization process. If a design optimization method can consider all MEMS design issues such as failure criterion and manufacturabilty, the actuator failure rate can be substantially reduced [14]. However, to our knowledge, no such method is yet available, so far. A frame ground structure can effectively address this problem since the design variables are the dimensional length scales of the domain, e.g. in plane width of the elements. Moreover, using frame elements allows to directly address the failure criterion and manufacturability of the design.

Discretized domains are the best suitable solution when the target is a micro-domain. To the best knowledge of author, discrete optimization of multi-physics domain has not been addressed in the literature to date and is in the main objective of the research in this thesis.

2.5 Conclusions

In this chapter, compliant mechanisms were introduced along with a review on history of compliance theory. The advantages and applications of compliant mechanisms were listed and the need for use of compliance in MEMS design was explained.

It was highlighted that the focus of this thesis is to improve the existing topology optimization methods for mechanical structures by proposing a new optimization formulation and employing evolutionary algorithms to overcome the convergence difficulties addressed in the literature. Moreover, utilization of the improved optimization method for micromechanical applications by incorporating MEMS limits and concerns in the scheme may produce devices which are feasible to fabricate through available MEMS planar micromachining technologies. Since MEMS structures are multi-disciplinary in nature, it is necessary to extend the topology optimization to multidisciplinary domains for microelectromechanical structures and to improve

the optimization statement and solution techniques for the specific needs of a multi-disciplinary domain (e.g. preventing long slender elements in the final solution by considering buckling constraints in optimization statement).

In the next chapter, an improved objective function for topology optimization of mechanical micro-actuators is proposed and implemented using genetic algorithms. The results are compared with the available literature and demonstrate the superiority of this new scheme over existing methods.

Chapter 3

Discrete topology optimization with evolutionary algorithms

In this chapter, the general coupled governing equations of a multi-physics domain are presented and the specific case of micromechanical domain is studied. An improved objective function is proposed for the topology optimization of micromechanical actuators. The design domain is discretized using a frame-ground structure. A binary coded genetic algorithm is developed to solve the optimization problem. A GUI is designed to ease the trace of the optimization results. Several numerical examples are compared with topologies reported in the available literature; these comparisons confirm the superiority of the new optimization scheme over the current methods described in the literature.

3.1 General Multi Physics Domain

The region in which the mechanism to be designed must fit is called the design domain. The design domain can be discretized by different kinds of finite elements, for example, continuum, truss and beam elements.

In Figure 3-1 the general design domain Ω with multi-disciplinary boundary conditions is shown. The material is distributed in the gray area and the white area refers to void areas of the domain. In the figure, Γ is the boundary of domain Ω ,where the subscripts E, T and M refer to electrical, thermal and mechanical type boundary conditions, respectively, and subscripts D and

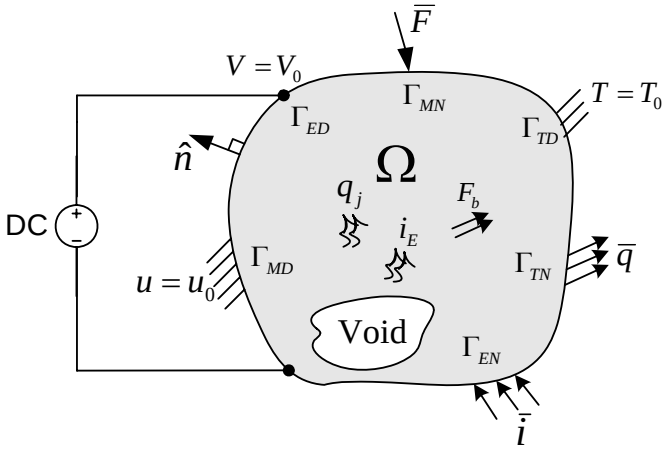

Figure 3-1: Schematic of the general design domain Ω with mixed boundary conditions.

N refer to Dirichlet (natural) and Neumann (essential) type boundary conditions, respectively. In mathematics, a Dirichlet boundary condition imposed on an equation specifies the values a solution is to take on the boundary of the domain and a Neumann boundary condition imposed on an equation specifies the values the derivative of a solution is to take on the boundary of the domain.

The boundary Γ is composed of six regions: $\Gamma_{MD} \cup \Gamma_{MN}$ in mechanical domain, $\Gamma_{TD} \cup \Gamma_{TN}$ in thermal domain and $\Gamma_{ED} \cup \Gamma_{EN}$ in electrical domain. The regions Γ_{MD}, Γ_{TD} and Γ_{ED} can coincide, partly overlap or be fully disjointed; This holds for regions Γ_{MN}, Γ_{TN} and Γ_{EN} as well.

The domain Ω contains a linear electro-thermo-elastic material. Small displacements and constant material properties are assumed. MEMS actuators undergo rather large displacements; however, experimental results at moderate temperatures have shown no sign of plastic deformation [10], which would have been seen as hysteresis or failure in returning the output point to the original position after actuation. Therefore, small strains and linear material behavior in the modelling of the actuators are assumed [10].

The design domain is two dimensional considering the planar nature of MEMS process. The effect of strain gradient and average residual stress in the thin film is neglected and the out of plane deflection in the optimum design is zero.

Let V, T and u be the voltage, temperature and displacement field, respectively, at a point in the domain. These are the independent variables in electrical, thermal and elastic energy domains, respectively. The problem, for a homogenous isotropic material in these three energy domains can therefor be formulated as follows.

The boundary value problem in the *electrical* energy domain is stated as:

$$\begin{aligned} k_e \nabla V + i_E &= 0 \text{ in } \Omega \\ V &= V_0 \text{ on } \Gamma_{ED} \\ \hat{n} k_e \nabla V &= \bar{\imath} \text{ on } \Gamma_{EN} \end{aligned} \tag{3.1}$$

where k_e is the electrical conductivity matrix of the material. Generally, k_e is a function of temperature and the doping level, which are both functions of position. In an electrically isotropic material k_e is not dependent on orientation. A homogenous material has a constant doping level for the entire domain. However, temperature is a function of position; therefore k_e is also an implicit function of position. The internal current source per unit volume is denoted by i_E, which is assumed to be zero for electro-thermo-mechanical domain as there are no internal current sources. This makes Equation (3.1) homogenous. The imposed voltage at the boundary Γ_{ED} is denoted by V_0 and $\bar{\imath}$ is the current flux vector imposed on boundary Γ_{EN}. $\hat{n}$ is a unit vector normal to the surface directed outward from the boundary Γ.

The *thermal boundary* value problem is formulated as:

$$\begin{aligned} k_t \nabla T + q_j &= 0 \text{ in } \Omega \\ q_j &= V k_e \nabla V \text{ in } \Omega \\ T &= T_0 \text{ on } \Gamma_{TD} \\ \hat{n} k_t \nabla T &= \bar{q} \text{ on } \Gamma_{TN} \end{aligned} \tag{3.2}$$

where k_t is the thermal conductivity matrix of the material. k_t is a function of temperature and, to a lesser extent, of the doping level. For a thermally isotropic material, k_t is not dependent on orientation of the material. Also, for a homogenous material, k_t is only an implicit function of position. The heat generation rate per unit volume, q_j, is a function of voltage. The imposed

temperature on Γ_{TD} is denoted by T_0 and $\bar{q}$ is the specified heat flux vector on Γ_{TN}.

The mechanical boundary value problem for linear elastic material is given as:

$$\begin{aligned} \nabla\sigma + F_b &= 0 \text{ in } \Omega \\ \sigma &= C(\varepsilon - \alpha T) \text{ in } \Omega \\ \varepsilon &= \frac{1}{2}(\nabla u + \nabla u^T) \\ u &= u_0 \text{ on } \Gamma_{MD} \\ \sigma\hat{n} &= \bar{F} \text{ on } \Gamma_{MN} \end{aligned} \tag{3.3}$$

where F_b is the body force, σ and ε are the symmetric stress and Green-Lagrange infinitesimal strain tensors, respectively, and C is the elasticity tensor. For homogenous and isotropic elastic material, C is independent of position and orientation. The parameter α is the thermal expansion coefficient vector, which is also a function of temperature and hence of position. u_0 is the imposed displacement on surface Γ_{MD} and $\bar{F}$ is the specified traction force applied to the surface Γ_{MN}. Note that the stress σ is a function of temperature T.

As posed in Equations (3.1), (3.2) and (3.3), the problem has no closed-form analytical solution. Indeed, it is a formidable problem even for iterative numerical solution techniques such as finite element method.

In the following, the equations are simplified for the single field of mechanical domain. A new topology scheme is developed for MEMS mechanical actuators and the results are compared with examples from the available literature. Since the focus of this thesis is on micromechanical applications, the optimization scheme is designed to meet the limitations and concerns of micro-device operations.

3.2 Mechanical Domain

Consider the design domain with boundary conditions shown in Figure 3-2. Assuming that there is no internal body force, $F_b = 0$, the simplified governing equations for this mechanical

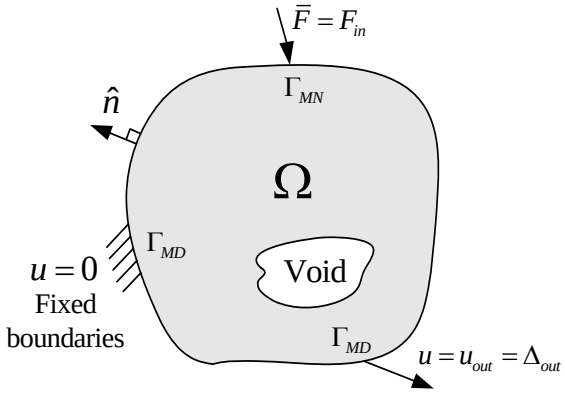

Figure 3-2: Schematic of design domain Ω in single physics of mechanical boundaries.

domain are:

$$\nabla\sigma = 0 \text{ in } \Omega \tag{3.4}$$

$$\sigma = C\varepsilon \text{ in } \Omega$$

$$u = u_0 \text{ on } \Gamma_{MD}$$

$$\sigma\hat{n} = \bar{F} \text{ on } \Gamma_{MN}$$

3.2.1 Constitutive Equations

The governing Equation (3.4) for each element at local coordinate $x - y$ in xy plane is stated as:

$$EA\frac{\partial u}{\partial x} + EI\frac{\partial^2 v}{\partial x^2} = 0 \tag{3.5}$$

where first term refers to axial truss element, second term refers to bending beam element, A is the cross section of the beam element and I is the moment of inertia around the third axis and E is the Young's modulus of elasticity of the material.

The Duhamel-Neuman relation for a elastic body is written as:

$$\sigma_{ijkl} = C_{ijkl}\varepsilon_{kl} \tag{3.6}$$

There exist no more than 21 distinct stiffness coefficients, C_{ijkl}, even for the most general type of anisotropic material. The Duhamel-Neumann equation in explicit matrix form is written as [72]:

$$\begin{Bmatrix} \sigma_{11} \\ \sigma_{22} \\ \sigma_{33} \\ \sigma_{32} \\ \sigma_{31} \\ \sigma_{12} \end{Bmatrix} = \begin{bmatrix} c_{1111} & c_{1122} & c_{1133} & c_{1123} & c_{1113} & c_{1112} \\ - & c_{2222} & c_{2233} & c_{2223} & c_{2213} & c_{2211} \\ - & - & c_{3333} & c_{3323} & c_{3313} & c_{3312} \\ - & - & - & c_{2323} & c_{2313} & c_{2312} \\ - & - & - & - & c_{1313} & c_{1312} \\ - & - & - & - & - & c_{1212} \end{bmatrix} \begin{Bmatrix} \varepsilon_{11} \\ \varepsilon_{22} \\ \varepsilon_{33} \\ 2\varepsilon_{32} \\ 2\varepsilon_{31} \\ 2\varepsilon_{12} \end{Bmatrix} \tag{3.7}$$

where $1, 2$, and 3 correspond to general coordinates in x, y and z direction, respectively. Whenever a material displays some kind of elastic symmetry, the number of distinct coefficients drops. It is often customary to call the direction perpendicular to the planes of elastic symmetry the *principal elastic* directions.

A special case of Equation (3.7) is when the material exhibit no preferred directions with regard to its physical properties. Such materials are called *isotropic.* For isotropic material, the elasticity matrix is [72]:

$$C = \begin{bmatrix} 2\mu+\lambda & \lambda & \lambda & 0 & 0 & 0 \\ \lambda & 2\mu+\lambda & \lambda & 0 & 0 & 0 \\ \lambda & \lambda & 2\mu+\lambda & 0 & 0 & 0 \\ 0 & 0 & 0 & \mu & 0 & 0 \\ 0 & 0 & 0 & 0 & \mu & 0 \\ 0 & 0 & 0 & 0 & 0 & \mu \end{bmatrix} \tag{3.8}$$

where λ and μ are the Lamė elastic constants and, in terms of Young's modulus E and Poison's ratio ν, are represented by:

$$\mu = \frac{E}{2(1+\nu)} \tag{3.9}$$

$$\lambda = \frac{E\nu}{(1+\nu)(1-2\nu)} \tag{3.10}$$

For isotropic materials the Duhamel-Neumann constitutive equations simplify to:

$$\sigma_{ij} = 2\mu\varepsilon_{ij} + \lambda\epsilon_{kk}\delta_{ij} \tag{3.11}$$

where δ_{ij}, known as the Kronecker delta, satisfies the relations:

$$\begin{cases} 0 & \text{if } i \neq j \\ 1 & \text{if } i = j \end{cases} \tag{3.12}$$

Equation (3.7) in 2D plane $x - y$ is simplified to [72]:

$$\begin{Bmatrix} \sigma_{11} \\ \sigma_{22} \\ \sigma_{12} \end{Bmatrix} = \begin{bmatrix} 2\mu + \lambda & \lambda & 0 \\ \lambda & 2\mu + \lambda & 0 \\ 0 & 0 & \mu \end{bmatrix} \begin{Bmatrix} \varepsilon_{11} \\ \varepsilon_{22} \\ 2\varepsilon_{12} \end{Bmatrix} \tag{3.13}$$

For the bars and frames with solid cross sections, it can be assumed that Poisson's ratio is zero, so that [73]:

$$2\mu = E \tag{3.14}$$

$$\lambda = 0 \tag{3.15}$$

which results in reducing Equation (3.13) to:

$$\begin{Bmatrix} \sigma_{11} \\ \sigma_{22} \\ \sigma_{12} \end{Bmatrix} = \begin{bmatrix} E & 0 & 0 \\ 0 & E & 0 \\ 0 & 0 & \frac{E}{2} \end{bmatrix} \begin{Bmatrix} \varepsilon_{11} \\ \varepsilon_{22} \\ 2\varepsilon_{12} \end{Bmatrix} \tag{3.16}$$

and, assuming that shear strain effect is negligible in frame elements, results in:

$$\begin{Bmatrix} \sigma_{11} \\ \sigma_{22} \end{Bmatrix} = \begin{bmatrix} E & 0 \\ 0 & E \end{bmatrix} \begin{Bmatrix} \varepsilon_{11} \\ \varepsilon_{22} \end{Bmatrix} \tag{3.17}$$

Combining Equations (3.5) and (3.17), the finite element equation for a frame element in matrix

form is [73]:

$$\{\sigma\} = [C]\{\varepsilon\} \tag{3.18}$$

A frame structure is composed of beam elements that can transfer both axial forces and bending moments. Because the assumption of linear small deformations is followed here, it is assumed that they are decoupled and can be superpositioned. With this assumption, from Equation (3.5) the elasticity matrix for a frame element is:

$$C = \begin{bmatrix} EA_e & 0 \\ 0 & EI \end{bmatrix} \tag{3.19}$$

where I is the moment of inertia of the cross section around neutral axis, A_e is the cross section of element, which is assumed constant along its length, and C is the elasticity matrix for a frame element.

3.2.2 Finite Element Discretization

The design domain Ω is discretized with plane frame elements with prismatic cross sections. Members in plane frame are designed to resist axial and bending deformations and are connected by stiff joints. The two-node beam element and the axial-truss element are combined together to form an element that can be used to analyze rigid-joint planar frameworks. It is assumed that the axial and bending effects are uncoupled from each other, which is a reasonable assumption within the framework of small deformation theory [74].

As shown in Figure 3-3(a), a local coordinate system is established for each element. Each node has three degrees of freedom, two translations and one rotation. The moment of inertia is assumed constant over each element and concentrated loads are allowed only at the nodes of an element. In the local coordinate system, the element equations are a combination of the truss element and beam element. The displacement vectors are:

$$\{u^n\} = \left\{ \begin{array}{cccccc} d_1 & d_2 & d_3 & d_4 & d_5 & d_6 \end{array} \right\}^T \tag{3.20}$$

$$\{u\} = \left\{ \begin{array}{cccccc} u_1 & v_1 & \theta_{z1} & u_2 & v_2 & \theta_{z2} \end{array} \right\}^T \tag{3.21}$$

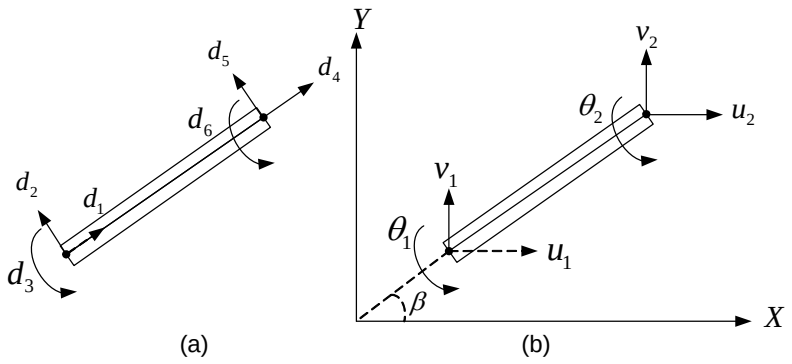

Figure 3-3: Degrees of freedom of a two-node frame element in (a) local coordinate and (b) global coordinate.

where $\{u^n\}$ and $\{u\}$ are the local and global nodal displacements, respectively, u_i represents the axial deformation, and v_i and θ_{zi} represent the bending deformations. The element equations in the finite element method are derived using Rayleigh-Ritz method [74] with Hermitian shape functions for displacement interpolation. Using the Hermitian interpolation shape functions, the matrix of shape functions, N, is:

$$N = \begin{bmatrix} N_1 & 0 & 0 & N_4 & 0 & 0 \\ 0 & N_2 & N_3 & 0 & N_5 & N_6 \end{bmatrix}^T \tag{3.22}$$

where N_i is the Hermitian shape function. The total strain in Equation (3.18) is expressed in terms of nodal displacements as:

$$\{\varepsilon\} = [B]^T \{d\} \tag{3.23}$$

$$B = \begin{bmatrix} N_1' & 0 & 0 & N_4' & 0 & 0 \\ 0 & N_2'' & N_3'' & 0 & N_5'' & N_6'' \end{bmatrix}^T \tag{3.24}$$

where prime denotes the differentiation with respect to x. Substitution in Equation (3.18) gives:

$$\{\sigma\} = [C][B]^T \{u\} \tag{3.25}$$

The element matrices are then assembled through enforcement of compatibility and equilibrium

for nodes and elements and:

$$K = \int_{\Omega} [B]\,[C]\,[B]^T\, d\Omega \tag{3.26}$$

$$\{F\} = [K]\{u\} \tag{3.27}$$

where $[K]$, $\{F\}$and $\{u\}$ are the global stiffness matrix, force vector and nodal displacements, respectively. The boundary conditions are then imposed to solve the finite element equation for displacement field [73].

The design domain is meshed with a finite number of nodes and elements. A full ground structure is a set of elements in a grid of points where each point is connected to every other point. In the literature, a full ground structure is recommended for the topology synthesis using truss, beam or frame elements. A full ground structure is impractical to use as it involves very long and overlapping elements in the continuum. Instead, the ground structure shown in Figure 3-4 is proposed here. The design domain is discretized with frame-like ground structure with two different meshing policies to enable the study of mesh dependency of the solutions.

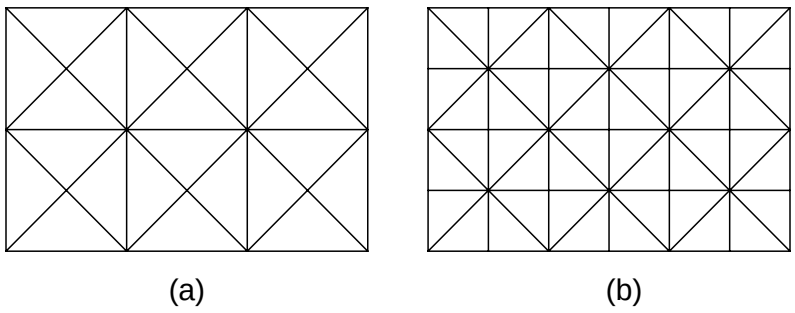

Figure 3-4: Frame ground structure with (a) light mesh (b) dense mesh.

3.2.3 Statement of Problem

Because the compliant system optimization is posed in terms of a set of conflicting design requirements, a type of optimization scheme is required to determine a compromise solution. One way to handle conflicting design objectives is by using the multicriteria optimization. The basis for the multicriteria formulation of an optimal compliant topology problem is the

physical intuition that a compliant mechanism should meet both the flexibility and stiffness requirements.

The multicriteria formulation based on the ratio of objectives, stated in Equation (2.18), is the basis to derive the optimal topology of compliant mechanisms in this chapter. The strain energy, SE from Equation (2.16) is the measure of stiffness and mutual strain energy, MSE from Equation (2.17) is the measure of flexibility. To overcome the problem of one objective dominating the solution in Equation (2.18), a new objective function is proposed here as:

$$Maximize : \frac{(sign(MSE))^{m-1} MSE^m}{SE^n} \tag{3.28}$$

where m and n are user defined power coefficients and $(sign(MSE))^{m-1}$ is a term that keeps the sign of MSE and the direction of output deflection, when $m > 0$ is an even number. Note that SE is always a positive number. Addition of user defined power coefficients m and n provides the option to scale the orders of magnitude of the two objectives to arrive at the desired balance between the two criteria, avoiding one objective dominating the solution. The resulted optimum topology is sensitive to the choice of the power coefficients, similar to Equation (2.17). However, using the ratio type objective function reduces the sensitivity of solution to m and n coefficients.

For a system with mechanical boundary conditions, as shown in Figure 3-2, the optimization problem is stated as:

$$\begin{aligned} Maximize \quad &: \quad \frac{(sign(MSE))^{m-1} MSE^m}{SE^n} \\ Subject\ to \quad &: \quad \text{lower and upper bounds on design variables} \\ &\quad\quad\ \ \text{Mechanical equilibrium equations} \\ &\quad\quad\ \ \text{flexibility constraints} \\ &\quad\quad\ \ \text{stiffness constraints} \end{aligned} \tag{3.29}$$

Including the finite element discretization of design domain into Equation (3.29), and considering A_e, the cross section area of each element as the design variable, the optimization problem

is posed as:

$$
\begin{aligned}
Maximize : (sign(MSE))^{m-1} \frac{(U_d^T K_2 U_1)^m}{(\frac{1}{2} U_3^T K_3 U_3)^n} \qquad (3.30)\\
Subject\ to : A_{lower} \leq A_e \leq A_{upper}\\
K_1 U_1 = F_{in}\\
K_2 U_d = F_d\\
K_3 U_3 = -F_d\\
u = u_0 \text{ on } \Gamma_{MD}
\end{aligned}
$$

where A_e is the cross section area of the eth element and, A_{lower} and A_{upper} are the lower and upper bounds on design variable. In the next section, details of the mathematical solution and implementation for this optimization problem are presented.

3.3 Implementation and Simulation Results

Here, the computational procedure and solution algorithm for the optimization statement of Equation (3.30) is presented. Some examples are studied that illustrate the results of the algorithm and compare these results with truss-element-based designs and continuum method designs in the available literature.

3.3.1 Solution Technique

A genetic algorithm (GA) is adopted to solve the optimization problem stated in Equation (3.30). Solving with GA requires no gradient information and can, in principle, achieve the global optimum in multiple runs. The flow chart of binary-coded GA implemented in Matlab [75] is presented in Figure 3-5. This algorithm finds the maximum of the fitness function. The user may define all or part of an initial population, e.g. $x_i = 0.5(x_{upper} + x_{lower})$, or leave the program to choose an initial population randomly between the lower and upper bounds.

The default algorithm uses a fixed population size and no generational overlap. Three genetic operations: reproduction, crossover, and mutation are performed during procreation. The probability that an individual of the population will reproduce is proportional to its fitness.

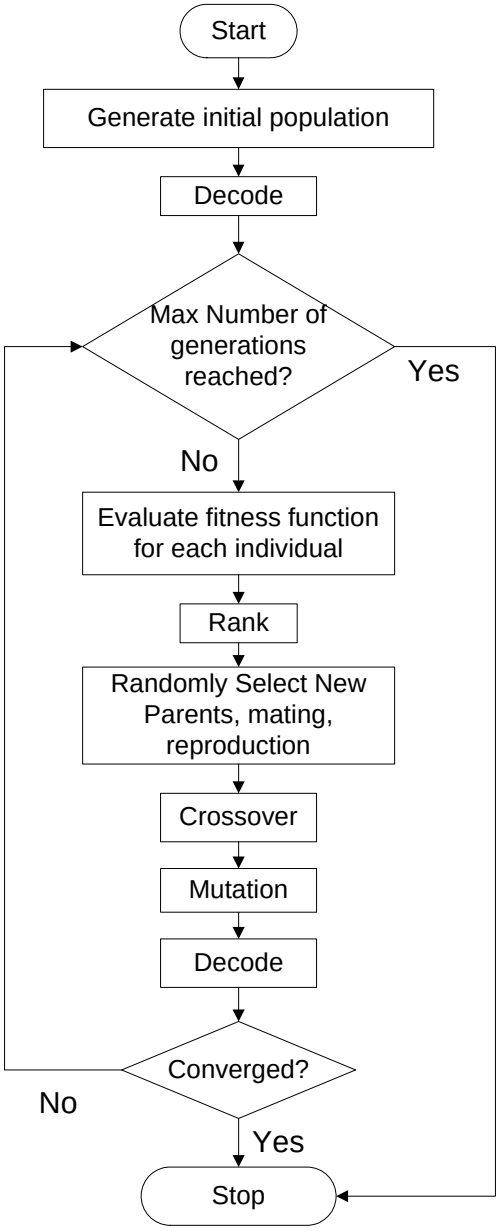

Figure 3-5: Flow chart of implemented binary-coded genetic algorithm.

Individuals chosen for reproduction are mated randomly. Mating produces two offspring (constant population size). Crossover in mating occurs with probability P_c and the crossover index is randomly selected. Each feature of the offspring can mutate independently with probability P_m.

Convergence of the algorithm is based on two criteria. First, the change in the design variable must be sufficiently small. Second, the value of the design objective is compared to the value from the previous iteration. Since this is a maximization problem, the algorithm is considered to have converged when the design objective stops increasing. If one of these criteria is not met, the algorithm returns and repeats the procedure using the updated population as the starting point until the maximum number of generations is reached. If the number of maximum generations is reached and the algorithm has not yet converged, a message will show that: "Maximum number of generations reached without termination criterion met. Either increase maximum generations or ease termination criterion."

Graphical User Interface

The binary-coded GA was implemented in Matlab [75]. A graphical user interface (GUI) is designed to ease the monitoring of the results. Figure 3-6 presents a schematic flow chart of the main optimization program developed in Matlab [75].

Because the focus of this research is on micro-compliant mechanisms, the program is designed to use $\mu m - kg - s$ system of units. In this case, dimensions are in μm, forces are in μN, and pressure is in MPa.

This details of designing a user interface for a topology optimization package are explained in Appendix A. The GUI designed for a single field of a mechanical domain is a simplified version of the GUI presented in Appendix A for the multi-physics optimization package and follows the same procedure.

In the following section, several design examples illustrating the results of the algorithm are presented.

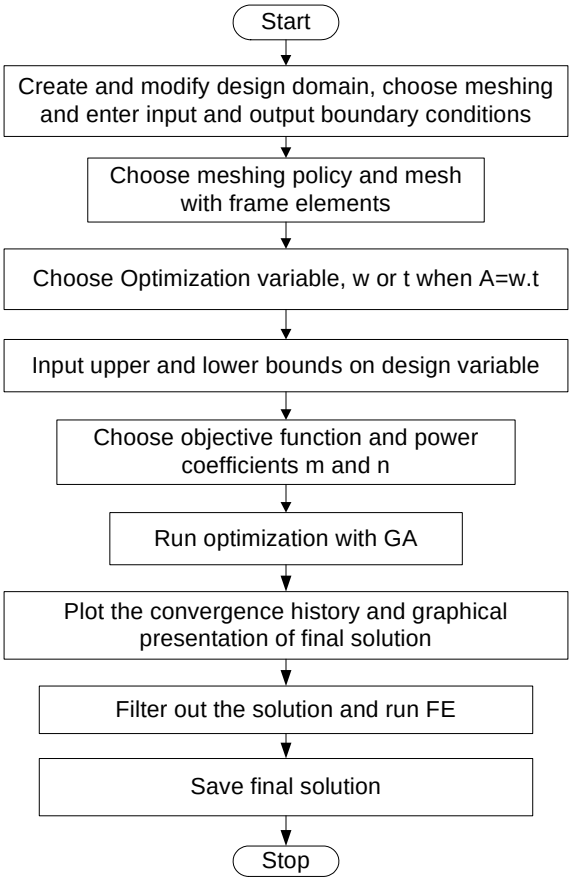

Figure 3-6: Flow chart of Graphical User Interface of program, implemented in Matlab.

3.4 Numerical Examples

In this section, compliant mechanism design examples are presented which illustrate the results of the algorithm and compares them with truss-element-based designs and continuum method designs. In all of the examples, the design problem is illustrated in terms of the design domain, boundary conditions, applied load, and required output deflection. The agreement of the optimal solution with the problem specifications is discussed.

The objective here is to synthesize the topology of a compliant mechanism and satisfy the given input and output specifications and other constraints. The space constraints within which the mechanism should fit are defined as a rectangular design domain. The prescribed design domain is divided into a number of nodes and a network of frame elements connecting these nodes which serves as an initial guess. The optimized compliant mechanism is a network of a subset of frame structure.

3.4.1 Compliant Gripper Mechanism

For the purpose of comparison, solutions to the compliant gripper problem using both discrete optimization with truss elements and using a continuum formulation with the homogenization method are presented [1].

A compliant gripper is a one-piece device that has no kinematic joints and requires no assembly. It can effectively transmit the input force/displacement to the output due to the absence of wear and backlash. Potential application areas include MEMS, nano-scale manipulators, and precision tools.

Figure 3-7(a) shows a concept of an compliant gripper. A symmetric half-view of the design problem is shown in Figure 3-7(b), where the dashed line represents the design domain, and the boundary conditions (nodal constraints) are as indicated. The design specifications are that an applied force, F_{in}, causes the motion, Δ, in the vertical direction. The direction of the desired output displacement is specified in terms of a unit vector. Note that the point of application of the applied force is constrained to move only in the horizontal direction due to the symmetry

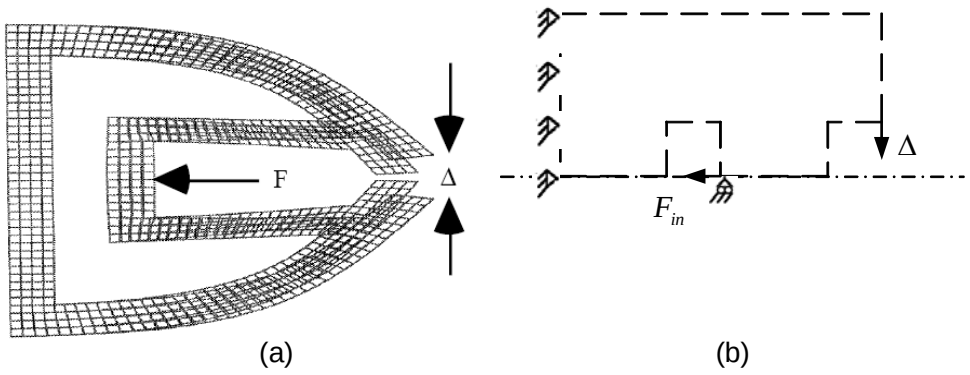

Figure 3-7: (a) Schematic of a compliant gripper mechanism and (b) the symmetric half view of the design domain.

of the problem. The other problem specifications are [1]:

$$F_{in} = [-10, 0] \quad kN \tag{3.31}$$

$$\Delta \text{ in the direction of } [0, -1]$$

$$E = 2.0 \quad GPa$$

$$0.001 < A < 0.5$$

$$A = tw,\ t = 0.5,\ 0.002 < w < 1$$

$$\text{Convergence Criteria} = 1e - 5$$

Figure 3-8(a), shows the initial frame ground structure. Each node has three degrees of freedom (x, y, θ). The objective function is:

$$Maximize : sign(MSE)\frac{MSE^2}{SE} \tag{3.32}$$

where the initial guess is randomly generated between upper and lower bounds. In order to maximize the design objective while satisfying the constraints, the algorithm changes the value of the design variables in each iteration so that the uneconomical members tend toward the lower bound constraints and the economical members tend toward the upper bound constraints. The optimal solution is the most efficient arrangement of beam members in terms of the design

objective and constraints. The optimum gripper mechanism is illustrated in Figure 3-8(b). The remaining members are superimposed on the initial frame structure with thick lines. Figure 3-8(e) shows the full schematic of the optimized solution of the compliant gripper.

The algorithm converged to optimal solution after 44 iterations, as shown in Figure 3-8(c). A finite element analysis of this solution was performed in order to verify the solution behavior. The result is shown in Figure 3-8(d), in which the undeformed shape is denoted by the solid lines and the deformed shape is denoted by the dashed lines. The displacements calculated here are for the optimal design subjected to the applied load F_{in}.

The algorithm generated a solution that efficiently connects the point of application of the load, the point of desired output displacement and the support points. The use of frame elements tends to yield solutions without flexural pivots because the elements bend as a whole. Therefore, qualitatively speaking, the resulting designs tend to have distributed compliance rather than lumped compliance.

Mesh refinement should ideally yield the same topology. To study the mesh dependency of the optimum design, the domain is discretized with a dense meshing scheme, as shown in Figure 3-9(a). The resulted optimum solution from this meshing scheme is shown in Figure 3-9(b). The optimum solution resulting from dense meshing is compared with the mechanism in Figure 3-8(d). These two structures are very similar in principle, which indicates the mesh independency of the optimum solution configuration. Figure 3-10 shows the topology design of the gripper with full truss-ground structure as the initial guess (Figure 3-10(a)). Figures 3-10(b) and (c) show the convergence of the topology to the optimum solution in Figure 3-10(d). Compared with the frame-ground structure in Figure 3-8(d), these designs share some similarities in topology but are different in principle. This resultant topology has overlapping elements which are connected with pin joints.

In terms of manufacturability, the frame element approach provides designs that can be most authentically realized. The optimum solution is Figure 3-10(d) is not feasible to fabricate through MEMS fabrication techniques. The joints connecting the truss elements must be replaced by pseudo hinge-like structures if a jointless compliant mechanism is to be physically realized. The physical characteristics of the optimized design may be lost in making that conversion to flexural hinges. In addition, high stress concentrations in flexural hinges are a

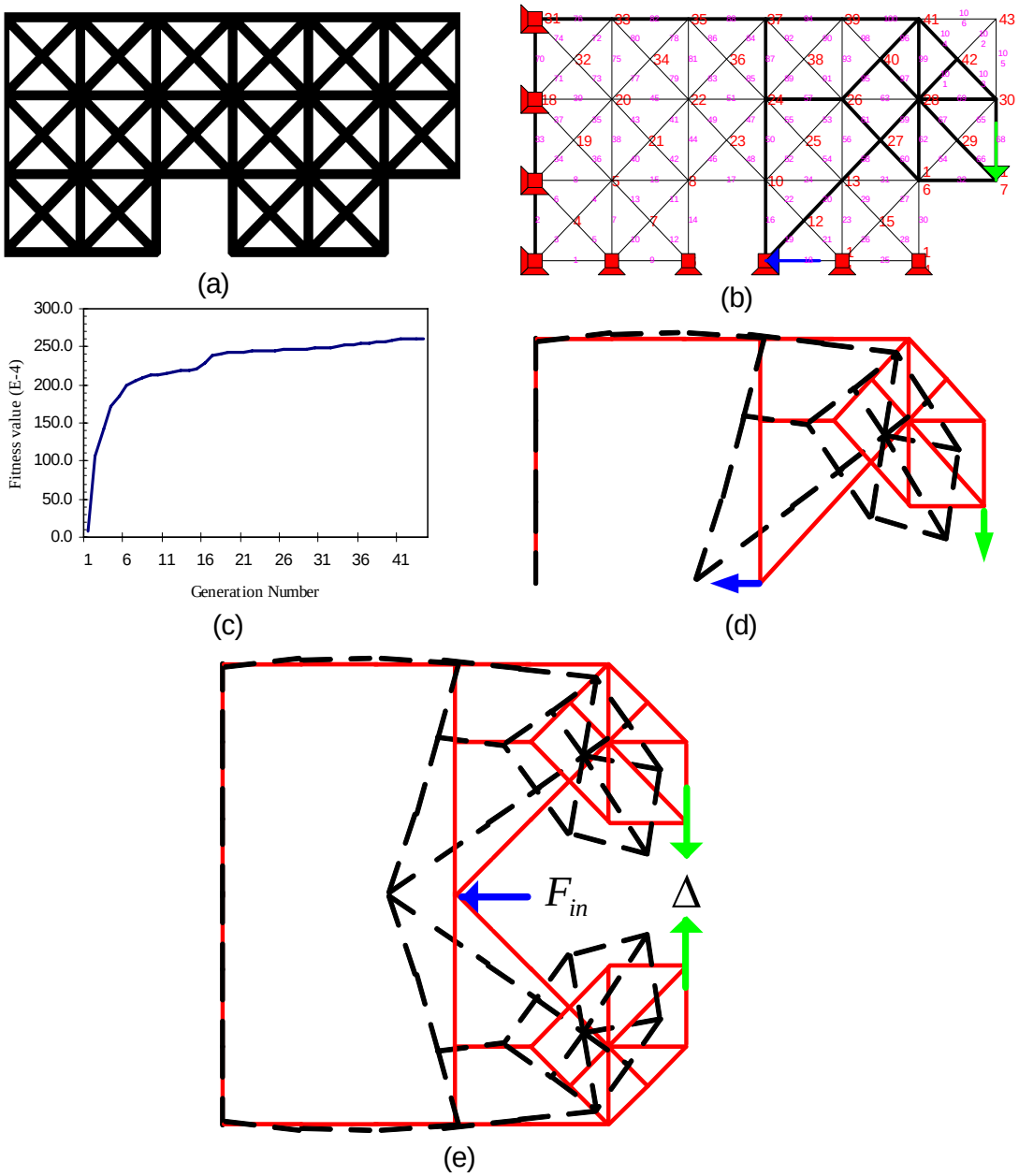

Figure 3-8: Compliant gripper mechanism design (a) Initial guess, (b) optimized solution (c) convergence history, (d) finite element model and (e) full view of optimum gripper mechanism.

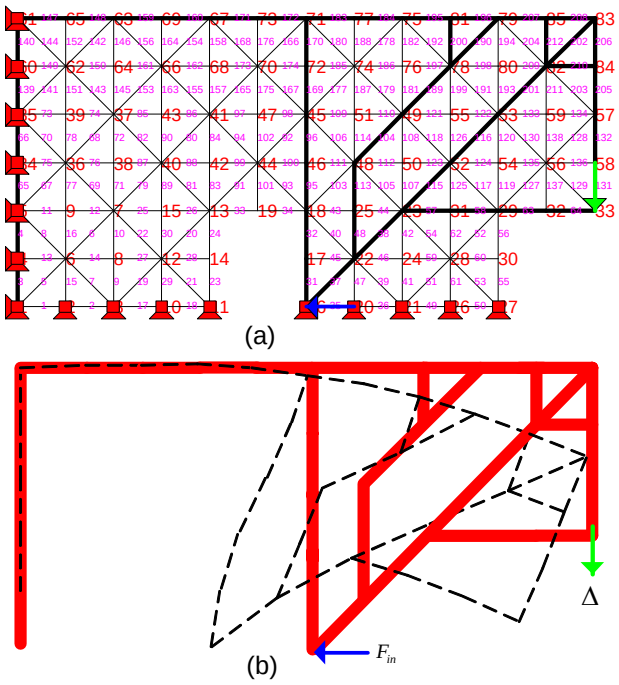

Figure 3-9: (a) Dense meshing scheme for gripper mechanism design and, (b) deformed and undeformed shape of optimal mechanism.

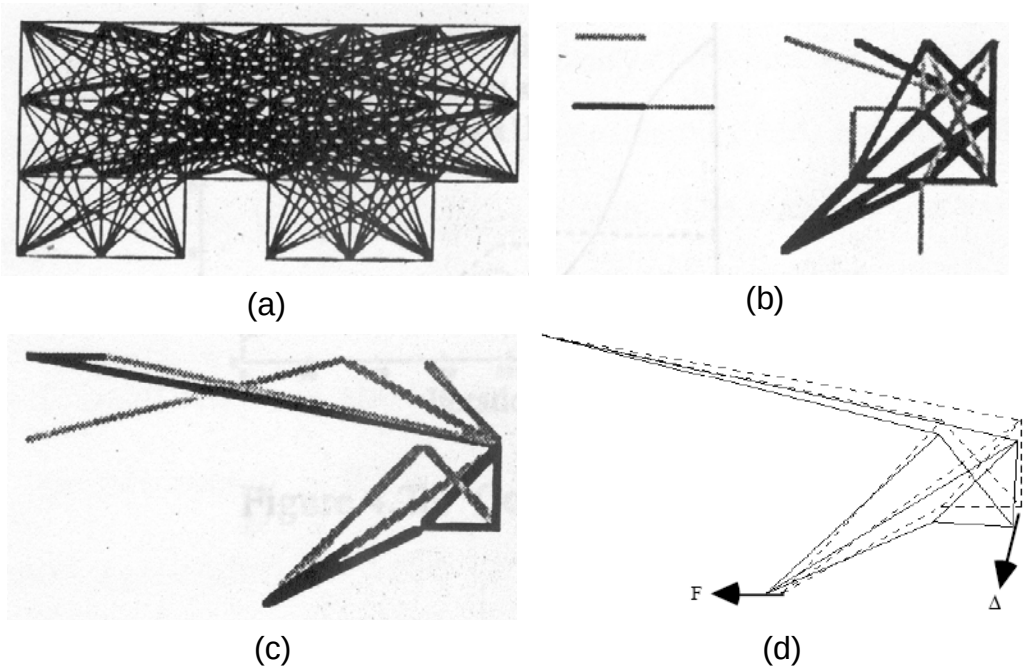

Figure 3-10: Compliant gripper design generated by truss elements [1]. (a) initial guess, (b) 125 iterations (c) 250 iterations and (d) optimal solution after 448 iterations with finite element model.

drawback.

Figure 3-11 shows the optimum solution of a gripper using the continuum homogenization method [2]. The solution shows the checkerboard patterns and narrow flexural hinges in areas. Checkerboard patterns often appear in the optimal configuration when using the continuum method because of numerical instability. A Checkerboard patch is a pattern of alternating solid and void elements in an optimal topology. The appearance of such patterns is common in topology optimization and is attributed to poor numerical modelling and the use of lower order finite elements [76].

From a computational efficiency point of view, the proposed GA is the most efficient, followed by truss ground structure. The continuum method generates more sophisticated structures than the other two and is therefore the most computationally expensive. From the repeatability of the resulted design point of view, the implemented GA shows a better convergence to an unique solution when compared with SLP or SQP, which have been used in the literature

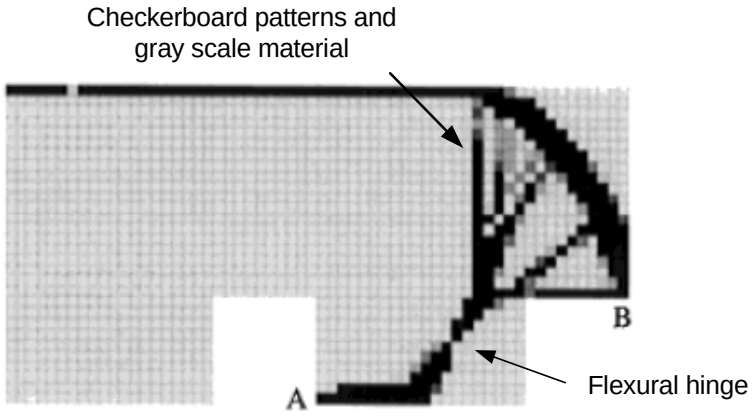

Figure 3-11: Compliant gripper design generated by continuum homogenization method after 350 iterations [2]. This design is not compatible for MEMS fabrication because of checkerboard patterns. It also involves high stress concentration in narrow sections and flexural hinges.

and are highly dependent on the initial guess. The algorithm results show very similar designs in different runs.

Once the mechanism topology is determined, an actual compliant mechanism prototype can be designed. If the performance of the modified solution is satisfactory, the process is continued and a CAD interface file in the IGES format is generated. The IGES format is chosen for its compatibility with many modelling and analysis software packages, e.g. ANSYS [11].

When MEMS compliant structures are the target, this layout can be transferred to the commercial layout editors available to create required masks for fabrications. Manufacturability of the resulted design depends on input parameters, such as the lower limits on design variables. To guarantee the compatibility of the optimum design with available MEMS processes, the design rules and limited features of the PolyMUMPs [77] process have been included in the element removal scheme inside the algorithm. These, of course, can be changed according to any other process limits.

3.4.2 Compliant Crimping Mechanism

An example of a compliant crimping mechanism is shown in Figure 3-12(a). The input force is transferred to the output port and some energy is stored in the form of strain energy in the

flexible members. Note that if the entire device were rigid, it would have no mobility and it would be a structure.

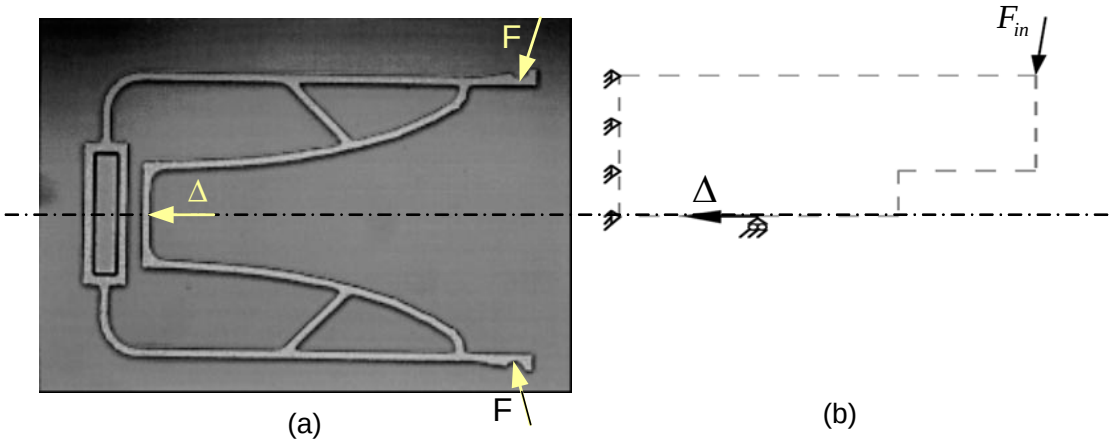

Figure 3-12: (a) Compliant crimping mechanism [3] [4] and, (b) upper half view of compliant crimping mechanism design domain.

The design domain shown in Figure 3-12(b) represents the upper half view of a crimping mechanism, since it is assumed to be a symmetric problem without any loss of generality in the solution procedure. The design specifications are that an applied force, F_{in}, causes the motion, Δ, in the horizontal direction. The direction of the desired output displacement is specified in terms of a unit vector. Notice that the point of application of the applied force is constrained to move only in the horizontal direction due to the symmetry of the problem. The other problem specification are:

$$F_{in} = [-1, -5] \quad kN \tag{3.33}$$

$$\Delta \text{ in the direction of } [-1, 0]$$

$$E = 2.0 \quad GPa$$

$$A = tw, \; t = 0.5, \; 0.002 < w < 0.5$$

$$\text{Convergence Criteria} = 1e - 5$$

The initial guess is a modular frame structure, shown in Figure 3-13(a), with a random

distribution of cross sectional areas. The node and element numbering and the optimized solution is shown in Figure 3-13(b) with thick lines. The GA converged to optimal solution after 25 iterations, as shown in Figure 3-13(c), and generated a solution that efficiently connects the point of application of the load, the point of desired output displacement and the support points. The corresponding finite element model of the optimum solution is shown in Figure 3-13(d), in which the deformed shape is denoted by the dashed lines and the undeformed shape is denoted by the solid lines. Figure 3-13(e) shows the complete crimping mechanism and the finite element model. With inspection, it is evident that the output displacement is in the specified direction. Figure 3-14 shows the initial guess with full truss-ground structure and resulting optimum mechanism [5]. When compared with frame elements, the initial meshing is extensive and the algorithm converges after 386 iterations. In comparison, the GA converged after 23 iterations. As mentioned previously, this optimum solution is not compatible for MEMS fabrication because of element overlapping and pin joints.

3.4.3 Design issues

Having defined the objective function to synthesize a compliant mechanism starting from the desired input/output specifications, the influence of the following design parameters on the behavior of the objective function is discussed here.

One limitation of previous formulations in the literature is that the MSE (see Equations (2.14) and (2.17)) plays a dominant role in controlling the behavior of the entire objective function. Subsequent studies revealed that the MSE tends to approach infinity because of the attempt to maximize MSE with force as input. Therefore, to maximize MSE, or compliance, the design variables, which are cross sectional area, approach lower bounds, leading to impractical results. The first attempt to remedy the situation involves proper scaling of the two terms, MSE and SE. Having user-defined powers m and n in the proposed formula serve this scaling purpose. By employing the proposed formulation in Equation (3.28), MSE and SE can be scaled properly, avoiding domination of the objective function by MSE.

Formulations that maximize flexibility have been shown to be ill-formulated for compliant mechanism optimization [15]. As a solution, in [16] stress constraints were employed to account for failure modes. However, the stress constraint may yield to overly stiff topologies and may

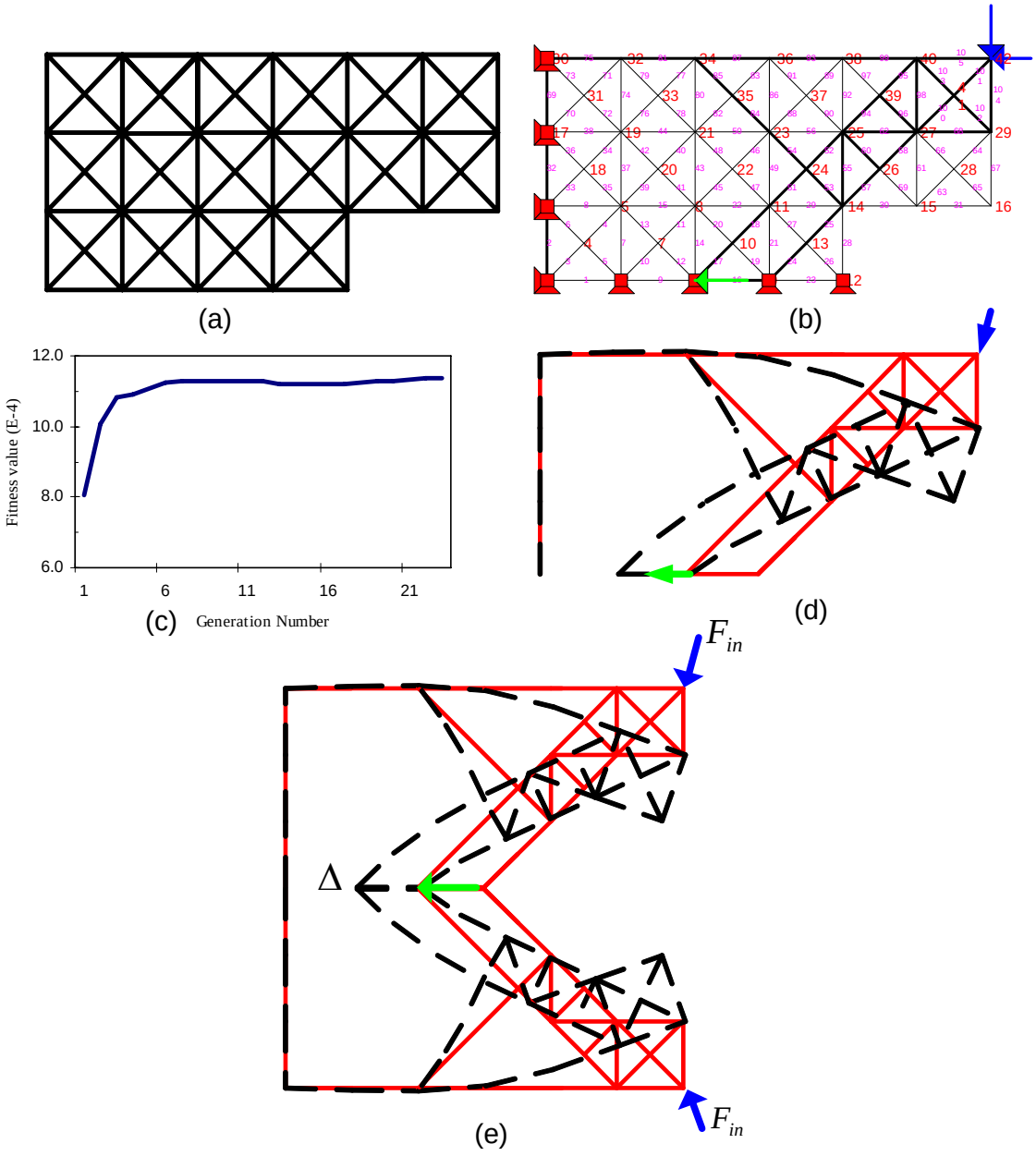

Figure 3-13: Compliant crimping mechanism design (a) Initial guess frame ground structure, (b) optimized solution (c) convergence history of GA (d) finite element model of optimum solution and (e) full view of optimum crimping mechanism.

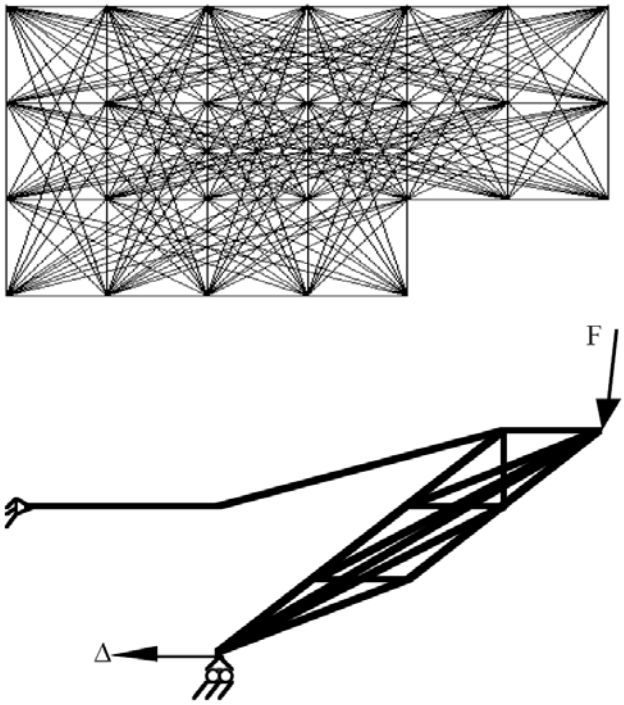

Figure 3-14: Initial guess and resulted compliant crimping mechanism design using truss elements [5].

also be inadequate to model the failure criteria directly. As a solution, a new strength constraint should be employed while maximizing the output displacement .

The optimized solution depends on the lower limits on the design variable and in order to avoid mathematically viable but physically impractical designs, one should avoid using meaningless bounds. Typically, in MEMS applications the design domain is restricted by the packaging constraints, and the bounds on design variables are constrained by the fabrication process limits. For instance, the minimum width of the beam element cannot be less than 2 [μm] using multi-user microfabrication techniques available though MUMPs [77]. The current element removal policy in the literature is to eliminate the beam members whose design variables reached the lower bound constraint, when the algorithm converges. The solution consists of beam members whose [design variable reaches (or is close to) the upper bound. If the lower bound is defined considering MEMS fabrication limits, e.g. 2 [μm], the final design consists of elements on or close to 2 [μm], which still significantly contribute to the stiffness of the structure. If these elements are eliminated, the resulting structure may not perform as desired. This issue should be addressed by a new element removal policy for topology optimization in MEMS.

The designer has to strike a balance between the choice of material and actuator displacement. For a design domain described by bounds on the design variables and materials, the designer may wish to adjust the magnitude of the input load. The structure becomes more flexible as the magnitude of the input force is increased. The choice of material has an effect on the behavior of the objective function, similar to that of the magnitude of the input force. That is, when the material becomes stiffer, when all other parameters are fixed, the individual element of the structure becomes thinner.

These identified design issues will be addressed in Chapter 5.

3.5 Conclusions

In this chapter, an improved multi criteria objective function was proposed. The proposed multi criteria formulation was implemented with genetic algorithm. The potential issues in implementing the algorithm with MEMS fabrication limits were addressed for further extension of this method to multi-disciplinary domains. Topology optimization of a compliant gripper

and a compliant crimping mechanism were compared with those of a truss ground structure and homogenization method from the literature. The comparison verifies that the frame-ground structure is the most suitable for MEMS applications. In addition, the developed GA effectively overcomes the previous convergence difficulties. The proposed objective function implemented with the genetic algorithm shows distinct advantages over other methods, such as:

- The proposed objective function provides control over the importance of flexibility or stiffness with user control power coefficients. Using proper powers, the problem of one objective dominating the solution can be avoided.

- The resulting design is a frame-like structure, which is feasible for MEMS fabrication. There is no joint or element overlapping, as seen in truss element method, or hinges, checkerboards and gray-material regions, as seen in homogenization method. The use of beam elements tends to yield solutions without flexural pivots because the elements bend as a whole. Therefore, qualitatively speaking, the resulting designs tend to have distributed compliance rather than lumped compliance.

- The GA shows a better repeatability. It converges to very similar solutions in different runs, when compared with SLP or SQP, in which the solutions are strongly dependent on an initial guess.

- The continuum method generates more sophisticated structures than the other two and is, therefore, the most computationally expensive. The frame ground structure is the most efficient, followed by the truss-ground structure.

In the next chapter, the analysis is extended to multi-disciplinary micro-domains with coupled boundary conditions. The governing equations for the case of electro-thermo-mechanical domain are derived and solved with a new, fully coupled analysis method. This new coupled field solver enables pre-fabrication study of electro-thermo-mechanical devices and allows designers to modify their designs. It is also developed to serve as the core finite element solver in the topology optimization scheme developed later in this thesis.

Chapter 4

A New Fully-Coupled Analysis Method for Multi-physics Domains

Although there is a wealth of literature in the modelling of thermal and electro-thermal actuators, the literature is limited to particular systems with a limited number of elements. Developing a new, fully-coupled, finite element formulation is necessary to solve a general multi-disciplinary domain with arbitrary arrangement of boundary conditions and large number of nodes and elements. This method of solving is essential in developing topology optimization of MEMS devices in which an automated modelling and solution procedure is required. This chapter presents a new, coupled formulation for automated modelling of multi-disciplinary domains using a coupled resistive circuit method, modified nodal analysis (MNA), and finite element analysis (FEA). An algorithmic approach for sequential analysis of an arbitrary ground structure with multi-disciplinary boundaries is developed and implemented in Matlab [75] with a graphical user interface. The results are then applied to examples from previous work in the literature. This formulation provides a fast and reliable tool to analyze electro-thermo-elastic devices, which allows large flexibility in the selection of mechanical, thermal and electrical boundary conditions. It also enables topology optimization in thermal and electro-thermal actuators. Moreover, it provides a powerful tool for the development, evaluation, and modification of electro-thermal actuators and sensors.

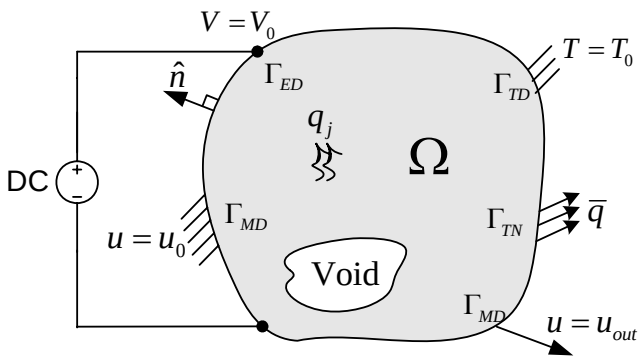

Figure 4-1: Electro-thermo-elastic domain with applied voltage, specified temperature, fixed displacements and specified heat flux at the boundary Γ.

4.1 Coupled Field Modelling

4.1.1 Governing equations

For an electro-thermo-mechanical actuator, the general multi-physics domain presented in Chapter 3, Figure 3-1, is simplified as seen in Figure 4-1. The design domain Ω is defined as the solid design region. The boundary conditions on boundary Γ, as shown in Figure 4-1, are applied voltage, in the electrical boundary condition Γ_{ED}, the internal current source is zero, the thermal boundary conditions are a specified temperature at Γ_{TD} and a specified heat flux at Γ_{TN}, the mechanical boundaries are fixed displacements at Γ_{MD} and there is no external applied force in the form of input in the micro-domain. There are reaction forces at the mechanical boundary, which will be calculated in FE analysis.

A constrained elastic structure deforms upon heating. The geometrical shape of the structure, the manner in which the structure is supported at its boundaries, and the material properties influence the thermally induced deformation. In micromechanical structures, achieving Joule heating is possible through internal heat generation due to current distribution.

For the domain shown in Figure 4-1, the general Equations (3.1), (3.2) and (3.3) are sim-

plified as:

$$\begin{aligned} \nabla^2 V &= 0 \text{ in } \Omega \\ q_j &= J^2 R_e \text{ in } \Omega \\ k_t \nabla T + q_j &= 0 \text{ in } \Omega \\ \nabla \sigma &= 0 \text{ in } \Omega \\ \sigma &= C(\varepsilon - \alpha T) \text{ in } \Omega \end{aligned} \tag{4.1}$$

subject to:

$$\begin{aligned} V &= V_0 \text{ on } \Gamma_{ED} \\ T &= T_0 \text{ on } \Gamma_{TD} \\ \hat{n} k_t \nabla T &= \bar{q} \text{ on } \Gamma_{TN} \\ u &= u_0 \text{ on } \Gamma_{MD} \end{aligned} \tag{4.2}$$

The equations are solved in the listed order. The first step is to solve the continuity equations of the current with a given voltage boundary condition. The current flow in each element causes Joule heating. This internal heat source is the input to the next step, which is the steady-state heat transfer equation. The heat transfer equilibrium is solved to find the temperature distribution in the structure. The thermo-elastic equation is then solved to find thermally induced displacements.

Electro-thermo-mechanical actuators undergo rather large displacements; however, evaluation of each element in the finite element model shows that the strain level is still small and a linear elastic model is sufficient to study the problem.

4.2 Voltage and Current Distribution

The design domain is defined and discretized into a finite number of nodes and frame elements. The continuity equation of current in the electrical field is solved using modified nodal analysis method (MNA) [78] and resistive circuit method [79]. Although the node voltage method and

loop current method are the most widely used, MNA is a powerful technique that results in larger systems of equations than the other methods, but it is easier to implement algorithmically. This offers a substantial advantage for automating the procedure and enables multiple input voltages. The method described here, with some modifications, as explained in the following, is compatible with finite element analysis and produces matrix form equations to solve for both the voltage at each node and the current through each element with the resistive circuit method.

Since the meshing policy for all the domains is unified, the set of equations from MNA should be compatible with finite element discretization. To overcome this problem, after the initial FEA mesh is generated, a search algorithm is developed inside the program to unify the MNA and FEA node and element connectivities in mesh structure. The result of this search algorithm is a resistive circuit that enables coupling of electrical, thermal and mechanical domains properly.

Each element is placed in its expected place to form the MNA main matrices and solve the voltage distribution equation. The general rule in MNA is to number the ground node to 0 and continue numbering the other nodes to avoid singularity in matrix equations. To solve this problem, another search algorithm is developed that searches for specified ground voltage in boundary conditions and eliminates that node from the connectivity matrices of the electrical domain. After the voltage distribution is solved, the search algorithm places the node and corresponding elements back in their corresponding place to form the FEA matrices. This method results in a fully-coupled, resistive circuit and finite element analysis between electrical and thermo-elastic fields.

4.2.1 Equivalent Resistive Circuit

The first step is to generate an equivalent resistive circuit from the initial mesh of the frame ground structure. A beam element has an equivalent electrical resistance, as in [80]:

$$R_e = \rho_0 \frac{L_e}{A_e} \tag{4.3}$$

where R_e is the beam equivalent electrical resistance [Ω], ρ_0 is the electrical resistivity of the material at room temperature [Ω-μm], A_e is the cross section area of the element [μm^2], and L_e is the element length [μm]. Usually, the resistivity ρ is assumed to have a linear dependency

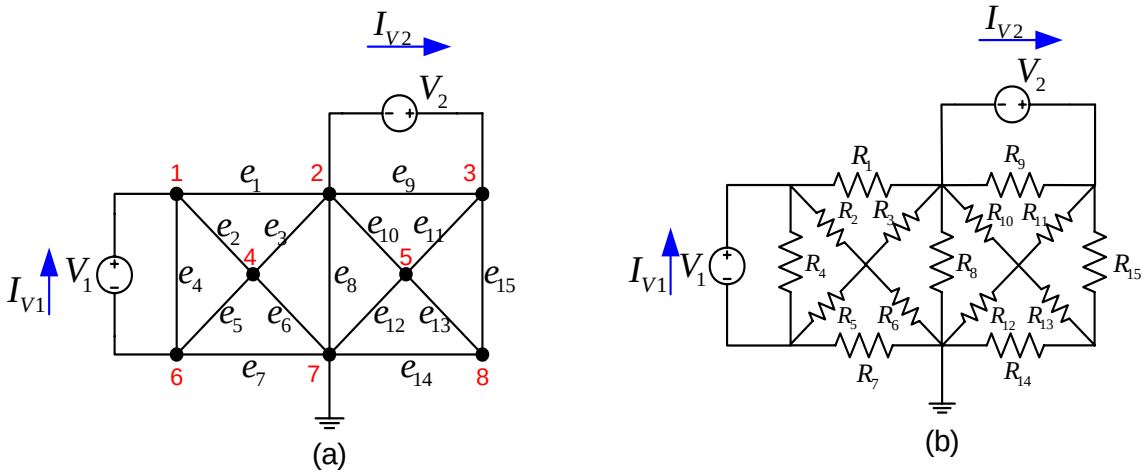

Figure 4-2: (a) Frame structure with voltage at input and (b) its equivalent resistive circuit.

on the temperature of the material, as in [80]:

$$\rho = \rho_0[1 + \xi(T - T_0)] \tag{4.4}$$

where ρ is the material resistivity at temperature T $[^\circ C]$, ξ is the temperature coefficient of electrical resistivity and T_0 is the initial temperature. Using Equation (4.3), ρ_0 is replaced by ρ to incorporate the resistivity dependency to temperature. As an example, Figures 4-2(a) and (b) show an initial frame structure generated with 8 nodes and 15 elements and its equivalent resistive circuit, respectively. Solving a set of equations that represent a circuit of resistive elements is straightforward; however, forming the matrix equations requires more attention to ensure compatibility with the FE mesh. The procedure is described in the following section.

4.2.2 Modified Nodal Analysis Method, MNA

Applying MNA to a circuit of resistors and independent voltage sources, as shown in Figure 4-2, results in a matrix equation of the form:

$$AX = Z \tag{4.5}$$

Voltage across an independent voltage source is specified independently of any other variable in a circuit (e.g. current).

For a circuit with g node and h independent voltage source:

- A is $(g + h)(g + h)$ matrix in size. The $(g \times g)$ part of the matrix holds the known quantities, which are the resistance of elements, and the rest of A matrix contains only 0, 1 and -1.
- X matrix is an $(g + h) \times 1$ vector that holds the unknown quantities, nodal voltages and the current through the independent voltage source. The top g elements are the nodal voltages. The bottom m elements represent the current through the h independent voltage sources.
- Z matrix is an $(g + h) \times 1$ vector that holds only known quantities, which are voltage boundary conditions. The top n elements are zero. The bottom h elements represent the h independent voltage sources in the circuit.

The circuit is then solved by a matrix manipulation:

$$X = A^{-1}Z \tag{4.6}$$

MNA Algorithmic Approach

An algorithmic method for generating MNA equations is described here. There are three matrices that must be generated: the A matrix, the X matrix and the Z matrix, as explained previously. Developing the X and Z matrices is rather straightforward and was explained previously.

The A matrix will be developed as the combination of four smaller matrices, G, B, C, and D in the form:

$$A = \begin{bmatrix} [G] & [B] \\ [B]^T & [C] \end{bmatrix} \tag{4.7}$$

where G matrix is $(g \times g)$ and is determined by the interconnections between the resistive circuit elements, B matrix is $(h \times g)$ and is determined by the connection of the voltage sources and

C matrix is $(h \times h)$ and is zero when independent voltage sources are considered. G matrix is an $(g \times g)$ symmetric matrix formed in two steps:

- each element in the diagonal matrix is equal to the sum of the conductance (one over the resistance) of each element connected to the corresponding node. So, the first diagonal element is the sum of conductances connected to node 1, the second diagonal element is the sum of conductances connected to node 2, and so on.
- the off diagonal elements are the negative conductance of the element connected to the pair of corresponding node. Therefore, a resistor between nodes 1 and 2 goes into the G matrix at location (1,2) and locations (2,1).

Rules for making B matrix:

- B matrix is an $(g \times h)$ matrix with only 0, 1 and -1 elements. Each location in the matrix corresponds to a particular voltage source (first dimension) at a node (second dimension). If the positive terminal of the ith voltage source is connected to node k, then the element (i, k) in the B matrix is a 1. If the negative terminal of the ith voltage source is connected to node k, then element (i, k) in B matrix is a -1. Otherwise, elements of B matrix are zero.

Rules for making the C matrix

- C matrix is an $(h \times h)$ matrix that is composed entirely of zeros.

Following this algorithmic approach, Equation (4.6) is solved for the nodal voltages and current distribution in each element.

Implementing MNA inside the FEA mesh

Here the method of coupling resistive circuit to initial FEA mesh is explained. For the example of Figure 4-2, $g = 9$ and $h = 2$, the voltage source V_1 is connected between two nodes 1 (positive) and 6 (negative), V_2 is connected to node 2 (negative) and 3 (positive) and the

ground is connected to node 7. The MNA equations are formed as:

$$G = \begin{bmatrix} \sum \frac{1}{R_{1,2,4}} & -\frac{1}{R_1} & 0 & -\frac{1}{R_2} & 0 & \dots & \dots & \dots \\ \dots & \sum \frac{1}{R_{1,3,8,9,10}} & -\frac{1}{R_9} & -\frac{1}{R_3} & -\frac{1}{R_{10}} & \dots & \dots & \dots \\ \dots & \dots & \sum \frac{1}{R_{9,11,15}} & 0 & -\frac{1}{R_{11}} & \dots & \dots & \dots \\ \dots & \dots & \dots & \sum \frac{1}{R_{2,3,5,6}} & 0 & \dots & \dots & \dots \\ \dots & \dots & \dots & \dots & \sum \frac{1}{R_{10,11,12,13}} & \dots & \dots & \dots \\ \dots & \dots & \text{Sym} & \dots & \dots & \dots & \dots & \dots \\ \dots & \dots & \dots & \dots & \dots & \dots & \dots & \dots \\ \dots & \dots & \dots & \dots & \dots & \dots & \dots & \dots \end{bmatrix} \tag{4.8}$$

$$B = \begin{bmatrix} 1 & -1 & 1 & 0 & 0 & -1 & 0 & 0 \end{bmatrix}^T$$

$$C = \begin{bmatrix} 0 & 0 \\ 0 & 0 \end{bmatrix}$$

$$X = \begin{bmatrix} V_1 & V_2 & V_3 & V_4 & V_5 & V_6 & V_7 & V_8 & I_{V_1} & I_{V_2} \end{bmatrix}^T$$

$$Z = \begin{bmatrix} 0 & 0 & 0 & 0 & 0 & 0 & 0 & 0 & V_1 & V_2 \end{bmatrix}^T$$

where R_i are equivalent resistivity for ith element, V_i are the nodal voltages and I_{V_1} and I_{V_2} are the current through voltage sources 1 and 2, respectively. The rest of the elements of matrix G in Equation (4.8) are derived following the guidelines outlined above.

To apply MNA to the initial FEA meshing, the ground node is eliminated from the set of the equations and, after solving for the nodal voltages, it is placed back into voltage vector at its corresponding node number. It is obvious that for a ground node the voltage is zero. For the example shown here, corresponding rows and columns to node 7 are eliminated from all the matrices. After solving for nodal voltages, $V_7 = 0$ is placed back in the voltage vector at row 7. The first 8 numbers in voltage vector are the nodal voltages and the last two numbers are currents through voltage sources. Then the current through each element is calculated as

$$I_e = \frac{V_{e2} - V_{e1}}{R_e} \tag{4.9}$$

where I_e is the current through element e, V_{e1} and V_{e2} are the nodal voltages at the nodes of element and R_e is the equivalent resistant of element e. The current distribution in each element is calculated from MNA analysis. The internal Joule heating for each element becomes:

$$Q_e = I_e^2 R_e \quad [W] \tag{4.10}$$

where Q_e is the internal heat generation in element e. The internal heat generation in Equation (4.10) is used in next step for thermo-elastic finite element analysis and is the key quantity that couples the electrical and thermo-elastic field.

4.3 Temperature Field

In this section, the derivation of the finite element equations and matrices for steady state heat transfer in a generated mesh of frame elements is explained. Since a beam element is long and slender, a one-dimensional analysis of the heat flow longitudinally along the beam length is performed.

For a body with internal heat generation, as shown in Figure 4-3, the governing differential equation in expressed as strong form of 1-D Poisson's equation, which is as follows for heat transfer at steady-state [81]:

$$\frac{\partial}{\partial x}(k\frac{\partial T}{\partial x}) + q_j = 0 \tag{4.11}$$

where k is the thermal conductivity of the material, q_j is the internal heat generation per unit volume and T is the temperature of interest within the domain.

The boundary of the domain is divided into two types of boundary conditions: 1) essential boundaries, which represent the fixed temperatures and 2) natural boundaries, which represent heat flux. Figure 4-3 shows thermal boundary conditions on the surface of a domain with internal heat generation. The heat loss is considered positive direction of flux. The natural boundary conditions can be expressed in terms of a statement of equilibrium between internal and external heat flux at any point on the boundary as:

$$q_x \hat{n}_x = q_s + q_h + q_T \qquad \text{on } S_1,\ S_2 \text{ and } S_3 \tag{4.12}$$

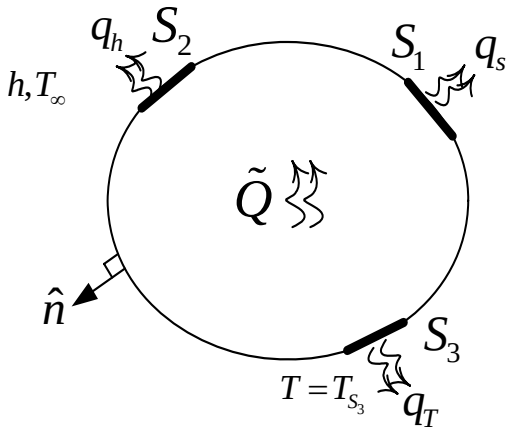

Figure 4-3: Thermal boundary conditions on the surface of a domain with internal heat generation. The heat loss is considered positive direction of flux.

where q_x is the internal heat flux in x direction and $q_x \hat{n}_x$ represents the proportion of q_x normal to the boundary, q_s is conductive heat loss flux on surface S_1, q_h is the convective heat flux on surface S_2, q_T is the reaction heat flux due to specified temperatures on surface S_3. In general, one never knows the actual distribution of q_n, only the reaction forces it causes on the boundary. The remaining component of q_x will run parallel to the body and, therefor, will stay inside the boundary. Knowing that $q_x = -k\frac{\partial T}{\partial x}$, Equation (4.12) is rewritten as [82]:

$$-k\frac{\partial T}{\partial x}\hat{n}_x = q_s + h(T - T_\infty) + q_T \qquad \text{Natural boundary on } \Gamma_{TN} \tag{4.13}$$

where h is the convection heat transfer coefficient, and T_∞ is the ambient temperature. This is valid for any point on the boundary Γ.

The essential boundary conditions are the fixed temperatures on the surface S_3 represented as:

$$T = T_{S_3} \qquad \text{Essential boundary on surface } S_3 \ (\Gamma_{TD}) \tag{4.14}$$

and T_{S_3} is the specified temperature on surface S_3. Galerkin's method is employed to solve Equation (4.11). To apply the Galerkin method, the equation is multiplied by a weight function

and integrated over the domain Ω of the element as [83]:

$$\int_{\Omega} N_i \left(\frac{\partial}{\partial x}(k\frac{\partial T}{\partial x}) + \tilde{Q} \right) d\Omega = 0 \qquad\qquad i = 1, 2, ..., m \tag{4.15}$$

where N_i is the weight function which is the element temperature interpolation shape function and m is the number of nodes.

Applying the Green-Gauss theorem to the first term and knowing that $div(-q) = \frac{\partial(-q_x)}{\partial x}$, Equation (4.15) results in:

$$\oint_{\Gamma} N_i(k\frac{\partial T}{\partial x}\hat{n}_x)d\Gamma - \int_{\Omega}(k\frac{\partial N_i}{\partial x}\frac{\partial T}{\partial x})d\Omega + \int_{\Omega} N_i\tilde{Q}d\Omega = 0 \qquad\qquad i = 1, 2, ..., m \tag{4.16}$$

Substituting natural boundary conditions from Equation (4.13) into Equation (4.16):

$$\int_{\Omega}(k\frac{\partial N_i}{\partial x}\frac{\partial T}{\partial x})d\Omega = \oint_{\Gamma} N_i(-q_s - h(T - T_{\infty}) - q_T)d\Gamma + \int_{\Omega} N_i\tilde{Q}d\Omega \qquad\qquad i = 1, 2, ..., m \tag{4.17}$$

To form the finite element matrix equations, temperature T should be expressed in terms of the shape function as $T = [N]^T\{T\}$, where T is the temperature of interest within the body, $[N]$ is the matrix of shape functions, $[N] = [\ N_1 \quad ... \quad N_m\ ]^T$and $\{T\}$ is the vector of nodal temperatures, $\{T\} = \{\ T_1 \quad ... \quad T_m\ \}^T$. Also temperature gradients are expressed as [84]:

$$\left\{\frac{\partial T}{\partial x}\right\} = [\ \tfrac{\partial N_1}{\partial x} \quad ... \quad \tfrac{\partial N_m}{\partial x}\ ]^T\{T\} = [B]^T\{T\} \tag{4.18}$$

Also from Fourier law:

$$q_x = -k\frac{\partial T}{\partial x} = -[k]\{\frac{\partial T}{\partial x}\} = -[D][B]^T\{T\} \tag{4.19}$$

Substituting Equations (4.18) and (4.19) in Equation (4.17) results in general matrix form of finite element equation for one-dimensional steady-state heat transfer as:

$$\begin{aligned}\int_{\Omega}[B][D][B]^T\{T\}d\Omega = \\ - \oint_{S_1} q_s[N]d\Gamma - \oint_{S_2} h[N][N]^T\{T\}d\Gamma + \oint_{S_2} hT_{\infty}[N]d\Gamma - \oint_{S_3} q_T[N]d\Gamma + \int_{\Omega}\tilde{Q}[N]d\Omega\end{aligned} \tag{4.20}$$

4.3.1 Heat transfer in micro domain

In the following section, the effects of micro-dimensions on general heat transfer in Equation (4.20) are discussed.

There are three possible modes of heat transfer: convection, conduction and radiation.

Natural Convection

The dimensionless number that describes buoyancy driven flow from a hot surface and indicates the importance of natural convection is Raleigh number, R_a [82]:

$$R_a = \frac{g\alpha_{air}}{\upsilon\beta}(T - T_\infty)D^3 \tag{4.21}$$

where g is the acceleration due to gravity, α_{air} is the coefficient of thermal expansion of air, υ is the kinematic viscosity of air, β is the thermal diffusivity of air, T is the heating element temperature, T_∞ is the ambient temperature, and D is the characteristic dimension, which is width or thickness for a beam, depending on the convecting surface. In the macro-world, R_a is typically large, i.e. in the order of 10^5 to 10^9, and convection is therefore important. For a beam of 2 $[\mu m]$ in width and thickness at a temperature of 650 $[^\circ C]$, $R_a = 2.7 \times 10^{-8}$. Therefore, the micro-scale heat transfer takes place by conduction, as opposed to convection.

Conduction

The heat is transferred to substrate by conduction between the microstructure and the substrate through air. As shown in Figure 4-4, if the vertical spacing between the beam and the substrate, δ, is 2 $[\mu m]$, the conduction heat transfer coefficient h_s can be approximated by [6]:

$$h_s = \frac{k_{air}}{\delta} \tag{4.22}$$

where k_{air} is the air thermal conductivity $[W/m^\circ C]$. Using a k_{air} of approximately 0.03 $[W/m^\circ C]$ for air, h_s is calculated to be 15,000 $[W/m^2\ ^\circ C]$. Note that this value of h_s is much larger than typical macro-scale values. The thermal conductivity of material reduces as temperature increases but its effect is negligible for air [85]. In [86] a shape factor is proposed to account for

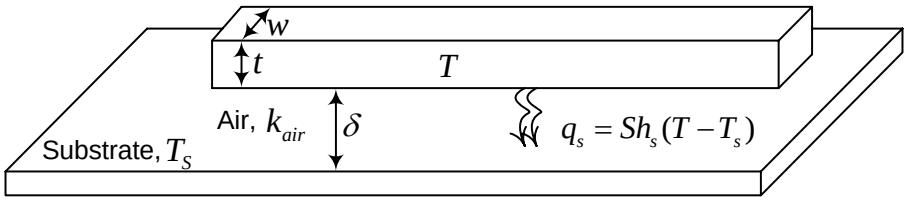

Figure 4-4: Convective heat loss to substrate in micro-dimensions.

the impact of the shape of the element on heat conduction to the substrate. For a beam with a rectangular cross section and dimensions as shown in Figure 4-4, shape factor S is defined as:

$$S = \frac{t}{w}(2\frac{\delta}{t} + 1) + 1 \tag{4.23}$$

where S is the non-dimensional shape factor and:

$$q_s = Sh_s(T - T_s) \tag{4.24}$$

where $h_s = k_{air}/\delta$ is the equivalent conduction coefficient and T_s is the substrate temperature. One may notice that h_s has the same units as the convection coefficient $[W/m^2\ ^\circ C]$.

Radiation

A micro-beam may reach a very high temperature due to current through element and material high resistivity. In this case, radiation effects may become important. The radiation heat transfer coefficient is given by [81]

$$K_r = \epsilon\sigma_s(T + T_\infty)(T^2 + T_\infty^2) \tag{4.25}$$

where ϵ is the emissivity of material, which is 0.7[7] for polysilicon, and σ_s is the Stefan-Boltzman constant. The heat transfer coefficient for radiation was found to be roughly 5-20 $[W/m^2\ ^\circ C]$, compared to 15000 $[W/m^2\ ^\circ C]$ for conduction. Even at very high temperatures, i.e. 1000 $[^\circ C]$, less than 1% of the heat is lost to the surrounding by radiation [87]. It can be concluded that, in micro-scale, the heat lost to surrounding by conduction and convection and radiation effect

is negligible [85].

4.3.2 Finite element formulation for heat transfer in micro-domain

Substituting q_s from Equation (4.24) into Equation (4.20) and collecting the temperature terms in left hand side, the general finite element equation for micro-domain is written as:

$$\int_{\Omega}[B][D][B]^T\{T\}d\Omega + \oint_{S_1} Sh_s[N][N]^T\{T\}d\Gamma + \oint_{S_2} h[N][N]^T\{T\}d\Gamma = \\ + \oint_{S_1} Sh_sT_s[N]d\Gamma + \oint_{S_2} hT_{\infty}[N]d\Gamma - \oint_{S_3} q_T[N]d\Gamma + \int_{\Omega}\tilde{Q}[N]d\Omega \tag{4.26}$$

where the right hand side contains the thermal stiffness matrix terms and the left hand side terms are the thermal forces. As mentioned before, in the micro-domain conduction through air is similar to natural convection and h and h_s have the same units of dimensions. Therefore, q_h and q_s both contribute to the thermal stiffness matrix in the right hand side.

Taking into account the micro-domain effects on the heat transfer phenomenon, the effect of the natural convection can be neglected and Equation (4.26) is rewritten as:

$$\left[\int_{\Omega}[B][D][B]^T d\Omega + \oint_{S_1} Sh_s[N][N]^T d\Gamma\right]\{T\} = \\ \oint_{S_1} Sh_sT_s[N]d\Gamma - \oint_{S_3} q_T[N]d\Gamma + \int_{\Omega}\tilde{Q}[N]d\Omega \tag{4.27}$$

and in finite element form:

$$[K_c + K_s]\{T\} = \{f_s\} + \{f_T\} + \{f_Q\} \tag{4.28}$$

where K_c is the conductive thermal stiffness matrix, K_s is the stiffness matrix, a component of conduction through air gap. K_s is one of the two components of the heat conduction to substrate through air gap. The other component is f_s, the heat flux vector due to conduction through air. f_Q is the heat flux vector due to internal heat generation and f_T is the reaction heat flux vector resulting from specified temperatures. The reaction heat flux due to specified

temperatures, f_T, are always left as nodal values.

$$K_c = \int_\Omega [B][D][B]^T d\Omega \tag{4.29a}$$

$$K_s = \oint_{S_1} Sh_s[N][N]^T d\Gamma \tag{4.29b}$$

$$f_s = \oint_{S_1} Sh_s T_s[N] d\Gamma \tag{4.29c}$$

$$f_T = -\oint_{S_3} q_T[N] d\Gamma \tag{4.29d}$$

$$f_Q = \int_\Omega \tilde{Q}[N] d\Omega \tag{4.29e}$$

Note that in driving finite element equations, heat flux out of the surface, i.e. heat loss, was defined positive. Now the temperature interpolation functions (shape functions) must be defined, in order to continue with development of finite element formulation. Two sets of shape functions are considered here: linear and quadratic.

4.3.3 Linear temperature interpolation

Considering linear shape function for temperature distribution in a two node beam element, $T(x) = \alpha_0 + \alpha_1 x$ and interpolation matrices for element are:

$$[T] = \begin{bmatrix} T_1 & T_2 \end{bmatrix}^T \tag{4.30a}$$

$$[N] = \begin{bmatrix} 1 - \frac{x}{L} & \frac{x}{L} \end{bmatrix}^T \tag{4.30b}$$

$$[B] = \begin{bmatrix} -\frac{1}{L} & \frac{1}{L} \end{bmatrix}^T \tag{4.30c}$$

and the finite element matrices for element stiffness and forces are:

$$K_c = k \int_0^L \int_0^A [B][B]^T dA dx = k \frac{A}{L} \begin{bmatrix} 1 & -1 \\ -1 & 1 \end{bmatrix} \tag{4.31}$$

$$K_s = Sh_s \int_0^L \int_0^w [N][N]^T dw dx = Sh_s wL \begin{bmatrix} 1/3 & 1/6 \\ 1/6 & 1/3 \end{bmatrix} \tag{4.32}$$

$$f_s = Sh_sT_s \int_0^L \int_0^w [N]dwdx = Sh_sT_swL \begin{bmatrix} 1/2 \\ 1/2 \end{bmatrix} \tag{4.33}$$

$$f_Q = \tilde{Q} \int_0^L \int_0^A [N]dAdx = \tilde{Q}AL \begin{bmatrix} 1/2 \\ 1/2 \end{bmatrix} = Q \begin{bmatrix} 1/2 \\ 1/2 \end{bmatrix} \tag{4.34}$$

4.3.4 Quadratic temperature interpolation

Considering Quadratic shape function for temperature distribution in a two node beam element, $T(x) = \alpha_0 + \alpha_1 x + \alpha_2 x^2$ and interpolation matrices are:

$$[T] = \begin{bmatrix} T_1 & T_2 & T_3 \end{bmatrix}^T \tag{4.35}$$

$$[N] = \begin{bmatrix} 1 - 3\frac{x}{L} + 2(\frac{x}{L})^2 & 4\frac{x}{L} - 4(\frac{x}{L})^2 & 2(\frac{x}{L})^2 - \frac{x}{L} \end{bmatrix}^T \tag{4.36}$$

$$[B] = \begin{bmatrix} -\frac{3}{L} + 4\frac{x}{L^2} & \frac{4}{L} - 8\frac{x}{L^2} & 4\frac{x}{L^2} - \frac{1}{L} \end{bmatrix}^T \tag{4.37}$$

and finite element equations of the element are:

$$K_c = k \int_0^L \int_0^A [B][B]^T dAdx = k\frac{A}{L} \begin{bmatrix} \frac{7}{3} & -\frac{8}{3} & \frac{1}{3} \\ -\frac{8}{3} & \frac{16}{3} & -\frac{8}{3} \\ \frac{1}{3} & -\frac{8}{3} & \frac{7}{3} \end{bmatrix} \tag{4.38}$$

$$K_s = Sh_s \int_0^L \int_0^w [N][N]^T dwdx = Sh_swL \begin{bmatrix} \frac{2}{15} & \frac{1}{15} & -\frac{1}{30} \\ \frac{1}{15} & \frac{8}{15} & \frac{1}{15} \\ -\frac{1}{30} & \frac{1}{15} & \frac{2}{15} \end{bmatrix} \tag{4.39}$$

$$f_s = Sh_sT_s \int_0^L \int_0^w [N]dwdx = Sh_sT_swL \begin{bmatrix} \frac{1}{6} \\ \frac{2}{3} \\ \frac{1}{6} \end{bmatrix} \tag{4.40}$$

$$f_Q = \tilde{Q} \int_0^L \int_0^A [N]dAdx = \tilde{Q}AL \begin{bmatrix} \frac{1}{6} \\ \frac{2}{3} \\ \frac{1}{6} \end{bmatrix} = Q \begin{bmatrix} \frac{1}{6} \\ \frac{2}{3} \\ \frac{1}{6} \end{bmatrix} \tag{4.41}$$

After assembly of the matrices based on nodal connectivities and applying the fixed temperature boundary conditions, the nodal temperature distribution is calculated by solving Equation (4.28) for T:

$$T = [K_c + K_s]^{-1}(f_s + f_Q + f_T) \tag{4.42}$$

These nodal temperature values are input to thermo-elasticity formulation to calculate thermally induced stresses and strains in the mesh of frame element.

The coupled field analysis package developed in this chapter is capable of implementing both linear and quadratic temperature interpolation.

4.4 Thermo-elastic field

This section will deal with the finite element formulation of thermo-elastic stress and strain analysis for the generated mesh of frame elements. Thermal effects will be included in the formulation in the form of dilatational strains. The theoretical formulation presented in this section is intended for two-dimensional planar frames. The finite element formulation is based on the linear elastic small deformations. The temperature distribution is assumed to be uniform over the section of the structural member.

The following assumptions are made for the thermo-elastic formulation:

- A transverse plane is assumed to remain plane and normal to the beam axis throughout deformation, i.e. the Bernolli-Euler hypothesis.
- The cross-sectional area of the member is assumed undistorted due to elevated temperatures.
- The frame element is assumed doubly symmetric in its cross section so that the shear center and the centroid coincide.
- The strain is small but rotation is allowed.

4.4.1 Thermal strain and stress

Temperature change in a structure causes thermal strain. When the thermal strain is constrained, thermal stress occurs in the structure. The total strain is the sum of mechanical and

thermal strains:

$$\{\varepsilon\} = \{\varepsilon_m\} + \{\varepsilon_{th}\} \tag{4.43}$$

where superscripts m and th denotes mechanical and thermal strains, respectively. The mechanical strain is caused by an applied mechanical load.

The thermo-elastic Duhmel-Neumann relation for a general thermo-elastic body is [72]:

$$\sigma_{ijkl} = C_{ijkl}\varepsilon_{kl} + \beta_{ij}\Delta T \tag{4.44}$$

where ΔT is the temperature change in body and β_{ij} is the thermal moduli.

From Equation (3.7), the Duhamel-Neumann equation for a general thermo-elastic body in explicit matrix form is written as [72]:

$$\begin{Bmatrix} \sigma_{11} \\ \sigma_{22} \\ \sigma_{33} \\ \sigma_{32} \\ \sigma_{31} \\ \sigma_{12} \end{Bmatrix} = \begin{bmatrix} c_{1111} & c_{1122} & c_{1133} & c_{1123} & c_{1113} & c_{1112} \\ - & c_{2222} & c_{2233} & c_{2223} & c_{2213} & c_{2211} \\ - & - & c_{3333} & c_{3323} & c_{3313} & c_{3312} \\ - & - & - & c_{2323} & c_{2313} & c_{2312} \\ - & - & - & - & c_{1313} & c_{1312} \\ - & - & - & - & - & c_{1212} \end{bmatrix} \begin{Bmatrix} \varepsilon_{11} \\ \varepsilon_{22} \\ \varepsilon_{33} \\ 2\varepsilon_{32} \\ 2\varepsilon_{31} \\ 2\varepsilon_{12} \end{Bmatrix} + \Delta T \begin{Bmatrix} \beta_{11} \\ \beta_{22} \\ \beta_{33} \\ \beta_{32} \\ \beta_{31} \\ \beta_{12} \end{Bmatrix} \tag{4.45}$$

For an isotropic material, the Duamel-Neuman constitutive equations are simplified to [88]:

$$\sigma_{ij} = 2\mu\varepsilon_{ij} + \lambda\epsilon_{kk}\delta_{ij} + \beta\Delta T\delta_{ij} \tag{4.46}$$

where λ and μ are the Lame elastic constants from Equations (3.9) and (3.10) and δ_{ij} is the Kronecker delta from Equation (3.12) and:

$$\beta = -\frac{E\alpha}{1-2\nu} \tag{4.47}$$

Equation (4.46) states that, for an isotropic material, temperature change results in a body expansion or shrinkage but no distortion. In other words, temperature change affects the normal strains but not shear strains.

Equation (4.46) in 2D plane $x-y$ is simplified to [72]:

$$\begin{Bmatrix} \sigma_{11} \\ \sigma_{22} \\ \sigma_{12} \end{Bmatrix} = \begin{bmatrix} 2\mu+\lambda & \lambda & 0 \\ \lambda & 2\mu+\lambda & 0 \\ 0 & 0 & \mu \end{bmatrix} \begin{Bmatrix} \varepsilon_{11} \\ \varepsilon_{22} \\ 2\varepsilon_{12} \end{Bmatrix} + \Delta T \begin{bmatrix} \beta & 0 & 0 \\ 0 & \beta & 0 \\ 0 & 0 & \beta \end{bmatrix} \begin{Bmatrix} 1 \\ 1 \\ 0 \end{Bmatrix} \tag{4.48}$$

For the frames with solid cross sections, it can be assumed that Poisson's ratio is zero, so that:

$$2\mu = E \tag{4.49}$$

$$\lambda = 0 \tag{4.50}$$

$$\beta = -E\alpha \tag{4.51}$$

and Equation (4.48) for frame elements is rewritten as [88]:

$$\begin{Bmatrix} \sigma_x \\ \sigma_y \end{Bmatrix} = \begin{bmatrix} E & 0 \\ 0 & E \end{bmatrix} \begin{Bmatrix} \varepsilon_x \\ \varepsilon_y \end{Bmatrix} + \begin{bmatrix} -E\alpha & 0 \\ 0 & -E\alpha \end{bmatrix} \Delta T \begin{Bmatrix} 1 \\ 1 \end{Bmatrix} \tag{4.52}$$

where α is the coefficient of thermal expansion of the material, ε_x and ε_y are the total strains in x and y direction, respectively, ΔT is the element temperature change, A is the cross section of the beam element and I is the moment of inertia around the third axis. As the temperature increases, the coefficient of thermal expansion of material increases, although for polysilicon in air these variations are neglected. The mechanical strain is related to stress through the constitutive equation. Equation (4.52) yields the constitutive equation for a frame structure:

$$\{\sigma\} = [C]\left(\{\varepsilon\} - \{\varepsilon_{th}\}\right) \tag{4.53}$$

where ε_{th} is thermal strain and is denoted by:

$$\begin{Bmatrix} \varepsilon_{th_x} \\ \varepsilon_{th_y} \end{Bmatrix} = \alpha \begin{Bmatrix} \Delta T \\ \Delta T \end{Bmatrix} \tag{4.54}$$

4.4.2 Finite element formulation for thermo-elastic frames

In a linear analysis using the finite element formulation, it is customary to use a simplified form of Green's strain tensor to express the strain-displacement relation as [88]:

$$\frac{\partial u}{\partial x} + \frac{\partial^2 v}{\partial x^2} = 0 \tag{4.55}$$

where u and v are the displacements in x and y direction, respectively. On the right hand side, the first term is a pure axial deformation and the second term is pure bending. Because the assumption of linear small deformations is followed here, it is assumed that they are decoupled and can be superpositioned and the elasticity matrix is as Equation (3.19).

Displacement interpolation functions

The nodal displacement functions of the element at elevated temperatures are assumed to be the same as those at room temperature. Using the Hermitian interpolation shape functions, the total strain in Equation (4.53) is expressed in terms of nodal displacements as:

$$\{\varepsilon\} = [B]^T \{u\} \tag{4.56a}$$

$$B = \begin{bmatrix} N_1' & 0 & 0 & N_4' & 0 & 0 \\ 0 & N_2'' & N_3'' & 0 & N_5'' & N_6'' \end{bmatrix}^T \tag{4.56b}$$

Substitution in Equation (4.53) gives:

$$\{\sigma\} = [C][B]^T \{u\} - [C] \{\varepsilon_{th}\} \tag{4.57}$$

The total potential energy denoted by Π consists of two parts, internal energy U and external energy W_m, which is equal to work done by external loads, that is:

$$\Pi = U - W_m \tag{4.58}$$

The internal energy is the strain energy caused by deformation of the frame and can be written as:

$$U = \frac{1}{2}\int_{\Omega} \{\varepsilon\}^T \{\sigma\}\, d\Omega = \frac{1}{2}\int_{\Omega} \{\varepsilon\}^T \left([C]\left(\{\varepsilon\} - \{\varepsilon_{th}\}\right)\right) d\Omega \tag{4.59}$$

substituting total strain with Equation (4.56a) gives:

$$\begin{aligned} U &= \frac{1}{2}\int_{\Omega} \{u\}^T [B] \left([C][B]^T \{u\} - [C]\{\varepsilon_{th}\}\right) d\Omega = \\ &\quad \frac{1}{2}\{u\}^T \int_{\Omega} [B][C][B]^T \{u\} - [B][C]\{\varepsilon_{th}\}\, d\Omega \end{aligned} \tag{4.60}$$

On the other hand, the work done by external load F_m can be written as:

$$W_m = \frac{1}{2}\{u\}^T \{F_m\} \tag{4.61}$$

Substitute U and W_m in the potential energy:

$$\Pi = \frac{1}{2}\{u\}^T \int_{\Omega} [B][C][B]^T \{u\} - [B][C]\{\varepsilon_{th}\}\, d\Omega - \frac{1}{2}\{u\}^T \{F_m\} \tag{4.62}$$

In order to find the equilibrium solution, the principal of minimum total potential energy is applied. Solving for the stationary value in Equation (4.62), results in [84]:

$$\sum \frac{\partial \Pi}{\partial \{u\}} = \int_{\Omega} [B][C][B]^T \{u\}\, d\Omega - \int_{\Omega} [B][C]\{\varepsilon_{th}\}\, d\Omega - \{F_m\} = 0 \tag{4.63a}$$

$$\int_{\Omega} [B][C][B]^T \{u\}\, d\Omega = \int_{\Omega} [B][C]\{\varepsilon_{th}\}\, d\Omega + \{F_m\} \tag{4.63b}$$

$$[K_m]\{u\} = \{F_T\} + \{F_m\} \tag{4.63c}$$

where F_m is the external applied force vector and K_m and F_T are the mechanical stiffness matrix and thermal force vector, respectively, defined as:

$$K_m = \int_{\Omega} [B][C][B]^T\, d\Omega \tag{4.64a}$$

$$F_T = \int_{\Omega} [B][C]\{\varepsilon_{th}\}\, d\Omega \tag{4.64b}$$

.Substituting Equation (4.52) into (4.64b), the thermal force vector for a beam element with Hermitian shape functions is:

$$F_T = \alpha \int_\Omega [B]\,[C]\left\{\Delta\bar{T}\right\} d\Omega = \left\{ -EA\alpha\Delta\bar{T} \quad 0 \quad -EI\alpha\Delta\bar{T} \quad EA\alpha\Delta\bar{T} \quad 0 \quad EI\alpha\Delta\bar{T} \right\}^T \tag{4.65}$$

where $\Delta\bar{T}$ is the average temperature change in the element, defined as:

$$\Delta\bar{T} = \frac{1}{L}\int_0^L T(x)dx = \frac{T_1 + T_2}{2} \tag{4.66}$$

where T_1 and T_2 are the nodal temperatures. Equation (4.65) verifies that the temperature field has no effect on the stiffness matrix and contributes to loads applied to the body.

By this formulation, solving the thermo-elastic displacement filed is summarized as:

- forming the element local stiffness and force matrices and transferring them to global coordinate using transformation matrix.
- assembling the element matrices based on node and element connectivity.
- applying the mechanical boundary conditions and solving Equation (4.28) for nodal displacements and reaction forces.

4.5 Implementation of Coupled Field Solver

The proposed finite element formulation coupled with MNA is implemented in Matlab [75]. A GUI is designed to ease the user interface and monitoring the results. Because the focus of this research is on micro-compliant mechanisms, the program is designed to use $\mu m - kg - s$ system of units. In this case, dimensions are in $[\mu m]$, forces are in $[\mu N]$, and pressure is in $[MPa]$.

The program starts with opening two main menus for the graphical representation of the design and user command, respectively, as shown in Figure 4-5. The domain is generated and meshed and material properties, displacement, voltage and temperature boundary conditions are entered in the form of nodal values. The cross section area of each element is specified.

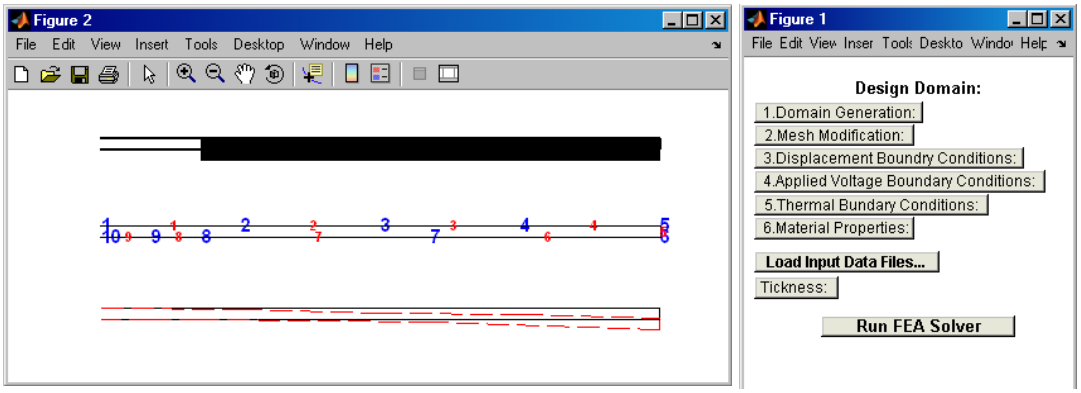

Figure 4-5: FEA solver user interface and main menus.

The data are loaded into the main program and the graphical representation window. Now the user can run the FEA solver. The finite element result is plotted as the deformed shape of the structure and nodal displacements and temperature distributions are plotted. The program saves the solution in data files for future reference. This implementation is part of the GUI designed for the optimization package and is explained in details in Appendix A.

4.5.1 Temperature Dependency of Material Properties

In the above development, the change in material properties due to temperature change is assumed negligible; however, in real applications, electro-thermal actuators endure high temperature changes over their range of operation. For this reason, the material property dependency on temperature is implemented inside the FEA to enable accurate modelling of the actuator behavior. Thermal behavior of material is added as an option inside the FEA solver and can be enabled by user. Since the focus of the analysis is on electro-thermo-mechanical domain, electrical resistivity, thermal conductivity and Young's modulus are identified as the key properties. The temperature dependency of these three material properties is implemented in FEA.

Thermal coefficient of electrical resistivity

In general, electrical resistivity of metals increases with increasing temperature, whereas in semiconductors electrical resistivity decreases with increasing temperature. Equation (4.4)

shows the linear temperature dependency of electrical resistivity. If the value of the temperature coefficient of electrical resistivity, ξ is provided at input, the electrical resistivity of each element is updated according to average temperature change in that element and Equation (4.4).

Thermal coefficient of thermal conductivity

The thermal conductivity of most of the materials reduces as temperature increases but its effect is usually negligible in air. Nevertheless, its dependency to temperature is captured through Thermal Coefficient TCk_t :

$$k_T = k_0(1 + TCk_t\Delta T) \tag{4.67}$$

where k_T and k_0 are thermal conductivity at temperature T and reference temperature, respectively, and $\Delta T = \Delta\bar{T} - T_0$.

Thermal coefficient of Young's modulus of elasticity

As temperature changes, Young's modulus of elasticity of material changes. This behavior is explained through thermal coefficient of Young's modulus denoted as TCE and::

$$E_T = E_0(1 + TCE.\Delta T) \tag{4.68}$$

where E_T and E_0 are Young's modulus at temperature T and reference temperature, respectively, and $\Delta T = \Delta\bar{T} - T_0$.

This equation is implemented inside the FEA code and, if the value of TCE is provided at input, the Young's modulus of each element is updated according to average temperature change in that element and Equation (4.68).

4.6 Verification

The above automated algorithm to solve electro-thermo-mechanical domain is implemented in Matlab [75] and here its results are verified in comparison with analytical and experimental data of some of the actuators in the literature.

One of the most popular actuators in the MEMS community is the pseudo-biomorph that relies on differential expansion of a cold and hot arm to cause it to bend in plane (parallel to the substrate). These thermal actuators, are called electro-thermal compliant actuators (ETC). Another popular actuator is the chevron actuator, in which an array of buckle beams are packed close together and link two common anchored arms with a movable third arm.

In the following section, the results of FEA with experimental results of samples of both these type of actuators from the literature are compared.

4.6.1 Example 1: Electrothermal compliant actuator (ETC)

The ETC actuator consists of two asymmetric parallel arms connected at one end forming an electrical loop. One arm is long and thin and the other arm consists of a wide section and a shorter thin flexure section, as shown in Figure 4-6(a). When a current passes through the loop, the thin arm will heat more than the wide arm and will tend to rotate the actuator. A disadvantage of this type of actuator is that it moves in an arc where most desired movements are linear.

The size of the cross section of the actuator is much smaller than the actuator length. Therefore, the electrothermal analysis of the hot arm actuator is generally simplified as a one-dimensional problem [86]. The thermal actuator domain in Figure 4-6(a) is discretized into finite number of nodes and elements, as shown in Figure 4-6(b). Figure 4-6(c) shows the deformed shape of the actuator for the input voltage of 5 [V]. The boundary conditions for this actuator are:

$$\begin{aligned} V &= V_{dc} && \text{at anchors} \\ V &= 0 && \text{at ground} \\ T &= T_s && \text{at anchors} \\ u &= v = \theta_z = 0 && \text{at anchors} \end{aligned} \tag{4.69}$$

The device is anchored to the substrate at two places, called the device anchor, which provide mechanical support as well as electrical and thermal connections to the substrate. The thermal model imposes an ambient temperature thermal boundary condition at the device anchors. This

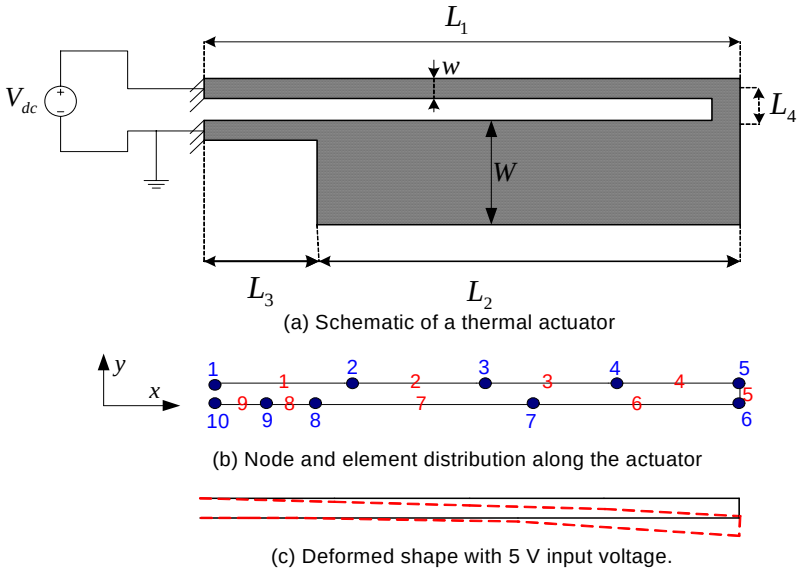

Figure 4-6: (a) Schematic of the thermal actuator ETC, (b) distribution of nodes and elements along the actuator length for finite element analysis, and (c) deformed actuator with 5 [V] at input.

choice of thermal boundary condition, referred to as the essential or Dirichlet thermal boundary condition, is justified when the substrate is thermally grounded by contact with a large thermal mass at the ambient temperature. However, for devices that do not have access to ideal heat sinking, for example due to device packaging, this model is inappropriate.

Material and geometrical properties for a sample actuator fabricate with MUMPs [77] are listed in Table 4.1. For these dimensions and properties, the experimental measurements of vertical deflection versus voltage and the predicted results from closed form equations are shown in Figure 4-7 [6]. The finite element prediction for deflection versus voltage for the same actuator is superimposed in Figure 4-7. The actuator was modelled with 203 nodes and 202 elements. Comparison between these two values shows the accuracy of finite element in analysis of thermal actuators. As mentioned previously, heat dissipation through radiation and free convection are neglected in comparison with the conductive heat loss through air to substrate. From Table 4.1, the conduction coefficient between the actuator and the substrate is:

$$h_s = \frac{k_{air}}{\delta} = \frac{0.03 \times 10^6}{2} = 0.015 \times 10^6 \quad [pW/\mu m^2\,^\circ C] \tag{4.70}$$

Table 4.1: Material and geometrical properties for the thermal actuator.

Material Properties		
Property	Value	Unit
Young's modulus E of polysilicon	160×10^3	MPa
Thermal expansion coefficient α of polysilicon	3×10^{-6}	C^{-1}
Thermal conductivity of polysilicon k	50×10^6	$pW\mu m^{-1}C^{-1}$
Thermal conductivity of air k_{air}	0.03×10^6	$pW\mu m^{-1}C^{-1}$
Resistivity of polysilicon	22	$\Omega - \mu m$
Geometrical Data [6]		
L_1, L_2, L_3, L_4	$200, 164, 36, 4$	μm
w, t, W	$2, 2, 15$	μm
V_{dc}	5	V
air gap to substrate δ	2	μm
T_s, T_∞	25	$^\circ C$

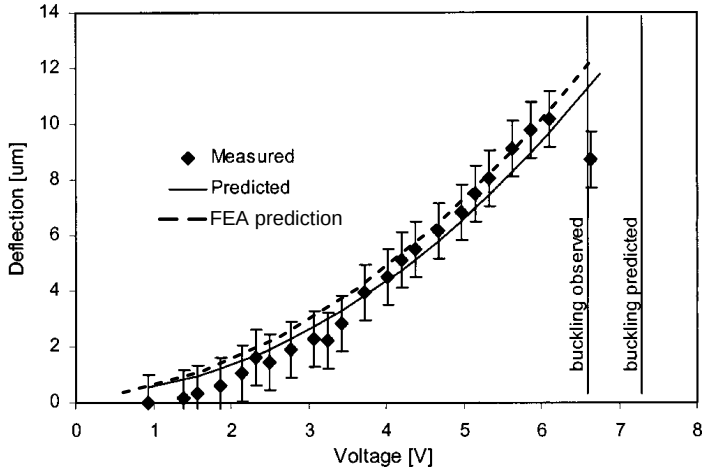

Figure 4-7: Plot of simplified analytical and measured deflection as a function of voltage reported in [6] and tip deflection versus voltage from the FEA code.

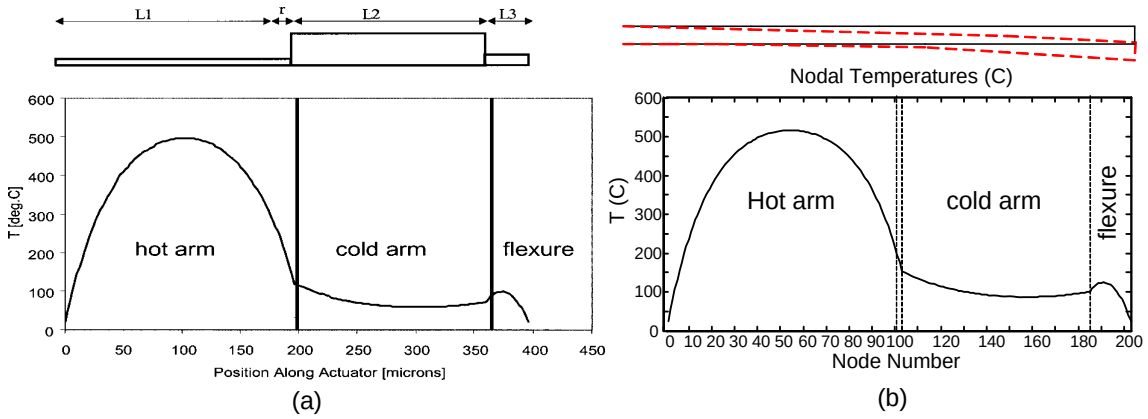

Figure 4-8: Temperature distribution (a) simplified analytical solution [6] (b) finite element solution with 203 nodes and 202 elements along the actuator length.

where comparing with air convection coefficient, $h = 25\ [pW/\mu m^2\ ^\circ C]$, confirms the importance of conduction.

Figure 4-8(a) shows the simplified analytical solution for the temperature distribution along the actuator at input voltage of 5 [V] [6]. In the figure, the maximum temperature is shown in the middle of the arm. The hot arm can reach temperatures as high as 500 $[^\circ C]$. Since the hot arm and flexure arm are both connected to the anchor, the temperature at those points is equal to the substrate temperature, $T_s = 25\ [^\circ C]$. At the joint point between the hot arm and the cold arm, the temperature changes abruptly, because the cold arm acts as a heat sink. To evaluate the finite element model, nodal temperature values are plotted, as shown in Figure 4-8(b). As seen in the figure, finite element can predict the temperature distribution as accurately as the closed form solution plotted in Figure 4-8(a). Comparison among the data reported in [6], illustrated here, and the data from finite element analysis shows a good agreement.

Mesh dependency of finite element solution

To study the mesh dependency of the FEA solution, Figure 4-9(a) shows the convergence of the maximum temperature and tip deflection by increasing the number of nodes per actuator length. As seen in Figure 4-9(a), the values merge to analytical solution at 18 nodes and increasing the number of nodes does not have a significant effect on the results for node numbers larger

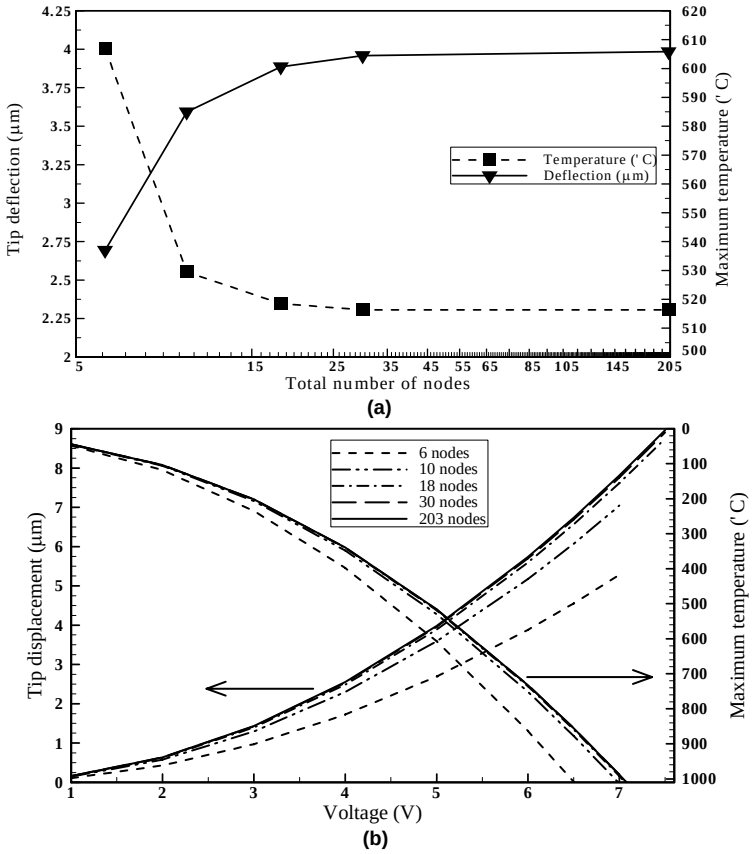

Figure 4-9: (a) Tip deflection and maximum temperature converge to exact solution with 30 nodes and 29 elements (b) convergence of deflection and maximum temperature versus voltage.

than 18. Comparing the values for 30 and 203 nodes in Figure 4-9(a) for both temperature and displacements verifies this concept. Figure 4-9(b) shows how the displacement and maximum temperature versus voltage curves converge to the analytical solution by increasing the number of nodes. Again as seen in this figure, the solutions for 18 nodes and higher overlap. In addition, Figure 4-9(b) clearly shows that the maximum temperature increases with the input voltage. In general, for polysilicon, the maximum temperature should be kept below 1000 [$^{\circ}C$] to avoid thermal failure and self annealing. For this actuator, finite element predicts the thermal failure at $V = 7$ [V], as seen in Figure 4-7.

To further investigate the convergence dependency of solution, Figure 4-10 shows the temperature profile along the actuator length with respect to increasing the number of nodes. As

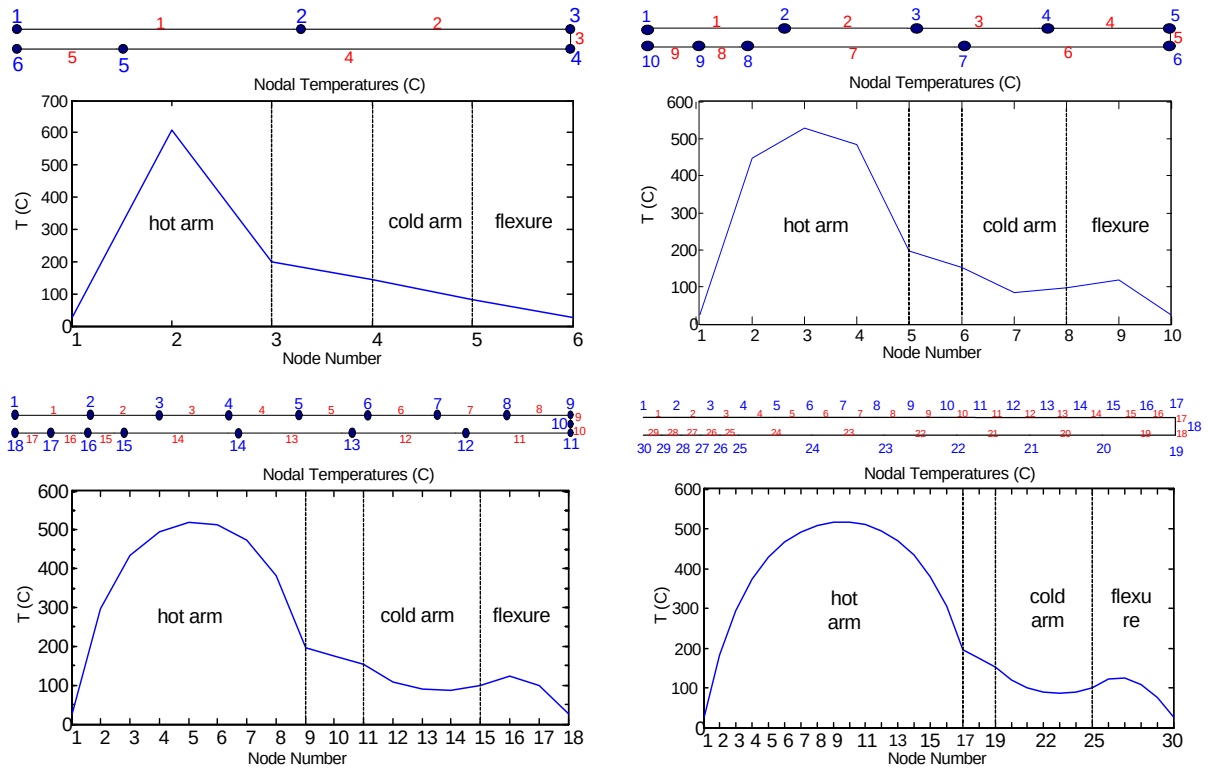

Figure 4-10: Comparison of temperature distribution for input voltage 5 [V] with 5, 10, 18 and 30 nodes per length of the actuator. It is shown that with 30 nodes, FEA converges to analytical solution in Figure 4-8(a).

seen, by increasing the number of nodes, the solution converges to the analytical solution in Figure 4-8(a) at the node numbers are increased.

Effect of element length on FEA results:

The ETC domain is discretized with frame elements. Frame elements, like Euler beam elements, are assumed to be long enough to neglect the effect of shear stresses. The question that might arise is whether analysis will fail if one discretizes the domain with short length elements.

To investigate the effect of element length on the FEA solution, the domain is discretized with 2 [μm] length elements. The cross section of the hot arm is also 2×2 [μm^2] so the elements are cubes along the hot arm and flexure. This results in 203 nodes and 202 elements along the actuator length. Figures 4-8(b) and 4-9 show the temperature profile, maximum temperature

and tip deflection for this set up. As see in the figures, the FEA analysis converges to the exact solution.

The explanation is that in an electro-thermo-mechanical domain, the shear stresses in the whole domain are very small. Since the dominant forces are axial, expansion, and bending, neglecting the shear effect will not disturb the solution even in small length elements. This analysis shows that frame elements are proper for analysis of this type of domains in general.

4.6.2 Example 2: Chevron actuator (TIM)

Figure 4-11 shows a schematic of a chevron actuator, also known as in plane thermal actuator (TIM), where an array of buckle beams are packed close together and link two common anchored arms with a movable third arm. The actuator array consists of only one thermal expansion beam per actuator. The results of a chevron actuator fabricated with MUMPs [77] process as presented in [7], are described herein. Figure 4-11(b) shows a single arm actuator. As a voltage is applied between the mechanical anchors, ohmic heating of the two half-beams causes them to expand and ultimately buckle. The beam is designed with a prebend angle α_b so buckling will have an affinity to move in plane. Here again, the buckle beam temperature should be kept below 1000 $[^{\circ}C]$ to prevent self annealing, which can cause irreversible damage.

Arrays of buckle beam devices can be easily designed by arranging them in a pattern resembling a chevron, as shown in Figure 4-11(a). A center beam is added to stiffen the midpoint and allow mechanical coupling of the individual beams. There is no theoretical limit to the number of beams that can be added, as long as the device and conductors can handle the current and heat, the beams can lose heat rapidly and there is no cross coupling of heat from one beam to another [7].

The actuator array tested in [7] consists of 218 $[\mu m]$ half beams and a 2 $[\mu m]$ by 2 $[\mu m]$ cross sectional area. It is reported that when the pre-bend angel is close to zero, most actuators attempt to buckle out of plane. The full array response can be predicted as the displacements are the same and the forces from each arm add linearly.

The pre-bend angle is usually very small, on the order of a fraction of a degree. The measured deflection is dependent on actuation voltage, beam length and pre-bend angle and not on actuator thickness or number of actuator pairs. Figure 4-13(a) is a graph of measured

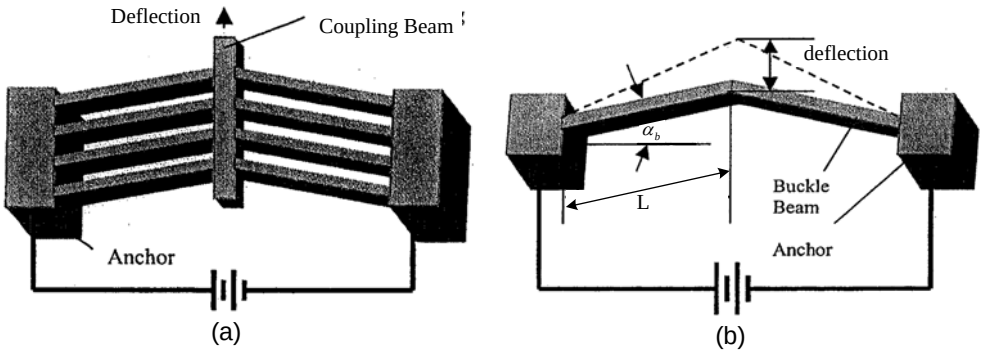

Figure 4-11: Schematic of a chevron actuator (a) an array of four buckle beam actuators with the addition of a coupling beam. The output displacement is the same as the single actuator and the output force is linear, four times that of a single actuator (b) single buckle beam actuator [7].

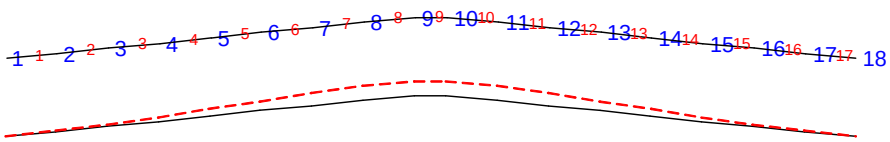

Figure 4-12: Node and element distribution along chevron actuator and deflected actuator at 4 [V].

deflection for a series of actuators with various pre-bend angles and excitation voltages. It indicates that the actuators exhibit a linear response when excitation is above 3 [V]. The slope of the curves indicated the higher the pre-bend angle, the lower the deflection.

Figure 4-12 shows the node and element distribution for the finite element analysis and the deflected shape of the actuator after applying the voltage. As shown in this figure, element 9 is the coupling beam, center section, with 5 [μm] length and width. Figure 4-13(b) shows the finite element result for the same actuator. As one can compare, the result of FEA matches the test results.

The exact analytical solution of temperature distribution for a chevron thermal actuator is shown in Figure 4-14(a) [8]. This sample was fabricated with the PolyMUMPs [77] process. This chevron actuator has two 95 [μm] half beams, hot arms, and a 5 [μm] center section, for a total length of 195 [μm], and 2 [μm] by 2 [μm] cross sectional area. Figure 4-14(b)

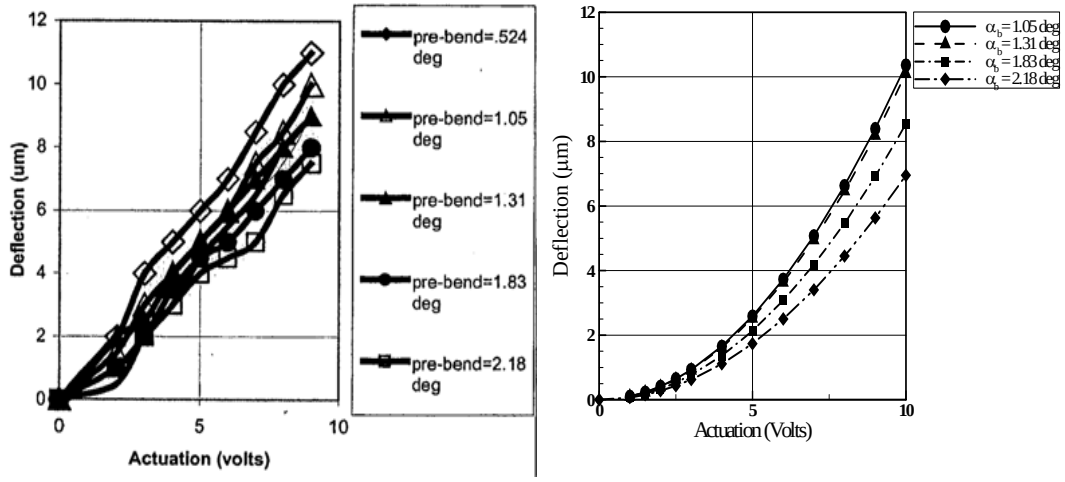

Figure 4-13: (a) Measured deflection versus actuation voltage for chevron actuators with different pre-bend angles [7] (b) finite element analysis.

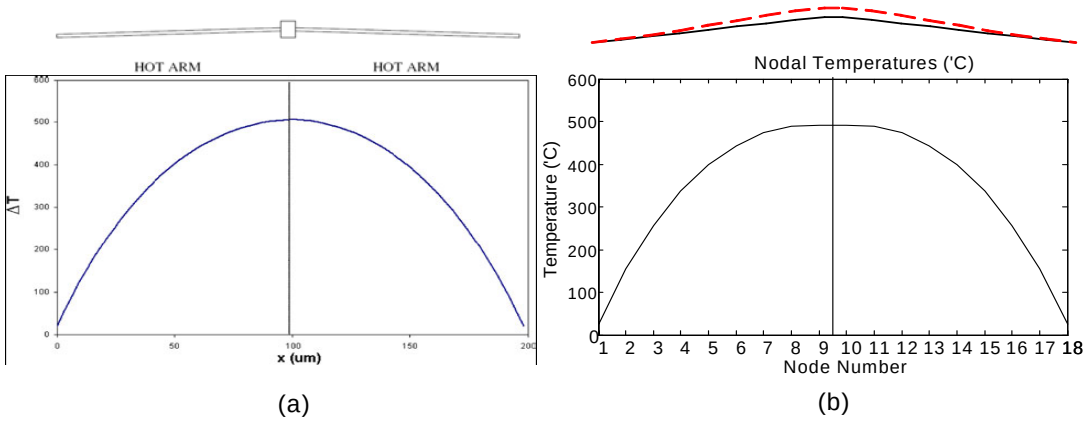

Figure 4-14: (a) Simulated analytical steady-state temperature profile along the chevron thermal actuator at 3 [V] [8] and, (b) nodal temperatures from finite element analysis.

shows the temperature distribution predicted by multi-domain FEA developed in this chapter. The maximum temperature is 500 [^{o}C] at the tip of the actuator, predicted by simplified analytical steady-state temperature profile in Figure 4-14(a) [8] and nodal temperatures from finite element analysis in Figure 4-14(b) predicts the maximum temperature with less than 1% accuracy. Again these two graphs match which indicates the validity of the analysis.

4.7 Conclusions

A new, fully-coupled field analysis method using combined MNA, resistive circuit modelling and finite element analysis was developed for an electro-thermo-mechanical domain and its results were verified with reported analytical and experimental results in the literature. Thermal dependency of material properties was implemented in the formulation to allow accurate modelling of the actuator when it undertakes large temperature changes during operation. This method of analysis serves as the core FEA solver for the topology optimization of an electro-thermo-mechanical domain, which is presented in the next chapter. Moreover, it provides a powerful tool for fast and reliable development, evaluation, and modification of electro-thermal actuators and sensors.

Chapter 5

A Novel Topology Optimization Scheme for Micro-Compliant Mechanisms with Embedded Multi-Physics Actuation

Applications of topology optimization in multi-physics problems are numerous but one very interesting application is in the systematic design of MEMS. Manufacturing and processing techniques for MEMS have reached a high level of maturity and new devices can be built in a matter of days in labs and foundries. By contrast, modelling and, in particular, development of systematic design methods for MEMS is still in its infancy. Due to the lack of existing systematic design methods for MEMS, many devices are designed using intuition, experience and trial and error approaches. Obviously, such structures cannot be optimal solutions and systematic design methods, such as topology optimization, should be able to considerably improve existing designs and develop entirely new or more efficient devices or devices with increased functionality [10]. Until now, however, no method has been able to predict better designs for MEMS.

A method that may be able to solve some of the above-mentioned problems is topology optimization. The topology optimization method solves the problem of distributing a given amount of elements freely in a design domain such that some performance criteria are maximized. In

this chapter, the method is applied to systematic design of thermal and electro-thermal micro-actuators.

Any topology optimization process involves discretization of the design domain into elements. The optimization process selectively removes elements from the domain to define an optimal topology for the design objective. In the frame-element-based approach, the design domain is discretized into a network of frame elements called the ground structure. The continuum element method uses a fictitious material density as the design variable. In contrast, the line element approach uses the in-plane width of the line elements as the design variable. The out-of-plane thickness can be fixed so that it is compatible with microfabrication processes, which make it difficult to vary device thickness continuously. Nevertheless, frame ground structure can also incorporate the cross section area of each element as the design variable.

This chapter presents an extension of previous topology optimization work, presented in Chapter 3, on design of passive MEMS. In Chapter 3, topology optimization was used to design micromanipulators, which were operated using external probes (i.e. external applied forces). To allow for on-chip actuation, the principles of thermal and electro-thermal actuations are embedded into the optimization scheme in this chapter. The result of the research described in this chapter is a novel topology scheme for electro-thermo-mechanical micro-domains.

In the following sections, the design problem is defined and the computational procedure is described.

5.1 Modelling

A common problem in micro-actuator or MEMS design is the conversion of an electrical input to a mechanical output, i.e. voltage to displacement. In the electro-thermo-mechanical actuation principle, an electrical current is converted to heat by Joule's heating and the heat then causes thermal strain, which in turn causes structural deformation. Developing a design for an efficient electro-thermo-mechanical actuator is obviously a complicated task.

The first step in the topology optimization procedure is to develop a model for the evaluation of the mechanical response of the micro-actuator subject to an applied electric or thermal field. Assuming that the geometrical changes do not influence the convection or conduction properties,

the small strain allows for modelling of the electrical and thermal fields linearly; therefore, the system is only weakly coupled in the sense that the heat equations do not depend on the elasticity equations and that the electric field equations are independent of heat equations. To simplify the equations, it is assumed that the body force and the internal electric current source are zero.

The structure to be analyzed is a sub-domain of the open domain Ω, as shown in Figure 4-1. The governing equations for a general electro-thermo-mechanical structure are as formulated in Equations (4.1)-(4.2). Note that the internal heat generation is a function of the electric field and that the stress is a function of the temperature field.

5.2 Topology Optimization Problem

Compliant structure design is motivated by the fact that the mechanism should possess enough flexibility to deform in the desired shape, yet it should contain enough stiffness to resist failure and external forces.

The concept of compliant mechanism design for single-physics of mechanical domain with force at input was addressed in Chapter 3, where mutual strain energy (MSE) and strain energy (SE) were employed as the measure of flexibility and stiffness of the mechanism. For design of a compliant mechanism, MSE is maximized, while SE is minimized, simultaneously. However, to apply the compliance theory to electro-thermal domains, the flexibility and stiffness requirements should be expressed in terms of electro-thermal inputs. To address the electro-thermal compliant mechanism design, a new formulation is proposed as described in the following sections.

In thermally and electro-thermally activated compliant mechanisms, the deformation is caused by thermal expansion of material due to change of temperature distribution. The difference with thermal actuation is that, instead of elastic strain energy, the system stores the thermal strain energy. In this chapter, the case of non-uniform temperature distribution due to an applied voltage is considered.

From Equation (4.53), the strain-stress relation with temperature change can be written as:

$$\varepsilon = C^{-1}\sigma + \varepsilon_{th} \tag{5.1}$$

where C is the matrix of material elasticity coefficients, σ is the stress distribution and ε_{th} is the thermal strain defined in Equation (4.54). In addition, initial and boundary conditions are needed to achieve the solution.

The equilibrium equation can be expressed in an integration form according to the principle of virtual work as:

$$\int_{\Omega} \varepsilon^T \sigma d\Omega = \int_{\Omega} \varepsilon^T C \left(\varepsilon - \varepsilon_{th}\right) d\Omega = 0 \tag{5.2}$$

Assuming infinitesimal strains in Equation (3.3) and $f_T = C\alpha\Delta\bar{T}$ from Equation (4.64b), Equation (5.2) is simplified in a general form as:

$$\int_{\Omega} \varepsilon^T C \varepsilon d\Omega = \int_{\Omega} \varepsilon^T f_T d\Omega = F_T \tag{5.3}$$

where f_T is regarded as the differential operator of equivalent thermal body force and F_T is the total thermal load vector from Equation (4.65).

Equation (5.3) leads to a new formulation to accommodate thermal and electro-thermal load effects in flexibility and stiffness design. This is explained in the fallowing.

5.2.1 Problem Formulation

The topology optimization of compliant mechanisms with voltage and heat actuation shares similar design criteria with the general compliant mechanism with force actuation (as described in Chapter 3). The optimization scheme follows the basic concept of a compliant mechanism, which is supposed to be flexible enough to deform and stiff enough to resist failure or an external resistance. Two types of design criteria are considered to formulate an optimization problem: flexibility requirement and stiffness requirement.

The flexibility requirement, also called the mechanisms requirement, means the designed compliant structure must be deformed in a favorable manner to complete its functionality. Mathematically, this requirement can be captured by using the concept of mutual strain energy (MSE) based on the reciprocal theorem for linear elasticity [61], [51], [26]. The mathematical representation of MSE in the case of an applied force at input port was derived in Equation (2.14). Here an improved formulation is presented that extends the compliance theory to electro-thermal boundaries.

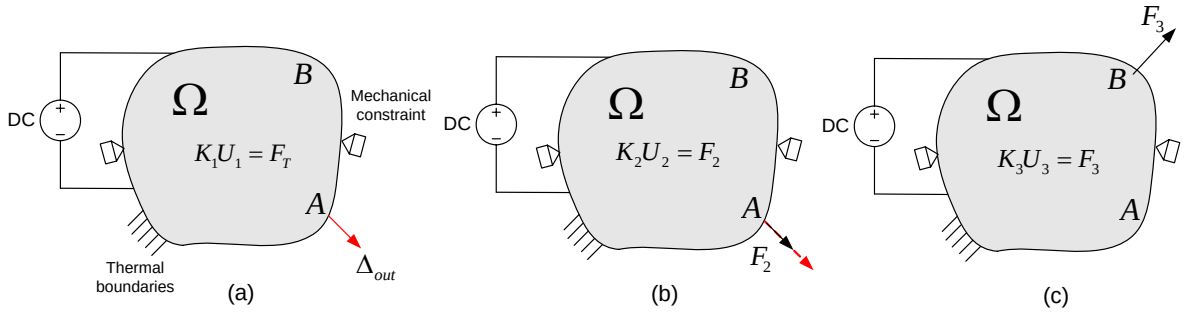

Figure 5-1: Design requirements for electro-thermo-mechanical compliant mechanism, (a) load case (1): thermal expansion, (b) load case (2): flexibility requirement, and (c) load case (3): stiffness requirement.

Considering the loading cases shown in Figure 5-1, if the displacement field in Figure 5-1(a) load case (1), denoted as U_1, caused by temperature change is used as the virtual displacement for equilibrium equation under the dummy loading case (2) (Figure 5-1(b)), the principal of virtual work can be expressed as the following:

$$\int_\Omega \varepsilon_1^T \sigma_2 d\Omega = \int_\Omega \varepsilon_1^T C \varepsilon_2 d\Omega = F_2^T U_{1A} \tag{5.4}$$

where ε_i, σ_i, U_i and F_i refer to strain, stress, displacement field, and load at loading case (i) respectively, and U_{1A} is the actual displacement at output point A due to actual forces at case (1). If U_2 is used as the virtual displacement for case (1), it results in:

$$\int_\Omega \varepsilon_2^T \sigma_1 d\Omega = \int_\Omega \varepsilon_2^T C \varepsilon_1 d\Omega \tag{5.5}$$

Considering that the loading at case (1) is, in fact, the thermal load vector F_T, Equation (5.5) is rewritten as:

$$\int_\Omega \varepsilon_2^T \sigma_1 d\Omega = \int_\Omega \varepsilon_2^T f_T d\Omega \tag{5.6}$$

The bilinear form $\Upsilon(U_1, U_2) = \int_\Omega \varepsilon_1^T C \varepsilon_2 d\Omega = F_2^T U_{1A}$ defines the mutual strain energy between case (1) and case (2). When the dummy load F_2 is a unit load, this mutual strain energy equals to the displacement at A, in the desired direction due to temperature change, denoted by U_{1A}.

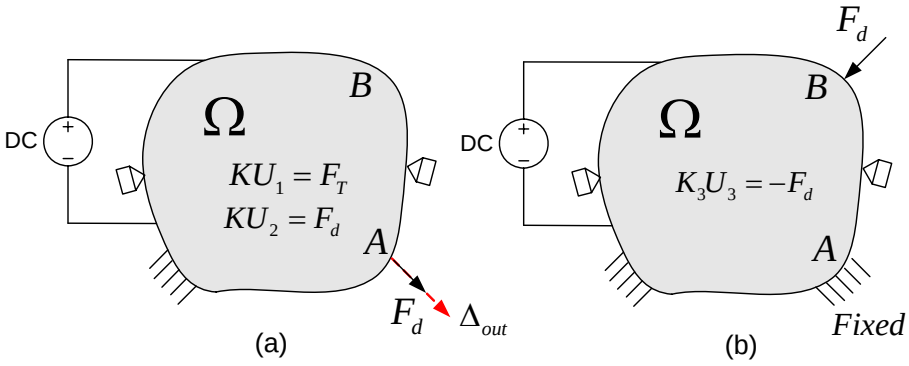

Figure 5-2: Motion transfer type mechanism design (a) flexibility requirement and (b) stiffness requirement.

The stiffness requirement provides the compliant mechanism with the internal ability to resist failure or external loading. Mathematically it can be formulated as the concept of compliance. Consider loading case (3) in Figure 5-1(c), if an external force is to be loaded to the mechanism at location B, in the form of resistive force or functioning disturbance force, the stiffness required to sustain the loading is characterized by the displacement at the loading location. Using the same displacement field as the virtual displacement:

$$\Upsilon(U_3, U_3) = \int_\Omega \varepsilon_3^T C \varepsilon_3 d\Omega = F_3^T U_{3B} \tag{5.7}$$

where U_{3B} is the displacement field at resistant point B due to resistive force F_3. When the resistive dummy force F_3 is a unit load, Equation (5.7) results in displacement at B.

The directions and locations of required flexibility, as well as those of required stiffness, need to be determined according to individual design problems. The formulation here is simplified for two general common cases: design for maximum displacement and design for maximum force.

To design a mechanism that transfers maximum displacement at point A, denoted as motion transfer type, the required flexibility is in the direction of desired output displacement at the desired location, while the required stiffness does not necessarily need to be in the similar direction or location. It can be at the stiffness resistive to input motion (or thermal expansion)

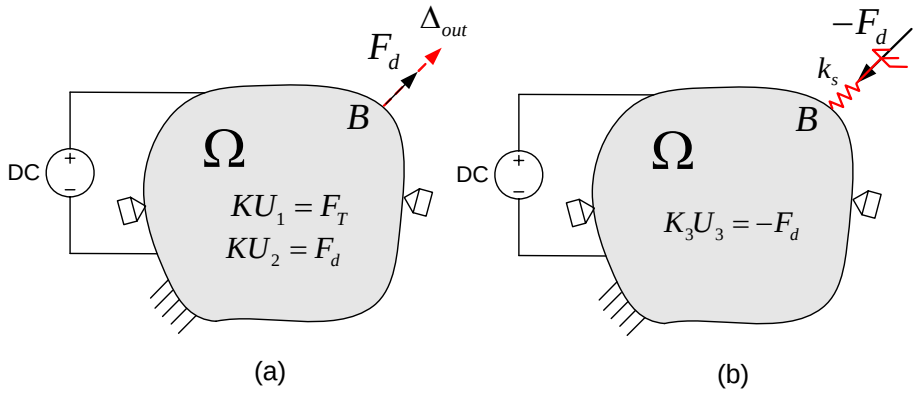

Figure 5-3: Force transfer type mechanism design (a) flexibility requirement and (b) stiffness requirement.

or any other locations and directions the specified mechanism requires (e.g. location B). This concept is the familiar MSE and SE of the system as a measure for flexibility and stiffness, where $F_2 = F_d$ is the unit dummy load in direction of desired output displacement Δ_{out} and $F_3 = -F_d$ is the unit dummy load at resistive point B. This problem is shown in Figure 5-2 and is formulated as:

$$MSE = \Upsilon(U_1, U_2) = \int_\Omega \varepsilon_1^T C \varepsilon_2 d\Omega = F_d^T U_{1A} = U_2^T K U_{1A} \tag{5.8a}$$

$$SE = \Upsilon(U_3, U_3) = \int_\Omega \varepsilon_3^T C \varepsilon_3 d\Omega = -F_d^T U_{3B} = U_3^T K_3 U_{3B} \tag{5.8b}$$

where $K_1U_1 = F_T$, $K_2U_2 = F_d$, $K_1 = K_2 = K$ and $K_3U_3 = -F_d$.

To design a mechanism that transfers force at point B, denoted as force transfer type, the required flexibility is in the direction of desired output forces at the actuation location B, while required stiffness is in the direction opposite to the output force at the same location. This concept is shown in Figure 5-3, where $F_3 = -F_d$ is a unit dummy load. This problem is formulated as:

$$MSE = \Upsilon(U_1, U_2) = \int_\Omega \varepsilon_1^T C \varepsilon_2 d\Omega = F_d^T U_{1B} = U_2^T K U_{1B} \tag{5.9a}$$

$$SE = \Upsilon(U_3, U_3) = \int_\Omega \varepsilon_3^T C \varepsilon_3 d\Omega = -F_d^T U_{3B} = U_3^T K_3 U_{3B} \tag{5.9b}$$

where $K_1U_1 = F_T$, $K_2U_2 = F_d$, $K_1 = K_2 = K$ and $K_3U_3 = -F_d$. k_s $[\mu N/\mu m]$ is a linear spring that simulates the resistance from a workpiece at output point B and K_3 is the stiffness matrix in load case (3) in Figure 5-3(b), representing the combined stiffness of the structure and the resistive spring k_s. The output force on work piece resistance is then:

$$F_{out} = U_{3B}k_s \tag{5.10}$$

5.2.2 Multi-Criteria Objective Functions

Because the compliant systems optimization is posed in terms of a set of conflicting design requirements, an optimization scheme is required to determine a compromise solution. The conflicting design objectives are handled using the multi-criteria objective function.

Mutual strain energy (MSE) as a measure of flexibility is maximized, while strain energy (SE), which is inversely proportional to the stiffness of the mechanism, is simultaneously minimized to enable the mechanism to sustain loads.

The multi-objective optimization is formulated as:

$$\begin{aligned} Maximize \quad &: \quad \Psi(MSE, \frac{1}{SE}) \\ Subject\ to \quad &: \quad \text{electrical equilibrium equations} \\ &\quad \text{thermal equilibrium equations} \\ &\quad \text{elastic equilibrium equations} \\ &\quad \text{stiffness requirement} \\ &\quad \text{flexibility requirement} \\ &\quad \text{lower and upper bounds on design variables} \\ &\quad \text{constraints} \end{aligned} \tag{5.11}$$

Using the proposed power multi-objective formula in Chapter 3, Equation(3.28), the problem

of topology optimization in finite element form is stated as:

$$Maximize: \quad (sign(MSE))^{m-1}\frac{(U_2^T K U_{1A})^m}{(U_3^T K_3 U_{3B})^n} \quad \text{Motion transfer type} \tag{5.12a}$$

$$\text{or} \quad (sign(MSE))^{m-1}\frac{(U_2^T K U_{1B})^m}{(U_3^T K_3 U_{3B})^n} \quad \text{Force transfer type} \tag{5.12b}$$

$$Subject\ to: A_{lower} \leq A_e \leq A_{upper}$$

$$V = V_0 \text{ on } \Gamma_{ED}$$

$$T = T_0 \text{ on } \Gamma_{TD}$$

$$\hat{n} k_t \nabla T = \bar{q} \text{ on } \Gamma_{TN}$$

$$u = u_0 \text{ on } \Gamma_{MD}$$

$$K_1 U_1 = F_T$$

$$K_2 U_2 = F_d$$

$$K_3 U_3 = -F_d$$

$$K_1 = K_2 = K$$

$$\Upsilon(U_1, U_1) = \int_\Omega \varepsilon_1^T f_T d\Omega$$

$$\Upsilon(U_2, U_2) = \int_\Omega \varepsilon_2^T C \varepsilon_2 d\Omega$$

$$\Upsilon(U_3, U_3) = \int_\Omega \varepsilon_3^T C \varepsilon_3 d\Omega$$

$$\Upsilon(U_2, U_1) = \int_\Omega \varepsilon_2^T f_T d\Omega$$

constraints

where A_e is the cross section area of the eth element and, A_{lower} and A_{upeer} are the lower and upper bounds on design variable, respectively.

5.2.3 Constraints

While past work had provided a great deal of insight into the fundamentals of designing compliant mechanisms, the main drawback of these approaches is that the flexibility of a structure is theoretically unbounded. Formulations that maximize flexibility have been shown to be ill-

formulated for compliant mechanism optimization [65]. As a solution, in [66], stress constraints were employed to count for failure modes. In this thesis, realizing that the stiffness objective may yield overly stiff topologies and that it may also be inadequate to model the failure criteria directly, a buckling instability constraint is employed while maximizing the output displacement. This proposed formulation, with buckling constraint, prevents long slender beams in final optimized solutions and addresses the strength of the solution, which is a major concern in current methods.

Buckling Constraint

The buckling constraint is imposed on the problem in the form of maximum force allowed in each member before buckling. During the optimization process, the axial forces in individual elements are constantly monitored so that they remain lower than the critical buckling of that element. The maximum force before buckling for a beam subject to axial load is described with Euler's limit as [89]:

$$P_E = \frac{\pi^2 EI}{(\alpha L)^2} \tag{5.13}$$

where P_E is the maximum allowed axial force before buckling, I is the area moment of inertia, L is the beam length, and α is a constant, which depends on beams boundary conditions. For typical boundary conditions, α is listed in Table 5.1 [89]. Frame elements mimic the clamped-clamped boundary condition for a beam; therefore, $\alpha = 0.5$ is used here. Although Euler's limit does not count for transverse shear effects, a new formula is proposed [89] for beams with different cross sections to explain the buckling behavior including transverse shear effect. That is [89]:

$$\bar{P} = \frac{\pi^2 EI}{(\alpha L)^2}(1 - \frac{\beta\ \bar{P}}{A\ G}) \tag{5.14}$$

where $\bar{P}$ is the maximum allowed force before buckling, A is the cross section area, G is the shear modulus and β is the cross section shape factor, where $\beta = 3/2$ and $\beta = 4/3$ for a rectangular and circular cross section, respectively [89]. Combining Equations (5.14) and (5.13) results in:

$$\bar{P} = \frac{P_E}{1 + \beta \frac{P_E}{AG}} \tag{5.15}$$

Table 5.1: Euler's buckling limit constants for beams with various boundary conditions.

Boundary Condition	α in Eq.(5.13)
clamped - free	2
clamped - clamped	0.5
clamped - pinned	0.7
pinned - pinned	1

Equation (5.15) shows that by including the transverse shear effect, the maximum allowed force is lowered before buckling occurs in a beam. By examining the terms in Equation (5.15) and the definition of P_E in Equation (5.13) one can conclude that the influence of transverse shear stiffness on beam buckling is primarily caused by a cross section shape function ($\beta L/A$) rather than a material properties function (E/G) because the E/G depends, for an isotropic material, only on Poisson's ratio, which does not vary enough to have significant effect on $\beta\frac{P_e}{AG}$. The reduction in buckling limit in Equation (5.15) is negligible for solid cross-section beams, but can approach 50% for some open cross-section beams [90]. If the forces in any element exceed the allowed limit before buckling from Equation(5.15), design variables are updated such that the buckling constraint is met.

Volume Constraint

From results of study described in Chapter 3, it was concluded that it was unnecessary to introduce a volume constraint in the optimization of micro-actuators using the present model, both because the material cost for such small devices is low and also because the initial guess for the frame ground structure does not entirely fill the design domain with material.

5.3 Implementation and Optimization Procedure

Figure 3-6 represents the flow of implementing the optimization scheme. A domain is generated and modified to the desired shape. It is then meshed, modified and boundary conditions are applied. The optimization variable and its upper and lower limits are defined. The objective function and corresponding exponents are entered. The optimization is then ready to be solved with the genetic algorithm (GA). When the convergence limit is met, the optimized design and convergence history are plotted and the data are saved in data files for further processing. Data

are filtered out and the final solution is solved using built-in finite element analysis (FEA) code from Chapter 4. The optimized design is saved and exported to IGES format. The IGES file is then transferred to other CAD based software for fabrication and further investigation.

This flow is implemented with a user-friendly graphical user interface (GUI), which will enable MEMS designers to easily define and solve their domains. Appendix A contains the detailed description of the GUI which was designed to enable the use of this topology optimization package.

5.3.1 Coupled Field Analysis

To solve the optimization problem stated in Equation (5.11) and the governing Equations (4.1)-(4.2), the design domain is discretized using a frame ground structure. The ground for employing a discretized optimization method with frame ground structure was described in Chapter 2. Moreover, in Chapter 3, the superiority of its results versus the homogenization method was proven.

As mentioned previously, the cross section of each element is the design variable. Considering the planar micro-domain, the width of the elements are a suitable design variable.

The fully-coupled analysis method for micro-domain, which was developed in Chapter 4, is used to solve the response of the design and evaluate the objective function. This fully coupled formulation is tailored for frame ground structures with multi-physics boundary conditions, coupling electrical field to thermo-elastic field using the resistive circuit method and modified nodal analysis (MNA).

5.3.2 Optimization Algorithm

The ground for choosing the genetic algorithm (GA) for the optimization was described in detail in Chapter 2. In the study of mechanical domain in Chapter 3, the chromosome was limited to binary digits. However, it has been shown that more natural representations are more efficient and produce better solutions [91]. For any GA, a chromosome representation is needed to describe each individual in the population of interest. The representation scheme determines how the problem is structured in the GA and also determines the genetic operators that are used. One useful representation of an individual or chromosome for function optimization involves

genes or variables from an alphabet of floating point numbers with values within the variables upper and lower bounds. In [91], extensive experimentation is done comparing real and binary coded GAs and shows that the real-valued GA is an order of magnitude more efficient in terms of CPU time. It is also shown that a real-valued representation moves the problem closer to the problem representation, which offers higher precision with more consistent results across replications [91].

As mentioned previously, in the topology optimization scheme presented here, design variables are considered as continuous variables allowed to take intermediate values in the constrained upper and lower bounds. To meet the nature of the problem, an efficient, real-coded GA with elitism is developed in Matlab as the core optimization solver.

Real-Coded Genetic Algorithm

Figure 5-4 shows the flow chart of the implemented GA. The initial population is generated by populating real valued random numbers between the upper and lower bounds up to the specified size of the initial population. A normalized Geometric Selection function is employed to rank the population and reproduction is performed using non-uniform mutation and heuristic crossover operators [91]. The GA is coded with elitism. After creating a new population by crossover and mutation, at least one best solution is copied without changes to the new population, so the best solution found can survive. Elitism can very rapidly increase performance of the GA, because it prevents losing the best found solution. The GA moves from generation to generation selecting and reproducing parents until a termination criterion is met. The GA structure may be resumed as follows:

1. Supply a population P_0 of N individuals and respective function values.
2. $i \leftarrow 1$
3. $P_i' \leftarrow$selection function $(P_i - 1)$
4. $P_i \leftarrow$reproduction function (P_i')
5. evaluate (P_i)
6. $i \leftarrow i + 1$

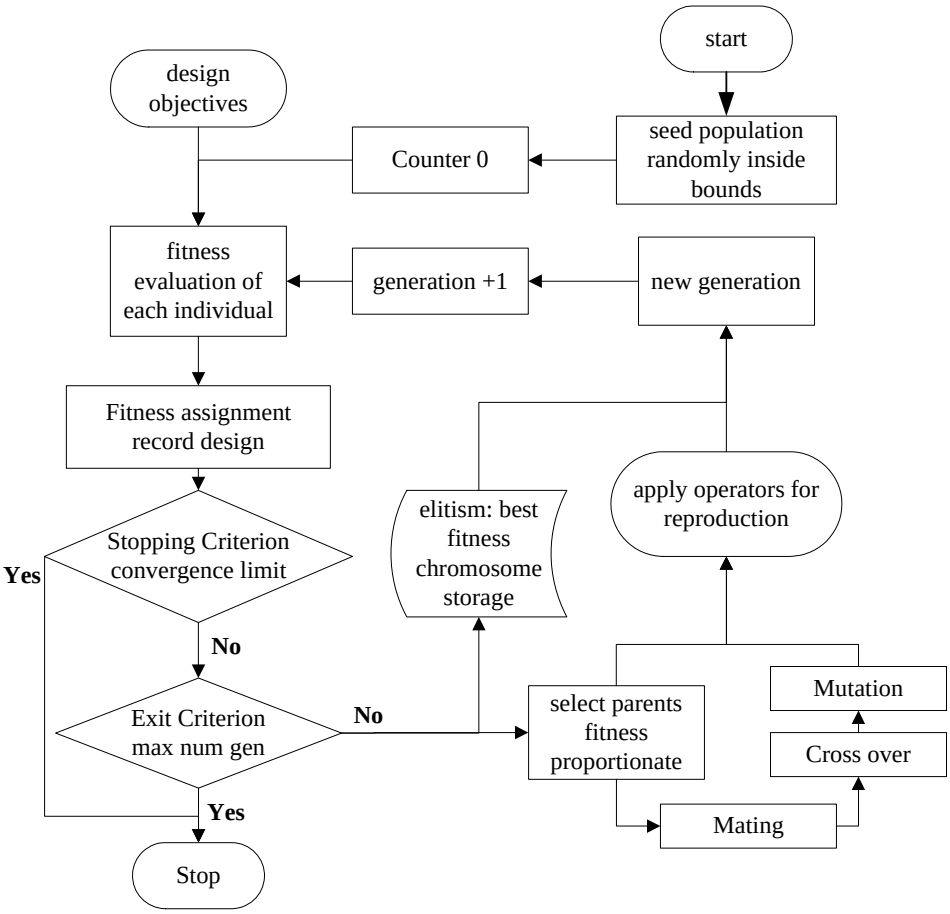

Figure 5-4: Flow chart of implemented real-coded genetic algorithm with elitism.

7. Repeat step 3 until termination

8. Print out best solution fond

Two criterion are set to terminate the GA: 1) meeting the convergence criterion or 2) lack of improvement in the best solution over a specified number of generations. In the following, each of the major components of the implemented GA is discussed.

Initialization The GA must be provided by an initial population. Initial population is generated by populating real-valued random numbers between upper and lower bounds up to the specified size of the initial population, e.g. 100 to 500 times the number of elements. If the

initial population seeded to the code is empty or the number of population is less than specified, automatically a set of random solutions are added to the population, preserving the initial individuals. For example, the beginning population might be seeded with potentially good solutions, with the remainder of the population being randomly generated solutions.

Elitism The implemented GA is coded with elitism to improve the convergence behavior. Elitism can very rapidly increase the performance of the GA, because it prevents loss of the best found solution. After creating a new population by crossover and mutation, if the algorithm has not yet converged, at least one best solution is copied to next generation without changes to the new population, so the best solution found can survive.

Selection Function The selection of individuals to produce successive generations plays an extremely important role in a GA. A probabilistic selection is performed based on the individual's fitness, such that the better individuals have an increased chance of being selected. An individual in the population can be selected more than once, with all individuals in the population having a chance of being selected to reproduce into the next generation. There are several schemes for the selection process: roulette wheel and its extensions, scaling techniques, tournament, elitist models, and ranking methods [71].

Ranking methods require the evaluation function to map the solution to a partially ordered set, thereby allowing for minimization and negativity. Ranking methods assign P_i based on the rank of solution i when all solutions are sorted. Normalized Geometric Selection is used as follows.

Normalized Geometric Selection Normalized Geometric Selection is a ranking selection function based on the normalized geometric distribution. Normalized geometric ranking defines P_i for each individual by [92]:

$$P_i = q'(1-q)^{r-1} \tag{5.16}$$

where P_i is the probability of selecting the ith individual and r is the rank of the individual, where 1 is the best and $r = U(0,1)$:

$$\begin{aligned} q &= \text{the probability of selecting the best individual} \\ P &= \text{the population size} \\ q' &= \frac{q}{1-(1-q)^P} \end{aligned} \tag{5.17}$$

GA Operators Let $\bar{X}$ and $\bar{Y}$ be two n-dimensional row vectors denoting n individuals (parents) from the population. Operators for real-valued representations, i.e. an alphabet of floats, were developed in [91]. A non-uniform mutation and heuristic crossover are chosen as the GA operators here.

Non-uniform mutation For real valued $\bar{X}$ and $\bar{Y}$, the non-uniform mutation was selected. non-uniform mutation randomly selects one variable, j, and sets it equal to a non-uniform random number [93]:

$$x_i^{'} = \begin{cases} x_i + (x_{upper} - x_i) f(G_r) & \text{if} \quad r_1 < 0.5 \\ x_i - (x_{lower} + x_i) f(G_r) & \text{if} \quad r_1 \geq 0.5 \\ xi & \text{otherwise} \end{cases} \tag{5.18}$$

where x_{lower} and x_{upper} are the lower an upper bound for variable i, respectively and

$$\begin{aligned} f(G_r) &= \left(r_2 (1 - \frac{G_r}{G_{\max}} \right)^b \\ r_1, r_2 &= \text{a uniform random number between (0,1)} \\ G_r &= \text{the current generation number} \\ G_{\max} &= \text{the maximum number of generations} \\ b &= \text{a shape parameter} \end{aligned} \tag{5.19}$$

Heuristic Crossover Heuristic crossover produces a linear extrapolation of the two individuals. Heuristic crossover was chosen because it is the only operator that utilizes fitness information. A new individual $\bar{X}'$ is created using Equation (5.20a), where $r_3 = U(0,1)$ and $\bar{X}$

is better than $\bar{Y}$ in terms of fitness [93].

$$\bar{X}' = \bar{X} + r_3(\bar{X} - \bar{Y}) \tag{5.20a}$$
$$\bar{Y}' = \bar{X}$$

If $feasibility$ of $\bar{X}'$ equals zero, as given by Equation (5.21), then it generates a new random number, r_3, and creates a new solution using Equation (5.20a), otherwise crossover stops. To ensure halting after t_r failures, it lets the children equal the parents and stops.

$$feasibility = \begin{cases} 1, \text{ if } x'_i \geq x_{lower},\ x'_i \leq x_{upper}\ \forall i \\ 0, \text{ otherwise} \end{cases} \tag{5.21}$$

Termination Criteria The GA moves from generation to generation selecting and reproducing parents until a termination criterion is met. Two criterion are set to terminate the GA. One is a specified maximum number of generations. Another termination strategy involves population convergence criteria, ϵ_G. In general, GAs force much of the entire population to converge to a single solution. When the sum of the deviations among individuals becomes smaller than specified threshold ϵ_G , the algorithm is terminated. Also the algorithm is terminated due to a lack of improvement in the best solution over a specified maximum number of generations, $G_{\max}$.

If the maximum number of generations is reached and the algorithm has not yet converged, a warning message will show that: "Maximum number of generations reached without termination criterion met. Either increase maximum generations or ease termination criterion."

Default values The default values for the GA operators are listed in Table 5.2; however, these parameters can be adjusted for specific needs of the problems. The listed parameters are described previously in formulations.

5.3.3 Design Issues

The optimized solution depends on the lower limits on the design variable. In MEMS applications, the bounds on design variables are constrained by the fabrication process limits. For

Table 5.2: Default values for GA algorithm operators.

GA Operator	Input parameter	default values
Initial population size	P	300×number of elements
Normalized Geometric Selection	q	0.08
Heuristic Cross Over	t_r	2
Non Uniform Mutation	b	3
Termination Criteria	ϵ_G	1e-6
Maximum number of generations	$G_{\max}$	300

instance, the minimum width of the beam element cannot be less than 2 [μm] using multi user microfabrication techniques. The conventional element elimination policies are to remove beam members whose design variables reached the lower bound constraint, after algorithm converges. But in MEMS, elements on or close to the lower bound, e.g. 2 [μm] , still significantly contribute to the stiffness of the structure. If these elements are eliminated, the resulted structure may not perform as desired. This issue is addressed by a new element removal policy for topology optimization in MEMS.

The minimum feasible geometric limits on design variables are usually defined with fabrication and lithography process limitations. Minimum dimensions are always subject to fabrication tolerance limits in a typical MEMS process. For example, if the design rule for minimum feature is 2 [μm] in design, and the lithography tolerance is $\delta_f = \pm 0.1$ [μm] on the minimum feature, 2 [μm] elements on wafer will have a distribution between 1.9 [μm] to 2.1 [μm]. It is preferred then to keep the elements inside the fabrication limit at the lower bound.

As a solution, at the start of the algorithm, the lower bound is modified to account for the fabrication tolerance provided by the designer as $x_{low} - |\delta_f|$. After the algorithm converges, the optimized solution contains elements at the modified bound of $x_{low} - |\delta_f| \leq x_i \leq x_{up}$. In the optimization process, a filtering scheme is implemented that allows the designer to preserve elements at the vicinity of the modified lower bound. The filtering factor, Δ_f is defined as:

$$\Delta_f = \frac{x_i + |\delta_f| - x_{low}}{x_{up} - x_{low}} \tag{5.22}$$

where $0 \leq \Delta_f \leq 1$. Elements with $\Delta_f < 0$ will be permanently removed from the mesh in post processing. For example, if the upper and lower bounds on the design variable are defined as $2 \leq x_i \leq 5$ and minimum feature tolerance is $\delta_f = \pm 0.2$ [μm], the optimized topology contains

elements at lower bound of 1.8 [μm].It might be desired to preserve the elements with a 1.8 [μm] design variable, which is achieved through filtering out with $\Delta_f = 0$. However, if the designer decides to keep the elements at the ± 0.1 vicinity of lower bound, then the optimized configuration is filtered out with:

$$\Delta_f = \frac{1.9 + 0.2 - 2.0}{5.0 - 2.0} = 0.0333 \tag{5.23}$$

Applying a filtering factor equal to 0.0333 preserves all the elements at 1.9 [μm] and higher and elements with less than 1.9 [μm] will be permanently removed in post processing.

5.4 Conclusions

Results presented in this chapter indicate that the topology optimization method can produce highly efficient micro-actuators. Topology optimization of MEMS devices was formulated and the genetic algorithm was discussed as a solver.

In the next chapter, the proposed topology optimization scheme is applied to the design of compliant thermal and electro-thermal micro-actuators. The performance values for the electro-thermal actuators are compared with the performance of a finite element model in ANSYS [11]. Furthermore, some examples of optimized configuration of electro-thermal actuators are presented and their performances are validated.

Chapter 6

Numerical Examples and Verification

In this chapter, numerical examples of the novel optimization scheme proposed in Chapter 5 are presented. The performance of the optimized actuators are extensively studied using the fully-coupled analysis method developed in Chapter 4, with the resistive circuit method, modified nodal analysis and finite element. For further verification, the performance and robustness of the optimized topologies are validated with finite element analysis in ANSYS [11] and, if applicable, with their counterparts from the available literature.

The design domain is two dimensional considering the planar nature of MEMS processes. The effect of strain gradient and average residual stress in the thin film is neglected and the out of plane deflection in the optimum design is zero, which is also confirmed in 3D ANSYS simulations in this Chapter. However, the out of plane deflection may occur in some of the beam members due to thermal buckling if the applied voltage exceeds the input requirement. The buckling constraint however, prevents appearance of buckling members in the optimized topology at the applied voltages close to specified input voltage.

This chapter covers three design examples, with the following objectives:

1. Compare results obtained by the frame element approach with both intuitive designs and designs from the continuum element approach reported in the literature and verification of results with ANSYS [11] models.

2. Study the influence of the specification for force transfer and motion transfer type mechanisms on the resulting optimal designs.

3. Illustrate the influence of the varying workpiece resistance on the final optimal design.

4. Demonstrate the ability of the optimization procedure to generate non-intuitive topologies.

6.1 Example 1: Voltage Activated Micro-Manipulator

A compliant electro-thermal micro-manipulator is a one piece device that can effectively transmit precise horizontal motion due to applied voltage at input ports. Micro-manipulators have numerous applications in MEMS, including motion amplifiers.

6.1.1 Design Domain

The design domain of a voltage activated micro-manipulator is shown in Figure 6-1. An optimized actuator is desired to have maximum deflection in output direction Δ at prescribed location, subject to 0.5 [V] applied voltage and thermal and mechanical boundary conditions at anchors. Output direction Δ is defined with vector [1,0] denoting that, at the target output location, the actuator moves only in X direction and should have no vertical movement, where X and Y are the coordinates of the $2D$ space, as shown in Figure 6-1.

In Figure 6-2 the resulting optimized mechanism from the homogenization method is shown [9]. As seen in Figure 6-2(b), the optimized design has gray materials which do not interpolate as either void or filled material. This layout needs manual interpolation in order to transfer to fabrication layout. Further, it is noted that the two ports of the voltage are shorted through the thick arm in the left side of the design domain. The performance of this design is not reported in the literature for comparison [9], but study of the optimized configuration raises the feasibility question.

The material for the design is assumed to be electroplated Nickel. Material properties of electroplated Nickel are listed in Table 6.1. These material properties are not exactly equal to the bulk values of Nickel and are found from literature [33, 94, 95]. Electroplated nickel is selected due to its suitability for electro-thermal actuator design, although the topology

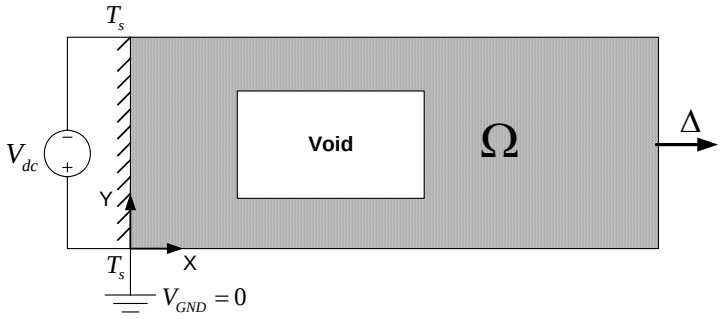

Figure 6-1: Design domain and problem specification for electro-thermal actuator in Example 1.

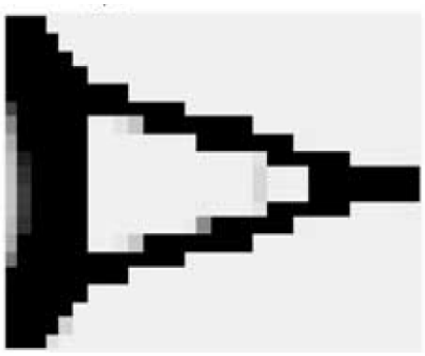

Figure 6-2: Optimal solution for design of example 1 reported in [9]. The presence of gray material and a short loop of voltage through the left arm of the design is observed. The performance of the actuator is not reported in [9].

Table 6.1: Material properties of Electroplated Nickel and geometrical dimensions for the electro-thermal micro-actuator in Example 1.

Material Properties		
Property	Value	Unit
Young's modulus E of Nickel	200×10^6	MPa
Thermal expansion coefficient α of Nickel	13.4×10^{-6}	C^{-1}
Thermal conductivity of Nickel k	90.7×10^{-6}	$W\mu m^{-1}C^{-1}$
Thermal conductivity of air k_{air}	0.03×10^{-6}	$W\mu m^{-1}C^{-1}$
Resistivity of Nickel	67×10^{-3}	$\Omega - \mu m$
Geometrical Data		
Design domain dimensions	200×100	μm
Void domain dimensions	50×50	μm
V_{dc}	0.5	V
Thickness	2	μm
air gap to substrate δ	2	μm
T_s	0	$^\circ C$
T_∞	25	$^\circ C$

optimization scheme is not limited to a specific material or fabrication process and any available material can be used. Dimensions of the design domain Ω, as listed in Table 6.1, are 200 [μm] by 100 [μm] and it has an out-of-plane thickness of 2 [μm]. The void area is shown in white. The substrate temperature is 0 [^oC] and the surrounding air is at room temperature of 25 [^oC]. The in-plane width of elements is the design variable with lower and upper bounds of 1 [μm] and 5 [μm], respectively.

6.1.2 Problem Statement using the Proposed Topology Optimization

The design specifications are that an applied voltage, V_{dc}, causes the motion, Δ, in the horizontal direction. The multi-criteria objective function in Equation (5.12a) was employed, where $m = 2$ and $n = 1$ and the buckling constraint is active. The choice of exponents for the objective function was made by considering that design specifications require a maximum motion transfer

type mechanism. The optimization problem is then formulated as:

$$Maximize : sign(MSE)(\frac{MSE^2}{SE}) \tag{6.1}$$

$$Subject\ to : 1 < w_e < 5\ \mu m$$

$$F_e < \bar{P}$$

$$k_s = 0$$

electrical equilibrium equations

thermal equilibrium equations

elastic equilibrium equations

flexibility requirement

stiffness requirement

Convergence criteria =1e-6

Δ in the direction of [1,0]

where w_e is the in-plane width of element e and is the design variable for the optimization algorithm and $\bar{P}$ is the maximum allowable force before buckling from Equation (5.15).

Figure 6-3(a) shows the initial frame ground structure with applied boundary conditions and output specification. The initial guess is randomly generated between upper and lower bounds. In order to maximize the design objective while satisfying the constraints, the algorithm changes the value of the design variables in each iteration so that the uneconomical members tend toward the lower bound constraints and the economical members tend toward the upper bond constraints. The optimal solution is the most efficient arrangement of beam members in terms of design objective and constraints.

The initial ground structure consists of 45 nodes and 109 beam elements. Initial population is randomly generated between upper and lower bounds. For fabrication feasibility, variables can have numbers in 0.1 [μm] increments. The design specification requires a motion transfer mechanism where $k_s = 0$.

6.1.3 Optimized Configuration

The optimized frame configuration is shown in Figure 6-3(b), which consists of 40 nodes and 88 beam elements; node 22 is the desired output location. The real-coded GA converges after 98 iterations, as shown in Figure 6-4.

After the algorithm converges, the optimized configuration is analyzed with a built-in FEA code, as described in Chapter 4, and nodal and element data files are saved for further study. The actual layout of the actuator is shown in Figure 6-3(c), where dashed lines show the deformed shape at 0.5 [V]. The displacement field is scaled for better illustration. The variation in the element sizes shown in Figure 6-3(c) actually represents the in-plane widths of the remaining elements.

As shown in Figure 6-3(c), the top and bottom arms move 2 [μm] in Y direction to allow a 7.3 [μm] forward deflection in X direction at output node 22. It is noted that output has no vertical displacement and is only moving in specified direction of Δ to satisfy the design requirement. The deformation of the actuator in Figure 6-3(c) confirms that the resulting mechanism is a fully compliant mechanism in which the whole body deforms to transfer the output deflection. Achieving a fully compliant design was one of the main targets of the optimization scheme and has been successfully implemented.

6.1.4 Verification

The performance of the optimized electro-thermal actuator is extensively studied here. For verification, its performance from built-in FEA is compared with solid model finite element in ANSYS [11]. The schematic layout in Figure 6-3(c) was automatically transferred to IGES format using the fabrication module of the graphical user interface (GUI), designed for this optimization package (Appendix A). Figure 6-5(a) shows the optimized actuator in IGES format. The IGES file was then imported into ANSYS [11] to built the solid model. Boundary conditions were applied and the solid model was meshed with SOLID 226, which is a 3D 20-node coupled-field element with displacement, voltage and temperature degrees of freedom [11]. The model was simulated with large deflections activated in ANSYS. Figure 6-5(b) shows the deformed meshed solid and undeformed edge of the actuator at 0.5 [V] in ANSYS [11].

In Figure 6-6 the maximum deflection at output location in X direction and the maximum

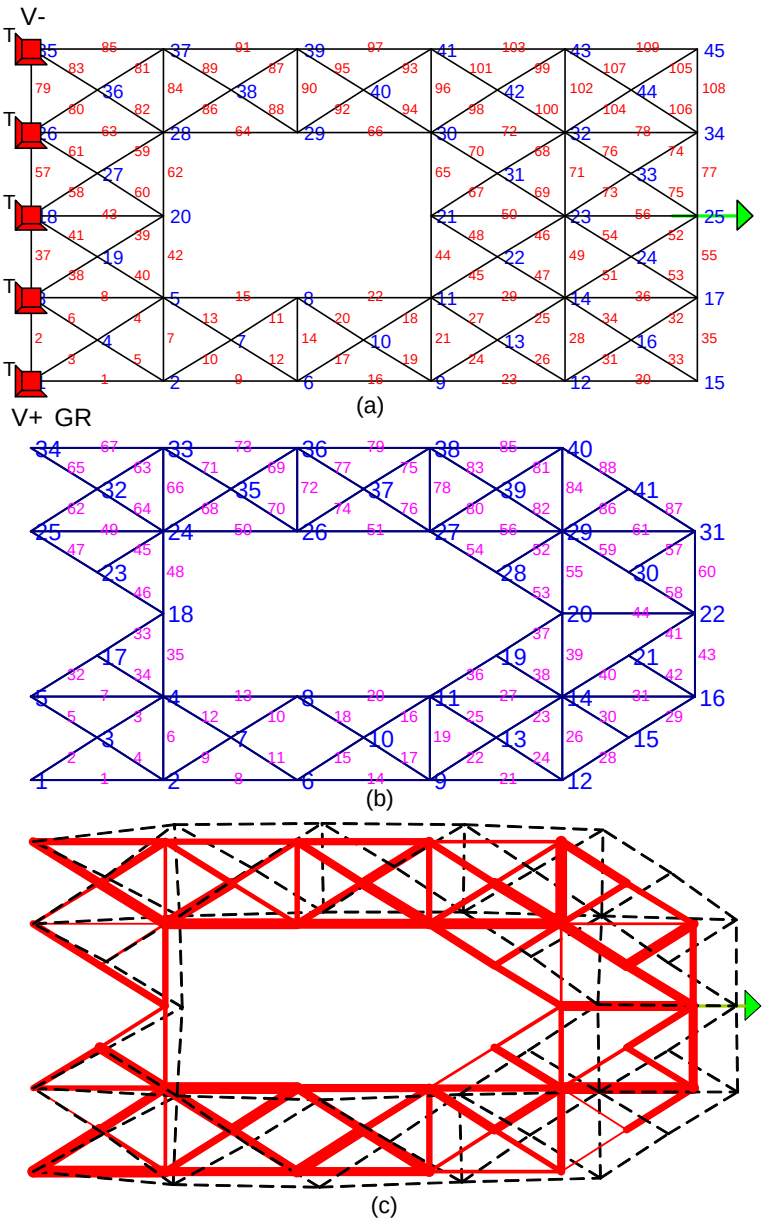

Figure 6-3: (a) Initial frame ground structure of Example 1, (b) optimized frame structure after convergence which contains 41 nodes and 88 elements, and (c) layout schematic of the optimized actuator, solid lines presents the remaining elements and dashed lines denote the deflected shape at 0.5 [V].

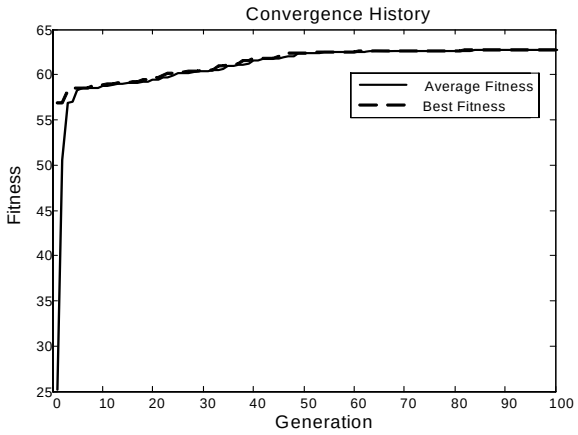

Figure 6-4: Convergence history of genetic algorithm for Example 1.

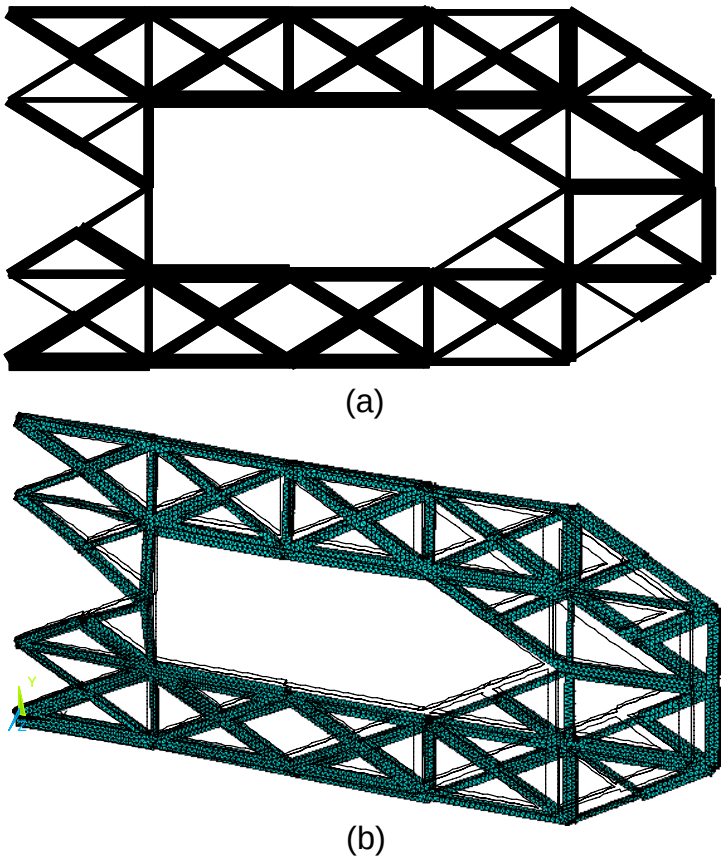

Figure 6-5: (a) Optimized topology of actuator transferred to IGES format (b) Solid model in ANSYS showing deformed shape and undeformed edge of the actuator at 0.5 [V].

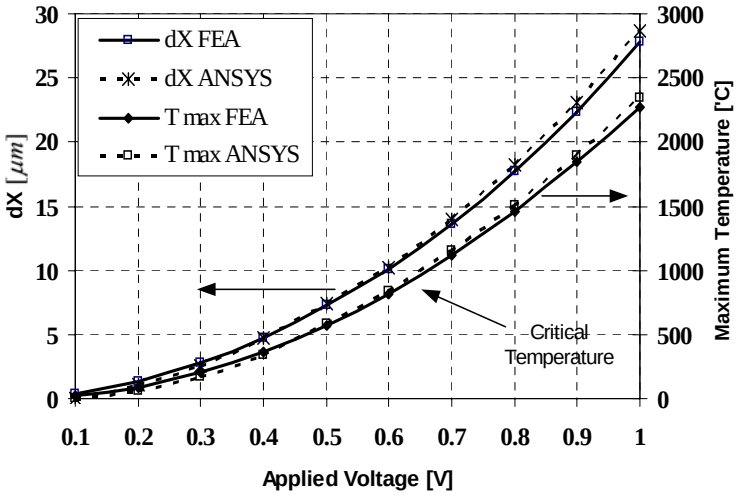

Figure 6-6: Comparison of maximum deflection dX at output node 22 and maximum temperature in the body from the FEA solver and ANSYS model for 0 [V] to 1 [V]. The operation range of the actuator is 12 [μm] at 0.65 [V], set by the critical temperature of Nickel at 800 [^oC].

temperature in the body of actuator for 0 [V] to 1 [V] are plotted. This figure compares the results from the FEA solver in the optimization package and the ANSYS [11] solid model. As seen in the figure, the FEA results agree with ANSYS with less than 1% error. It is concluded that the optimized topology is meeting the design specifications and that FEA formulation can precisely predict actuator performance. This plot also helps to understand the range of operation of the actuator. As shown in Figure 6-6, the maximum operation range of the actuator is 12 [μm] at 0.65 [V], which is set by critical temperature of Nickel at 800 [^oC]. At the specified operation point of 0.5 [V], the maximum temperature in the body is 570 [^oC], which is well bellow critical point.

To further study and verify the performance of the actuator, in Figures 6-7(a) and (c) nodal displacement solutions dX and dY are compared with ANSYS results in Figures 6-7(b) and (d) at operation point of 0.5 [V]. Node numbers in Figures 6-7(a) and (c) are referenced to the optimized frame structure in Figure 6-3(b). As seen in these figures, node 22, the specified output node, has the maximum dX of 7.3 [μm], which is confirmed with ANSYS model in Figure 6-7(b) with maximum $dX = 7.253$ [μm] with less than 0.7% error. Figures 6-8(a)

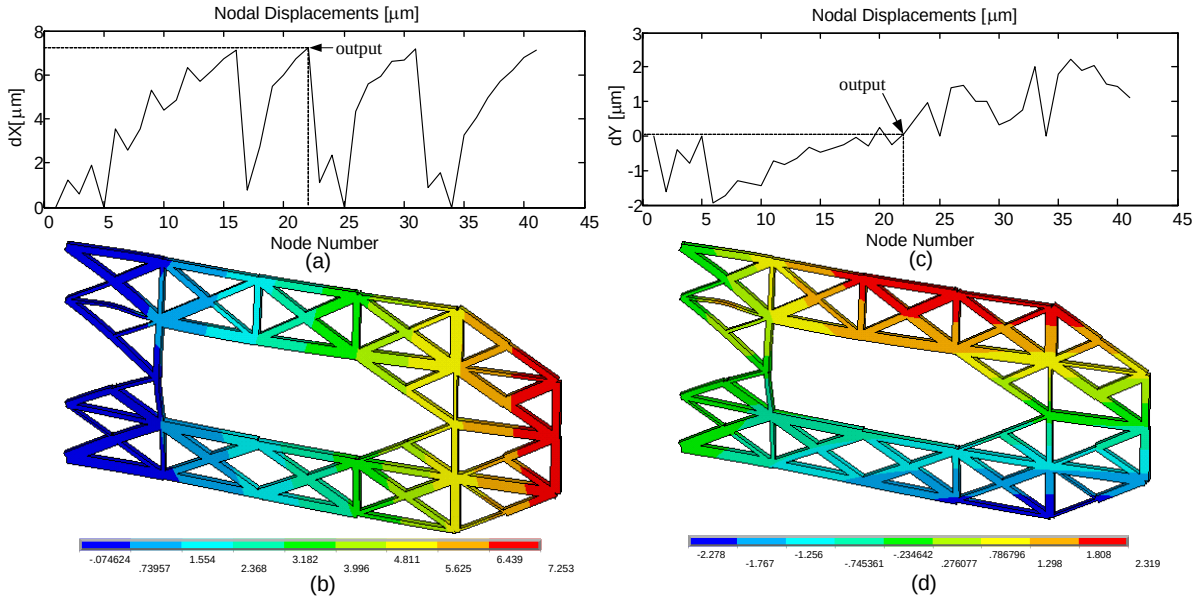

Figure 6-7: Comparison of (a) nodal dX solution from the FEA, (b) dX from ANSYS, (c) nodal dY solution from the FEA and (d) dY from ANSYS.

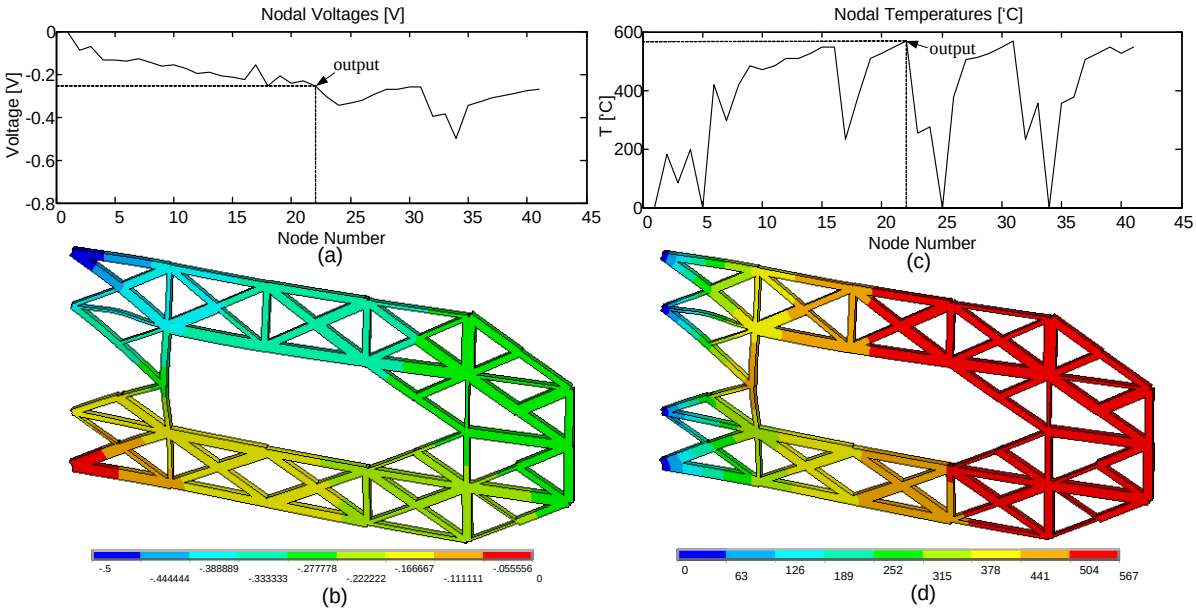

Figure 6-8: Comparison of (a) nodal voltage values from the FEA, (b) voltage distribution in ANSYS, (c) nodal temperature values from the FEA and (d) temperature distribution in ANSYS.

and (b) show the nodal voltage values from the FEA and the voltage distribution in ANSYS, respectively. The voltage is distributed in a loop from 0 [V] to -0.5 [V] between DC source terminals. Voltage at output node 22 is -0.248 [V], which is also verified in the ANSYS model with a specified value of -0.25 [V] with less than 0.9% error.

The nodal temperatures from the FEA are plotted in Figure 6-8(c) and compared to temperature distribution from ANSYS in Figure 6-8(d). The prescribed temperature value at anchor points is 0 $[^0C]$ and the FEA predicts the maximum temperature of 570 $[^oC]$, which agrees with 567 $[^oC]$ in ANSYS with 0.5% error.

The comprehensive study of the optimized topology confirms the following observations:

- Comparison of Figures 6-7(b) and (d) shows that the output node has close to zero deflection in Y direction, satisfying the design specification of direction Δ.
- It is noted that the active buckling constraint effectively prevents the presence of long unsupported beams in the optimized configuration to impose the strength constraint on the final solution.
- The resulted topology encompasses the fully distributed compliant characteristic. The actuator is expanding as a whole to transfer the motion.
- The built-in, fully-coupled FEA can precisely predict the behavior of the optimized actuator. Reliability of the built-in FEA code eliminates the necessity of transferring the solution to commercial software for further simulations.
- The resulted topology can easily be mapped for fabrication through the available GUI in Appendix A.
- Comparison of the optimized configuration from the proposed method with results of homogenization method in Figure 6-2(b) verifies that frame elements are a more suitable choice for MEMS domain. The performance of the actuator in Figure 6-2 is not reported for comparison [9].

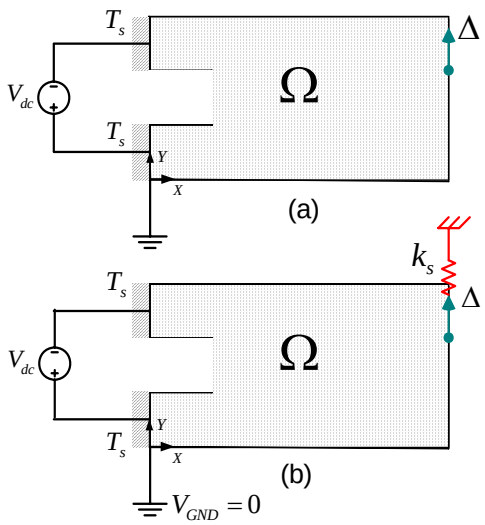

Figure 6-9: (a) Motion transfer and (b) force transfer electro-thermal actuator design domain and corresponding boundary conditions, where $k_s = 100$ $[\mu N/\mu m]$.

6.2 Example 2: Electro-thermal Compliant Actuator, ETC

In this example, to further demonstrate the advantages of the proposed method, examples of optimized electro-thermo-mechanical actuators are compared with available results of homogenization method in the literature [33, 94, 10].

6.2.1 Design Domain

As an example, design of an electro-thermal micro-actuator, sketched in Figures 6-9(a) and (b), is considered and results are compared with reported topologies in [33] and [10] from homogenization method. The design domain is rectangular and dimensions are listed in Table 6.2. The left edge has two terminals where a prescribed voltage V_{dc} is applied. A rectangular domain shown in white is fixed to be void. The actuators are fabricated with electroplated Nickel. Material properties of Nickel are listed in Table 6.1. The optimization consists in maximizing the deflection Δ at the output point in the desired shown direction Δ, for two cases:

a) Motion transfer mechanism as sketched in Figure 6-9(a). The optimized topology is desired to transfer the maximum deflection at output location in direction of Δ.

Table 6.2: Geometrical dimensions for the electro-thermal actuator in Example 2.

Geometrical Data		
Design domain dimensions	500×150	μm
Void domain dimensions	200×50	μm
V_{dc}	0.4	V
Thickness	7	μm
air gap to substrate δ	2	μm
T_s, T_∞	0	$^\circ C$

b) Force transfer mechanism as sketched in Figure 6-9(b). The optimized topology is desired to transfer the maximum deflection at the output location in the direction of Δ at he presence of a workpiece resistance at output. Linear spring $k_s = 100$ $[\mu N/\mu m]$ simulates the resistance from a workpiece at the output point.

6.2.2 Problem Statement

The design specifications are that an applied voltage, V_{dc}, causes the motion, Δ, in the vertical direction. The direction of the desired output displacement is specified in terms of a unit vector [0,1]. The optimization problem is formulated as:

$$Maximize : \frac{MSE}{SE} \tag{6.2}$$

$$Subject\ to : 1 < w_e < 8\ \mu m$$

$$F_e < \bar{P}$$

$$k_s = 0,\ 100\ [\mu N/\mu m]$$

electrical equilibrium equations

thermal equilibrium equations

elastic equilibrium equations

flexibility requirement

stiffness requirement

Convergence criteria =1e-5

Δ in the direction of [0,1]

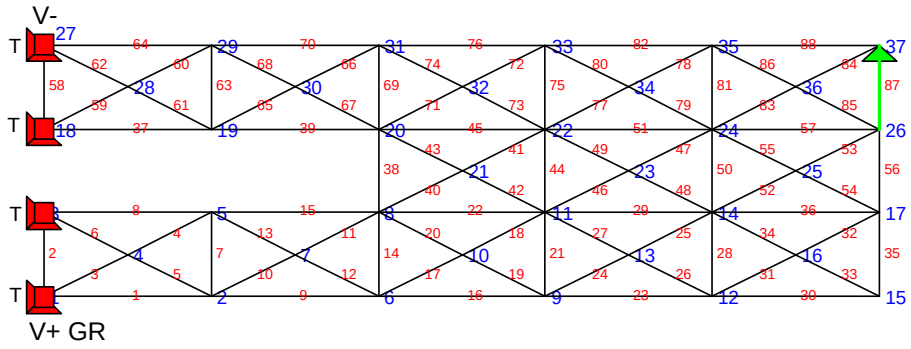

Figure 6-10: Design domain and boundary conditions of an electro-thermal actuator, discretized with frame elements.

where w_e is the in-plane width of element e and is the design variable for optimization algorithm. Boundary conditions applied to equilibrium equations are shown in Figure 6-9. The initial guess is randomly generated between the upper and lower bounds. For fabrication feasibility, variables can have numbers in 0.1 [μm] increments. In order to maximize the design objective while satisfying the constraints, the algorithm changes the value of the design variables in each iteration so that the uneconomical members tend toward the lower bound constraints and the economical members tend toward the upper bond constraints. The optimal solution is the most efficient arrangement of beam members in terms of design objective and constraints.

Power coefficients of the objective function are chosen as $m = n = 1$ to provide a balanced objective function for both motion transfer and force transfer designs.

6.2.3 Optimized ETC Configuration

The design domain is discretized and boundary conditions are applied, as shown in Figure 6-10.

The optimized topologies are shown in Figure 6-11 (a) and (b) for motion transfer and force transfer mechanisms, respectively. Figure 6-12 (a) and (b) shows the algorithm convergence history in both cases. As shown in the figures, for both cases, the algorithm converges in less than 100 iterations. This is one of the advantages of the implemented GA over other gradient-based methods applied in the literature, which usually require more than 500 iterations to converge.

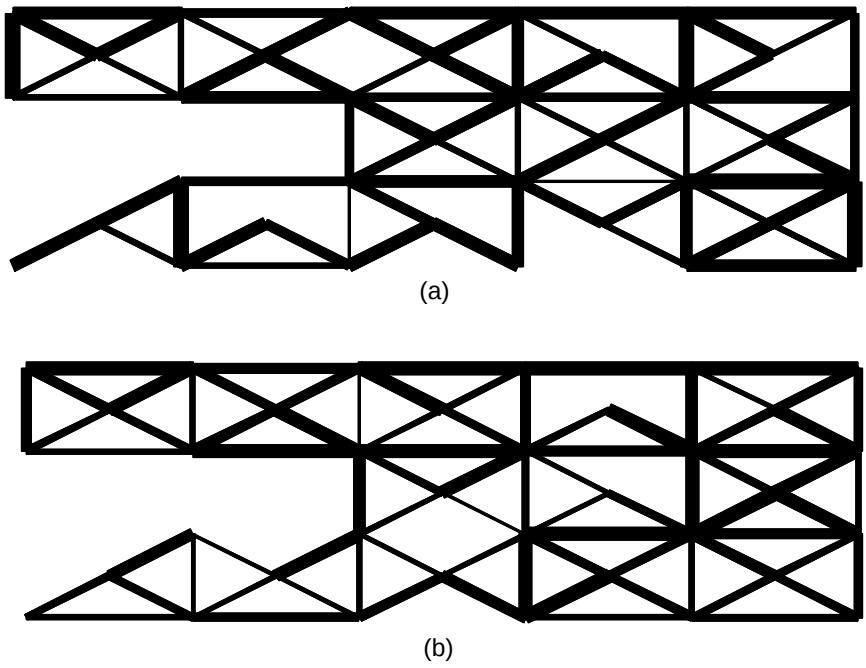

Figure 6-11: Optimized topology of (a) motion transfer electro-thermal actuator and (b) force transfer electro-thermal actuator where $k_s = 100$ $[\mu N/\mu m]$.

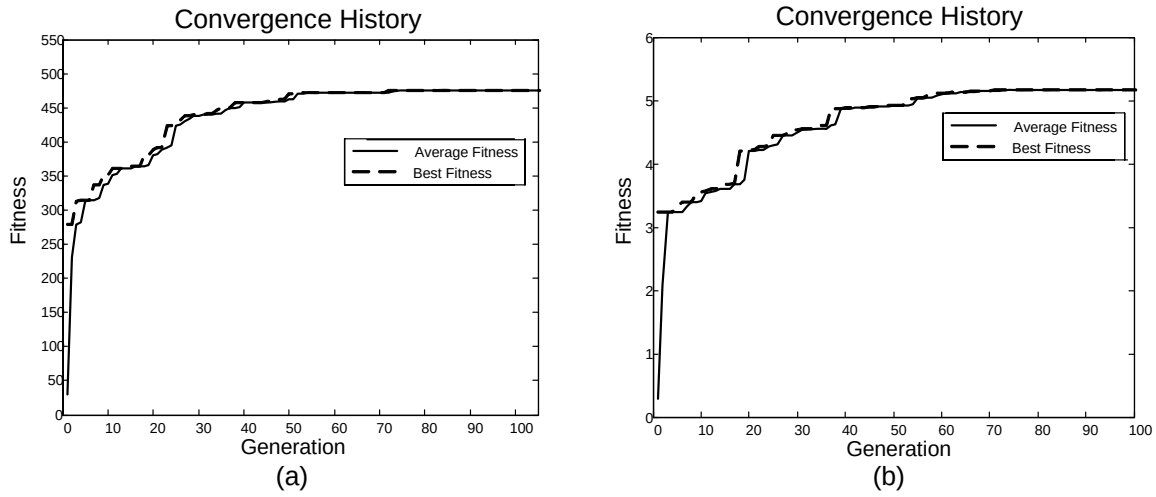

Figure 6-12: Convergence history of real-coded GA for (a) motion transfer and (b) force transfer mechanism.

Since the terminals are connected to voltage pads and to the substrate, they have the prescribed temperature as the substrate temperature. They act as heat sinks and, as a result, the local heating is lower near the terminals. Applying the buckling constraint prevents the creation of long, slender, single piece beam elements in the final solution.

A finite element analysis (FEA) of the solution was performed in order to verify the solution behavior. The result is shown in Figure 6-13, in which the undeformed shape is denoted by the solid lines and the deformed shape is denoted by the dashed lines. The displacements calculated here are for the optimal design subject to the applied voltage $V_{dc} = 0.4$ [V]. The output node number is 25 in both optimized configurations, as shown in Figure (6-13).

Comparison of the motion transfer mechanism in Figure 6-13(a) and the force transfer mechanism in 6-13(b) shows the effect of workpiece resistance on the optimized topology. As seen in these figures, the force transfer design has additional supporting elements in the arms that provide the required stiffness in the mechanism to resist the workpiece at output during actuation, in comparison with 6-13(a). The effect of workpiece resistance on optimized topology is illustrated in more detail in next example.

Figure 6-14 shows the optimized topologies for this actuator, using the same dimensions, material properties and boundary conditions presented in [10], where homogenized material

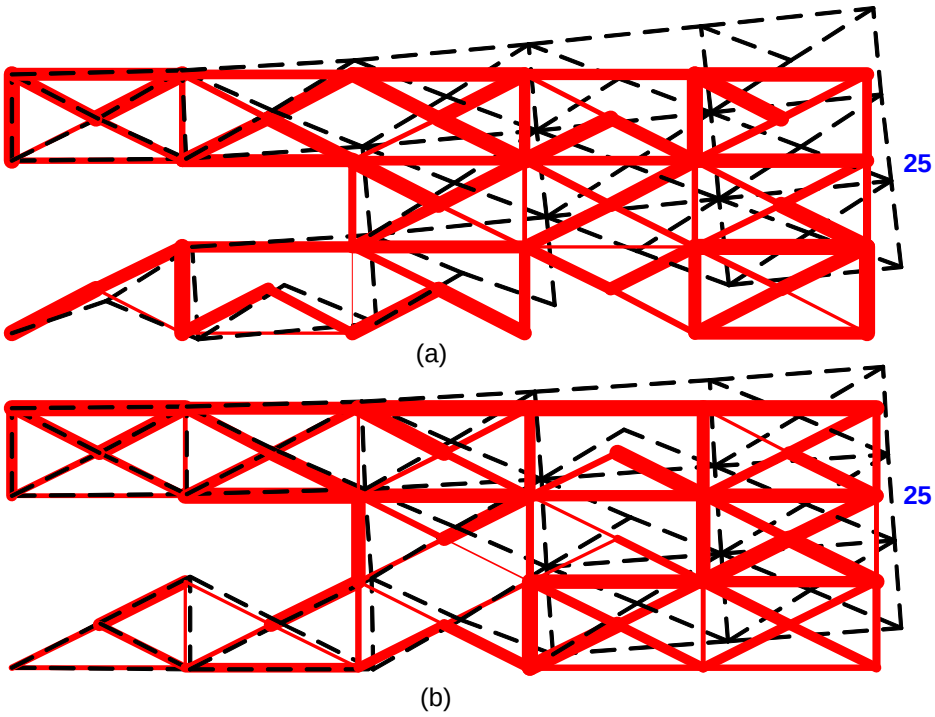

Figure 6-13: Deformed and undeformed shape of resulting optimal mechanisms for (a) motion transfer and (b) force transfer actuator where $k_s = 100$ $[\mu N/\mu m]$.

distribution was used.

Comparison of the topologies in Figures 6-13 and 6-14 highlight the following points:

- The homogenized material method results in a mechanism that relies on localized deflection at narrow flexural joints to provide the output motion; whereas, in Figure 6-13 (a) and (b), the compliance is distributed throughout the mechanism and the structure deforms as a whole.

- The mechanisms in Figure 6-13 are designed with strength consideration. The active buckling constraint ensures that all the elements are connected properly to avoid occurrence of buckling in elements during actuation. In Figure 6-14, the presence of a buckling element is observed.

- The optimized design from the homogenization method in Figure 6-14 requires manual interpolation to extract the actual layout, whereas, the design in 6-13 can be directly mapped to a feasible layout.

- Using a frame ground structures allows for a coarser subdivision of the design domain than the homogenized material method for the same resolution of the shape definition. Therefore, the frame ground structure significantly reduces the computational burden of the optimization procedure.

The optimization procedure for this example converges in less than 5 minutes on a regular PC, and after the convergence, the optimized topology is instantaneously analyzed with a built in FEA and data files are available for further study. It is also possible to conveniently extract the fabrication layout by exporting the topology to an IGES file in the GUI. The full optimization procedure from problem specification to fabrication is packaged with a GUI, which enables the efficient use of the method for users. Details of the implemented GUI are presented in Appendix A.

6.2.4 Study of Performance and Verification

To study the performance of the optimized actuator, the voltage-displacement characteristic and nodal temperature and voltage distribution of mechanisms in Figure 6-13, derived from

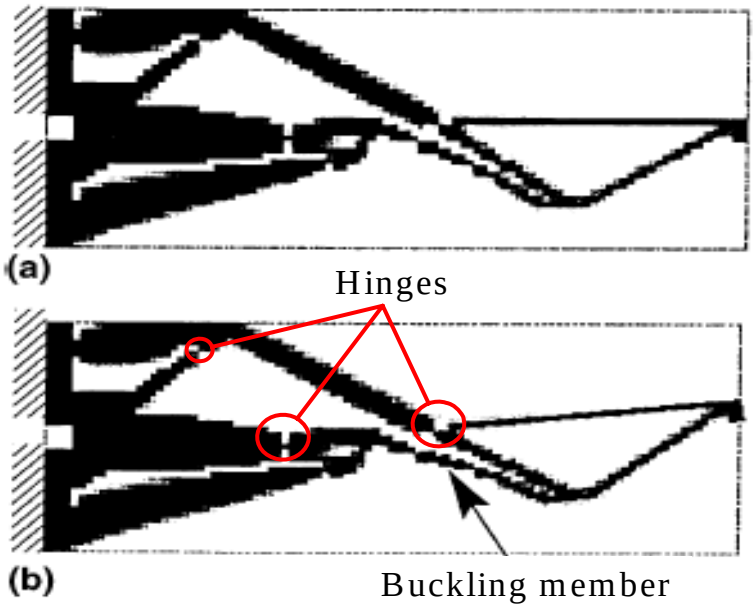

Figure 6-14: (a) Optimal actuator topology for the design problem sketched in Figure 6-9 and (b) actuated structure [10]. The design domain is discretized with 17856 elements. Deformation takes place through high stress hinges and narrow members that are prone to buckling.

the built-in FEA, are presented in the following. To further verify the results from the built-in FEA, optimized topologies are simulated in ANSYS and the results are compared with the FEA simulations. The performance of the force transfer mechanism is compared with results of same actuator optimized using the homogenization method described in the literature [33].

Figures 6-16 and 6-15 show the FEA results for nodal displacements dX and dY at $V_{dc} = 0.4$ [V] for both motion transfer and force transfer type actuators, respectively.

The output node, 25, is marked on the plots. The vertical displacements, dY, at the output node are 7.9 [μm] and 4.7 [μm] for motion transfer and force transfer, respectively. It is also noted that the horizontal deflection, dX, is 0.85 [μm] for the motion transfer and 0.41 [μm] for the force transfer mechanism. This confirms that the design specification of output direction Δ is met in both cases.

In Figures 6-18 and 6-17, the nodal voltage and temperatures of the designs are plotted from the FEA results. The voltage is distributed from 0 [V] to 0.4 [V] between the input DC terminals. The prescribed temperature value at anchors is 0 [^oC] and the maximum temperatures in the body are 543 [^oC] and 519 [^oC] for motion transfer and force transfer, respectively. It is shown here that the transferred force at output is obtained at the cost of lower displacement at the output.The optimized mechanisms are simulated in ANSYS for verification of the above FEA results. The layouts in Figures 6-11 are exported to IGES format and the solid model in ANSYS is built by importing the IGES file, meshing and applying boundary conditions. Figure 6-19 shows the ANSYS solid model of the motion transfer type actuator.

Figure 6-20(a) and Figure 6-20(b) show the displacement field contour plot of the motion transfer mechanism for dX and dY, respectively. The displacement field in ANSYS and the FEA results in Figure 6-15 agree with less than 1% error.

In Figure 6-21(a) and (b), voltage distribution and temperature distribution in the body of the actuator are plotted in ANSYS for the motion transfer mechanism. Figure 6-21(a) shows that voltage is distributed in a loop between the upper and lower arms of the actuator, from 0 [V] to 0.4 [V]. In Figure 6-21(b) the principal of actuation is shown. The formation of the cold arm in the upper region and hot arm in lower region enable the structure to deform upward in the Y direction. Also, the comparison of the temperature contour to the nodal temperature values from the FEA in Figure 6-17(b) confirms the FEA results

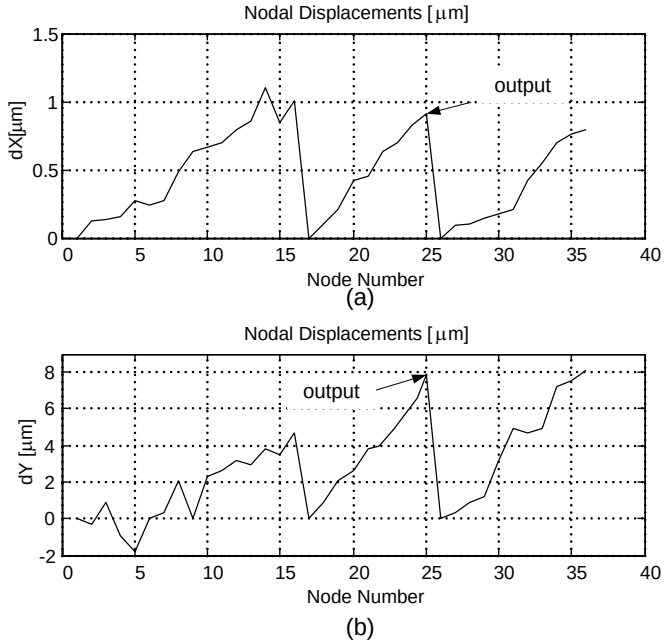

Figure 6-15: Nodal displacements of motion tansfer type actuator at 0.4 [V], plotted from FEA solver.

The voltage-displacement characteristic of both the motion transfer and force transfer mechanisms is listed in Table 6.3 and is also plotted in Figure 6-22, along with same results from ANSYS [11] simulations for comparison. The FEA and ANSYS results agree, as shown in Figure 6-22.

The performance of the force transfer mechanism in Figure 6-13(b) is compared to the one resulting from the homogenization method in [33], as shown in Figure 6-14.

In Figure 6-23, the force-displacement characteristic of the device is shown. The force transfer actuator in 6-13(b) achieves the maximum vertical deflection of 4.7 [μm] subject to 0.4 [V] applied voltage and the maximum temperature in the body is 530 [^oC]. The force exerted on the spring k_s is approximately 500 [μN] at this deflection. In [33], a vertical displacement of 7 [μm] and output force of 700 [μN] is reported for the mechanism in Figure 6-14.

It is concluded that the optimized force transfer actuator in Figure 6-13(b) can closely meet the performance of its counterpart with a reliable well posed configuration.

It should be noted that a compliant mechanism gains its mobility from flexibility of its

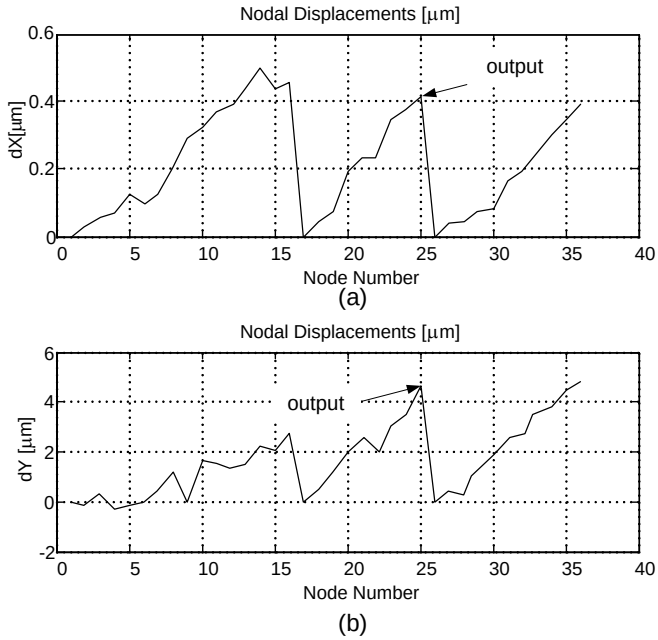

Figure 6-16: Nodal displacements of force tansfer type actuator at 0.4 [V], plotted from FEA solver.

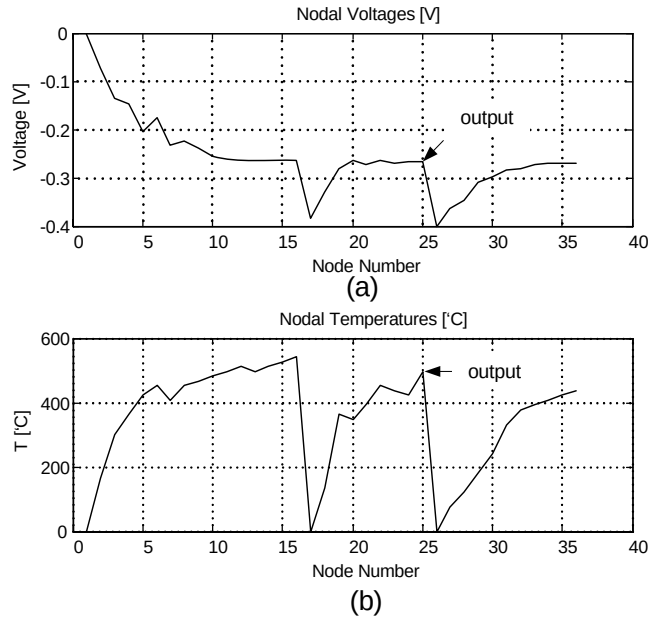

Figure 6-17: (a) Nodal voltage values and (b) nodal temperature values of the motion transfer type mechanism in Figure 6-13(a), plotted from the FEA results.

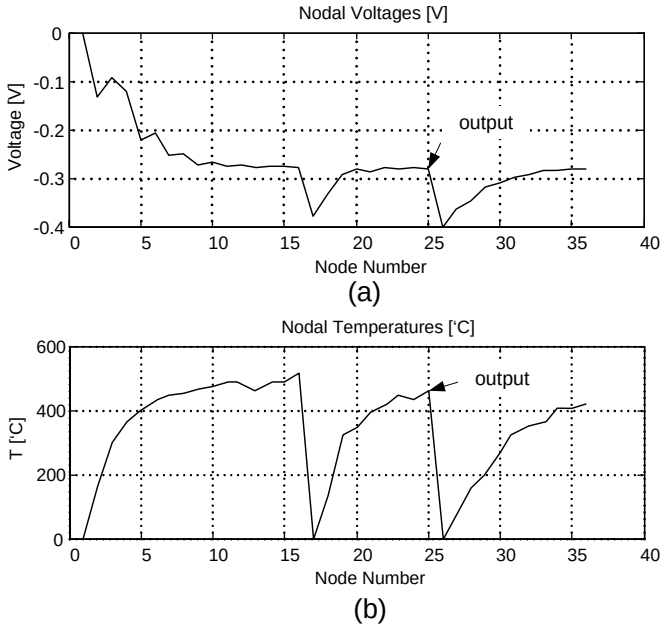

Figure 6-18: (a) Nodal voltage values and (b) nodal temperature values for the force transfer type mechanism in Figure 6-13(b), plotted from the FEA results.

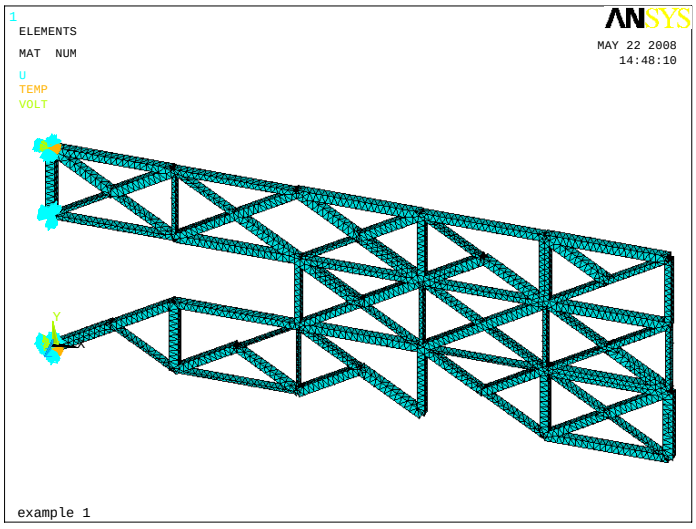

Figure 6-19: ANSYS [11] model of the motion trasfer mechanism, showing the mesh and boundary conditions applied.

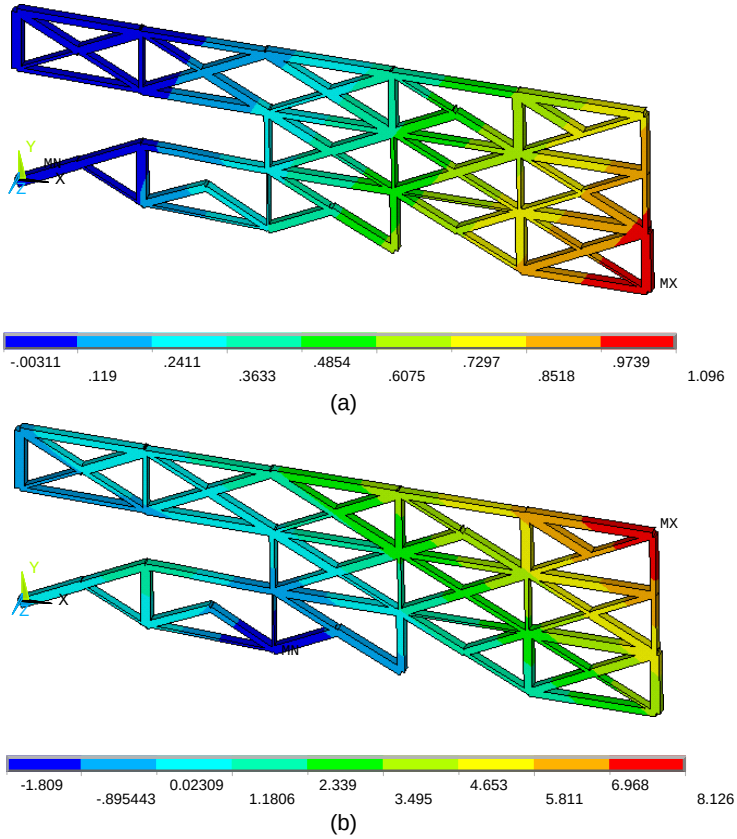

Figure 6-20: ANSYS [11] simulation results for the motion transfer actuator (a) dX and (b) dY. The simulations verify the nodal displacements plotted in Figure 6-15.

Table 6.3: Value of vertical displacement at output point from the optimization package for the motion transfer and the force transfer actuators

$dY[\mu m]$		
Voltage [V]	Motion Transfer	Force Transfer
0.1	0.7	0.3
0.2	2.01	1.1
0.3	4.5	2.7
0.4	7.9	4.7
0.5	12.2	7.5
0.6	17.2	10.5
0.7	23.1	13.9

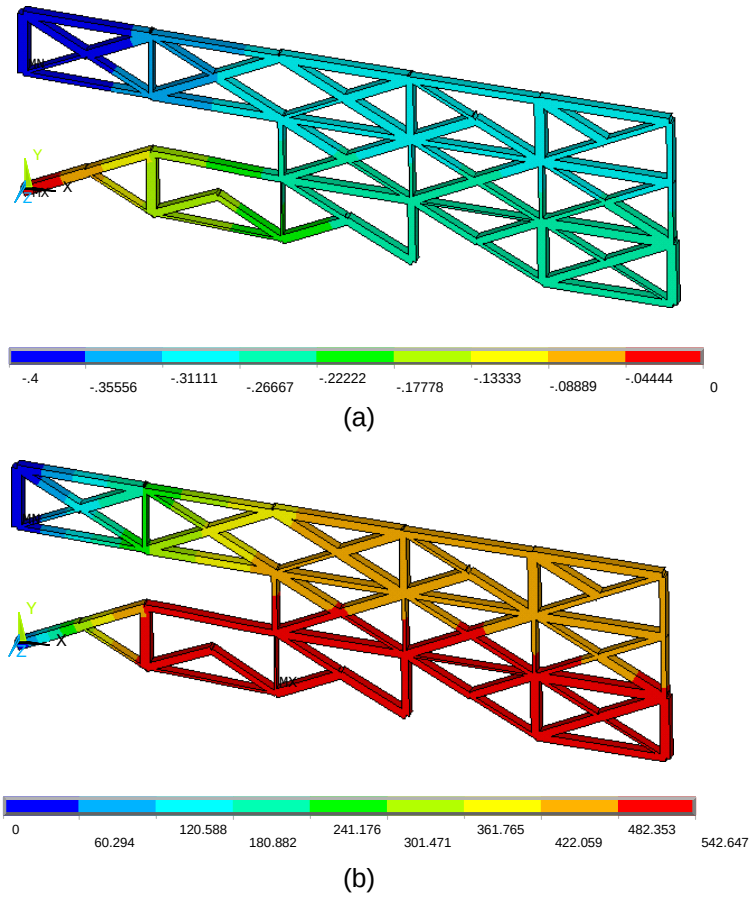

Figure 6-21: ANSYS [11] simulation results for motion transfer actuator (a) voltage distribution and (b) temperature distribution. The simulations verify the nodal voltage and displacements plotted in Figure 6-20.

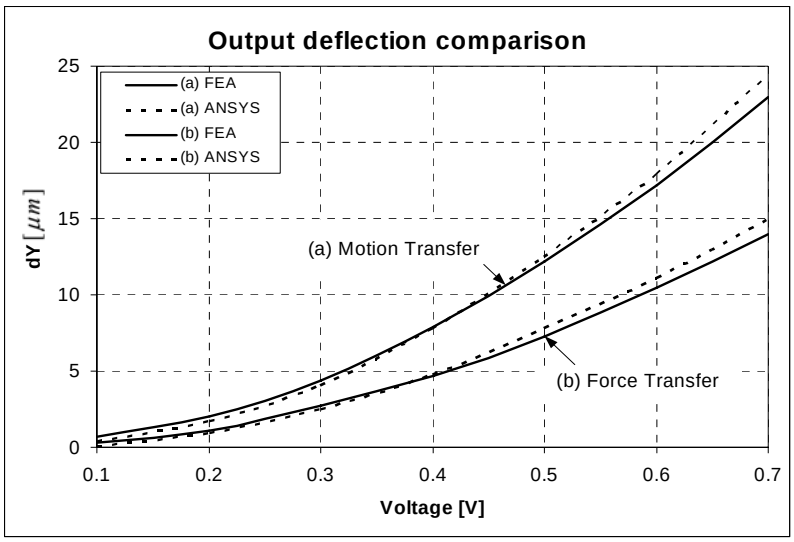

Figure 6-22: Comparison of vertical displacement, $dY[\mu m]$ at the output point from the optimization package and ANSYS [11] for both motion transfer and force transfer type actuators.

members. A compliant mechanism will always perform worse than its rigid-body counterparts since some of the input energy will be stored as elastic energy in its members. This fact also justifies the difference in performance between the frame based mechanism and the homogenized material result. As mentioned previously, the mechanism resulting from the homogenized material method gains its mobility through solid blocks of material connected together with narrow hinges and is categorized as a lumped compliance mechanism. In contrast, the frame structure mechanism bends as a whole to transfer the force and motion and is categorized as a fully distributed compliant mechanism. It is then expected that a fully distributed compliant mechanism has a lower performance than its lumped compliant counterpart. However, the difference in performance is off-set by the robustness, reliability and manufacturability of the fully compliant mechanisms.

A comprehensive study of the optimized topologies and comparison with their counterparts from the homogenized material method highlights the following conclusions for this example:

- The design domain was discretized with 17854 elements to achieve the optimized topology in Figure 6-14 [33]. The initial frame ground structure in Figure 6-10 consists of 37 nodes and 88 elements. The significant decrease in number of elements results in a low

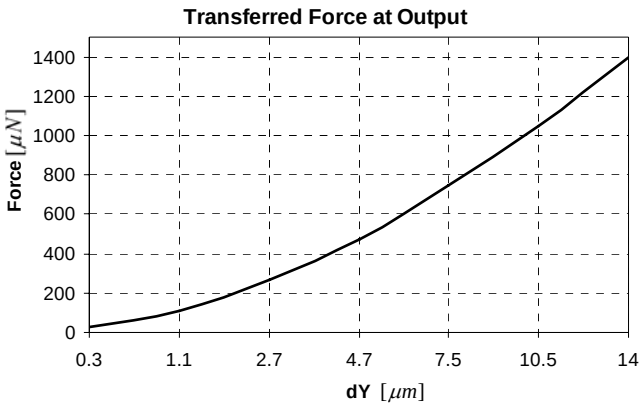

Figure 6-23: Force- displacement characteristic of the force transfer type mechanism in Figure 6-13(b).

computational cost.

- The simulation results from ANSYS [11] verify the accuracy of the optimization package and its finite element solver. They prove that this package is reliable to be used as a powerful tool to provide designers with novel ideas to design electro-thermo-mechanical components for MEMS.

6.3 Example 3: High Force Actuator

In this example, the effect of workpiece resistance on the final optimal topology is studied in detail and the optimum topologies are compared with a conventional actuator [12] and results from the homogenization method described in the literature [13].

6.3.1 Design Domain

Figure 6-24(a) shows the schematic of problem specification in example 3. In this example, the effect of workpiece resistance, k_s, on optimized actuator configuration is studied. In Table 6.4, the design domain dimensions and input specifications are listed.

The material properties are that of Polysilicon, which are listed in Table 4.1. A voltage of 10 [V] is applied across input DC terminals, which are also the locations where the domain

Table 6.4: Geometrical dimensions for the high force compliant actuator in Example 3.

Geometrical Data		
Design domain dimensions	200×500	μm
Void domain dimensions	67×84	μm
V_{dc}	10	V
Thickness	2	μm
air gap to substrate δ	2	μm
T_s, T_∞	0	$^\circ C$

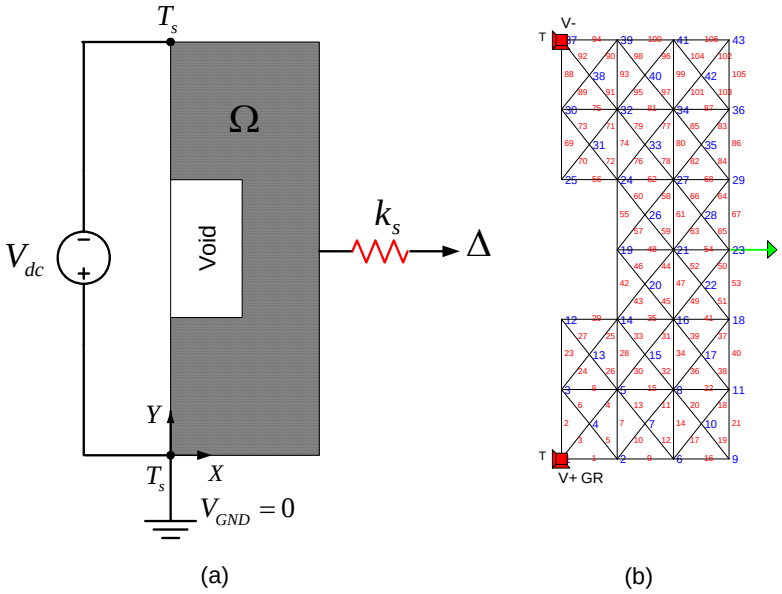

Figure 6-24: (a) Design domain for Example 3 and (b) initial frame structure with applied boundary conditions.

is mechanically fixed to the ground. The optimized actuator should have maximum deflection in output direction, Δ, at prescribed location, subject to applied voltage and thermal and mechanical boundary conditions at anchors. Output direction Δ is defined with the vector [1,0], denoting that, at target output location, the actuator moves only in X direction and should have no vertical movement, where X and Y are the coordinates of the $2D$ space, as shown in Figure 6-24(a).

Figure 6-24(b) shows the initial frame ground structure with the applied boundary conditions and output specification. The initial ground structure is discretized with 43 nodes and 106 elements.

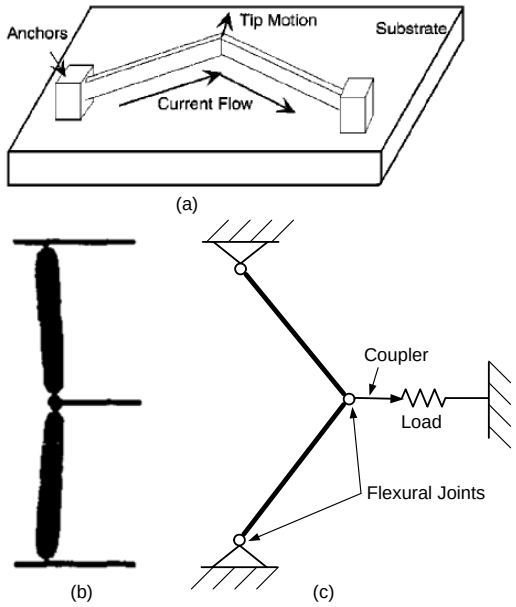

Figure 6-25: (a) Intuitive design for Example 3 [12] (b) optimized topology with homogenization method [13] and (c) equivalent rigid link mechanism.

Figure 6-25(a) shows the intuitive bent beam actuator reported in the literature [12].

In Figure 6-25(b) the result of the homogenized material method described in the literature for the same domain is shown [13]. Figure 6-25(c) shows the kinematic equivalent configuration of this design. It is shown in [14] that the continuum-based design in Figure 6-25(b) results in a very low yield in fabrication due to very narrow hinges, which are below the lithography reliability limit. This mechanism consists of rigid links connected together through flexural hinges to achieve the flexibility. In [14] fabrication yield of this device is reported to be less than 10% due to residual stress build up at narrow thin parts, as shown in Figure 6-26. From the failure analysis in [14] it is concluded that design optimization targeted only at performance hardly produces actuators at a high yield rate. In [14] it is stated " if a design optimization method can consider MEMS design issues such as stresses, the actuator failure rate can be substantially reduced. However, to our knowledge, no such method is yet available, so far." It will be shown in the following that frame ground structure with active buckling constraint can result in topologies compatible with microfabrication processes and as a result they can

potentially have a high yield rate.

6.3.2 Problem Statement

The design specifications are that an applied voltage, V_{dc}, causes the motion, Δ, in the horizontal direction. The multi-criteria objective function in Equation (5.12a) was employed where $m = 3$ and $n = 2$ and the buckling constraint is active. The exponents of objective function are chosen to provide a balance between high force and deflection. The optimized topology should transfer the maximum force and deflection at the output location in direction of Δ, while the workpiece resistance, k_s, is increased at the output point. The optimization problem is then formulated as:

$$
\begin{gathered}
Maximize : sign(MSE)^2(\frac{MSE^3}{SE^2}) \\
Subject\ to : 1 < w_e < 5\ [\mu m] \\
F_e < \bar{P} \\
k_s = 0,\ 100,\ 500,\ 1000\ [\mu N/\mu m] \\
\text{electrical equilibrium equations} \\
\text{thermal equilibrium equations} \\
\text{elastic equilibrium equations} \\
\text{flexibility requirement} \\
\text{stiffness requirement} \\
\text{Convergence criteria =1e-6} \\
\Delta \text{ in the direction of [1,0]}
\end{gathered}
\tag{6.3}
$$

where w_e is the in-plane width of element e and is the design variable for the optimization algorithm and $\bar{P}$ is the maximum allowed force before buckling from Equation (5.15).

6.3.3 Optimized Configuration

In Figure 6-27 the optimized topology is shown with solid lines and the deformed shape of the mechanism at 10 [V] is superimposed with dashed lines, for listed values of k_s. The displacement

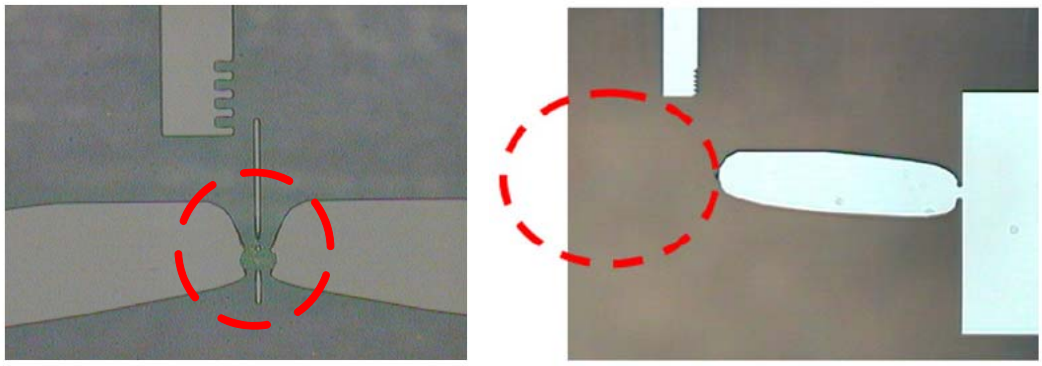

Figure 6-26: Failure of a optimized thermal actuator in Figure 6-25(b) due to stress concentration in narrow hinges and violating minimum length scale [14].

field in this figure is scaled for better presentation and is, therefore, not to scale with the figure. As shown in Figure 6-27, for $k_s = 0$ $[\mu N/\mu m]$, optimum design tends to the configuration of the intuitive design shown in Figure 6-25(a); however, the active buckling constraint prevents formation of long and slender elements. The actuator main body is a V shape element in the middle, supported by connecting elements to satisfy the strength consideration. As shown in this figure, the optimized topology becomes stiffer by increasing the workpiece resistance. The required stiffness for sustaining the external resistance is automatically provided by adding supporting elements to the main V shape actuator.

It is observed that the optimization scheme is capable of satisfying the symmetry nature of the design domain without imposing a symmetry condition on the formulation. It is also noted that the direction of the output deflection is fully satisfied and the optimized designs have almost zero vertical displacement at output. These observations confirm that topology optimization is well-posed to satisfy the full set of design specifications.

6.3.4 Study of performance

The performance of the optimized structures in Figure 6-27 are studied here. Figure 6-28 shows the plot of tip displacement, dX $[\mu m]$, versus applied voltage [V]. This plots shows that the actuator displacement decreases with increased workpiece resistance. In the neighborhood of the specified input voltage of 10 [V], the displacement of the actuator is linear. This linear

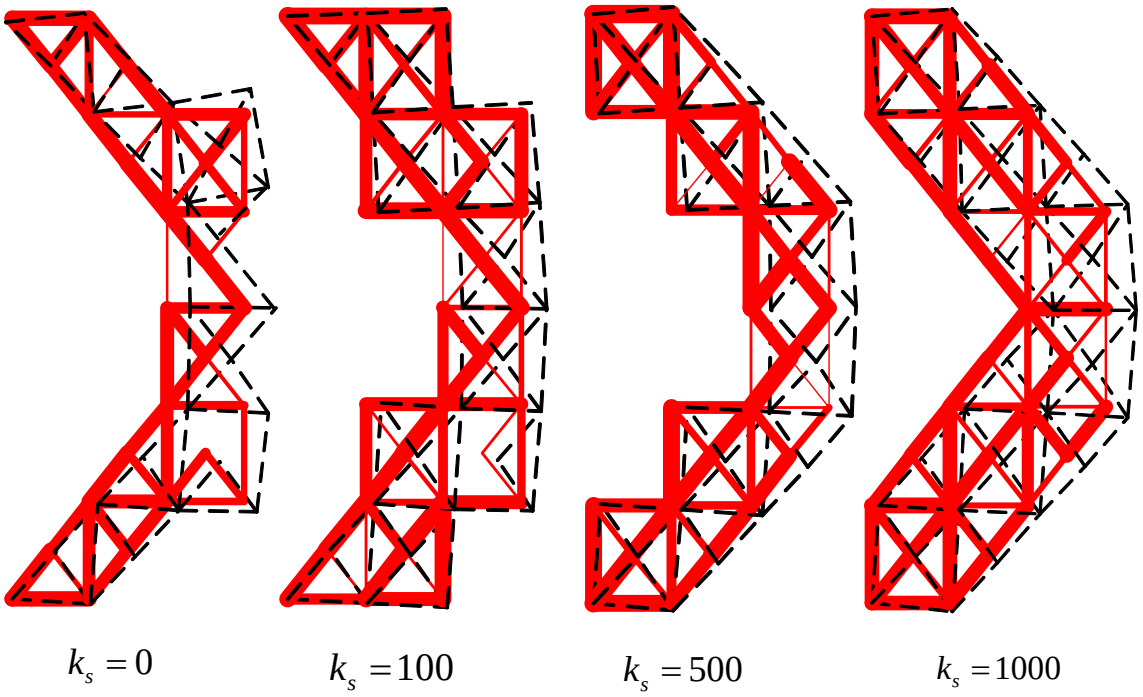

Figure 6-27: Optimized configuration of Example 3 for an increasing value of workpiece resistance k_s.

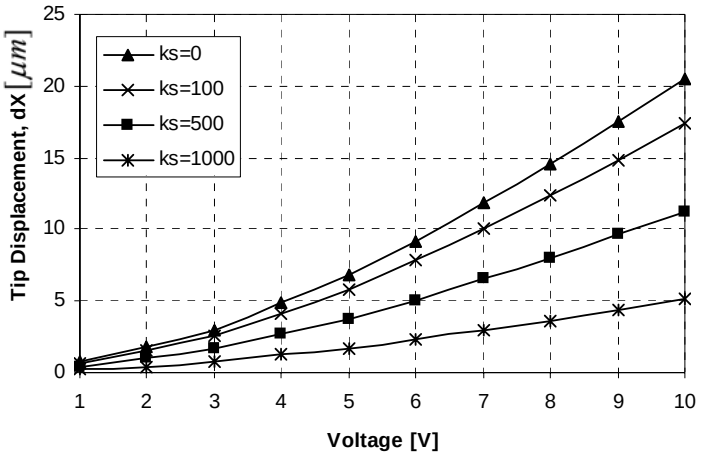

Figure 6-28: Tip displacement versus applied voltage of optimized configurations with varying k_s, shown in Figure 6-27.

displacement behavior is also seen in intuitive designs found in the literature [12].

For high values of k_s, the actuator has thicker arms supported with more elements, whereas for low values of k_s, the optimal topology shows thin members and a reduced number of supporting elements around the main V shape arm. In Figure 6-29, the force-displacement characteristics of the actuators are plotted for k_s = 100, 500 and 1000 [$\mu N/\mu m$] and it is shown that the optimized actuator have a linear force-displacement characteristic. However, it is observed that the large output forces with an increasing value of k_s are obtained at the cost of low deflection at output.

The intuitive design for this domain is shown in Figure 6-25(a). This type of bent beam actuator, also known as TIM, was studied in Chapter 4, Section 4.6.2. Figure 4-13 shows that the output displacement of the actuator decreases as the pre bend angle α_b increases. For the conventional TIM, the pre bend angle is usually very small, on the order of a fraction of a degree. However, the pre bend angle α_b in the optimized topology in Figure 6-27 is 38.66 degree. In Figure 6-30 performance of the TIM with same dimensions and material properties as example 3 is compared with optimized topology in Figure 6-27 for the case $k_s = 0$. The actuator in Figure 6-30(b) consist of 320 [μm] half beams with cross sectional area of 5 [μm] in width and by 2 [μm] in thickness connected with a 5 [μm] by 2 [μm] connector. The actuator is

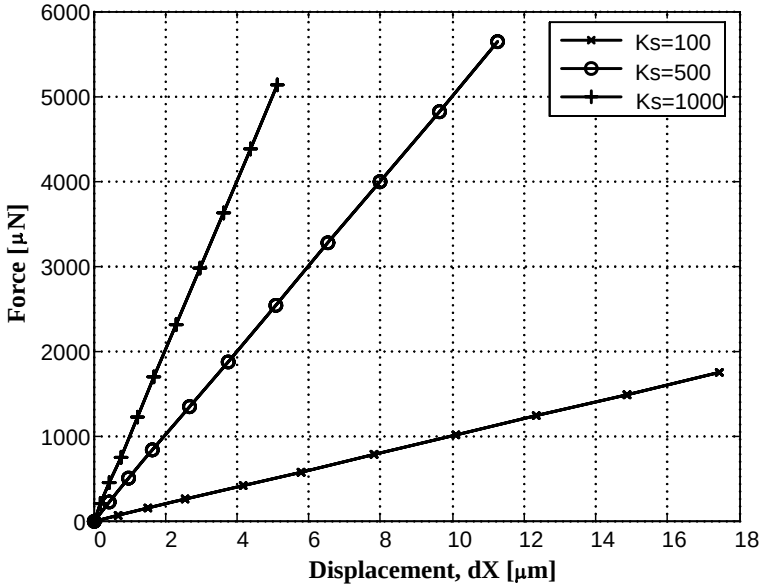

Figure 6-29: Force-displacement characteristic of optimized actuators of Example 3 for $k_s = 100$, 500 and 1000 $[\mu N/\mu m]$.

simulated with FEA package developed in Chapter 4 at 10 [V] applied voltage. It is seen in the deflected form of the actuator that TIM is not a feasible design for this domain. At pre bend angel of $\alpha_b = 38.66$ deg. the beam buckle in plane and the output displacement is less than 1.5 $[\mu m]$. The deformed shape pattern is magnified 15 times in Figure 6-30(b) for visibility. On the other hand, the topology optimization is capable of optimizing the design for any pre bend angel and best performance. To transfer high forces, bent beam actuators are placed in an array of connected actuators as shown in Figure 4-11 but topology optimization can produce a design that can transfer high forces at the output in one actuator. This comparison also applies to Example 1, where $\alpha_b = 75.96$ deg. The result confirms that topology optimization can be used to generate non-intuitive optimized designs.

6.4 Conclusions

The novel topology optimization scheme from Chapter 5 was applied to the design of compliant electro-thermal micro-actuators. The performance values of the optimized electro-thermal ac-

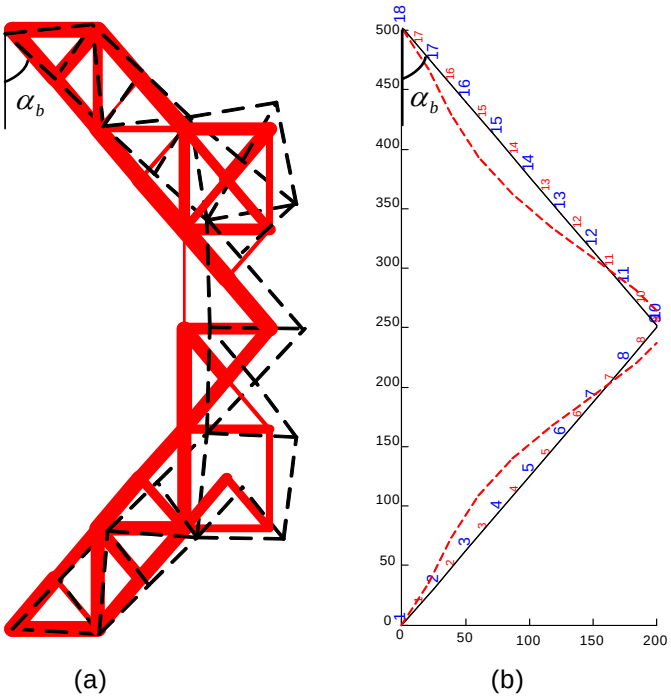

Figure 6-30: (a) optimized actuator for $k_s = 0$ with pre-bend angel of $\alpha_b = 38.66$ deg. and (b) The conventional actuator with same material and dimensions, simulated with FEA at 10 [V].

tuators were studied and compared with the performance of the finite element model in ANSYS [11], the resulting topologies from the homogenization method and intuitive actuators described in the literature.

The comparisons verify that, for MEMS applications, the frame ground structure is more suitable. The developed genetic algorithm effectively overcomes the previous convergence difficulties. The proposed objective function implemented with the real-coded genetic algorithm shows distinct advantages over other methods, such as:

- The new formulation provides the option to design the compliant mechanisms for specified motion or force transfer.

- The resulting design is a frame-like structure, which is feasible to fabricate in MEMS. There are no hinges, checkerboards or gray material regions, which do occur in the homogenization method. The use of beam elements tends to yield solutions without flexural pivots because the elements bend as a whole. Therefore, qualitatively speaking, the resulting designs tend to have distributed compliance rather than lumped compliance.

- The real-coded genetic algorithm shows a better repeatability. It converges to very similar solutions in different runs, as compared with SLP or SQP, in which the solutions are strongly dependent on an initial guess.

- The ground structure domain discretization, in conjunction with an efficient genetic algorithm, facilitated the use of a coarse mesh, which resulted in a low computational cost. The presented approach therefore provides a computationally efficient alternative to the continuum-element-based approach for the topology optimization of ETC mechanisms.

- The built-in FEA code is verified as an efficient and reliable tool for analysis of compliant designs.

Chapter 7

Conclusions

7.1 Summary of Contributions

Micro-compliant devices, which are predominantly utilized at micro-scale as force and motion transmitters are at the core of microsystems. This research deals with topology optimization of micro-compliant devices. The main application is in designing optimum MEMS compliant actuators with embedded actuation. Since electro-thermal actuation is very common in MEMS, the focus of this thesis is on the development of an optimization scheme for multi-disciplinary domains, especially an electro-thermo-mechanical domain.

An optimization algorithm for the design of compliant mechanisms with electro-thermo mechanical boundaries was developed. Several examples were used to validate and compare the results with previous research in this field. Improvements in optimum solutions are highlighted below:

- A new fully coupled analysis method for electro-thermo-mechanical domain was developed. A new algorithm was proposed to couple the resistive circuit method to finite element analysis (FEA) by Modified Nodal Analysis (MNA). This formulation provides a fast and reliable tool to analyze electro-thermo-elastic devices, which allows for large flexibility in the selection of mechanical, thermal and electrical boundary conditions.

- A novel topology optimization scheme for MEMS compliant electro-thermo-mechanical devices was developed. The superiority of the new optimization method was illustrated

with examples of novel electro-thermal actuators.

- Embedded electro-thermal actuation was implemented in the topology optimization scheme.
- Multiple inputs were enabled through the new formulations, which allows for topology optimization with an unlimited number of electrical, thermal and mechanical boundary conditions for the domain.
- A new multi-criteria objective function was proposed for electro-thermal and thermal domain optimization to balance flexibility and stiffness requirements. The new formula also enables optimization of the domain for force transfer or motion transfer compliant mechanisms.
- Practical solutions for several identified issues in topology optimization of MEMS devices were proposed and implemented:
  - An efficient real-coded genetic algorithm (GA) with elitism was implemented for the optimization procedure, which significantly improves the computation cost, convergence and repeatability of the optimization problem. The ground structure domain discretization, in conjunction with implemented genetic algorithm, facilitated the use of a coarse mesh, which results in a low computational cost. The presented approach therefore provides a computationally efficient alternative to the continuum-element-based approach for the topology optimization of electro-thermo-mechanical mechanisms.
  - A new element removal policy was implemented to include MEMS fabrication limits and tolerances in the optimization procedure.
  - The strength and reliability of the optimized designs were addressed by imposing a new buckling constraint on elements of optimization.
  - It was confirmed through examples that the frame ground structure produces optimal designs that can be directly mapped for fabrication and need no further interpretation, post processing or gray zone filtering, as required in previous research based on the homogenization method.

  - It was shown that frame ground structure discretization allows the use of a coarse subdivision of the design domain than the continuum-element approach for the same resolution of shape definition. Therefore, in conjunction with genetic algorithm, the frame-element-based formulation reduces the computational burden for the optimization procedure without compromising the sharpness of the shape definition. The presented approach therefore provides a computationally efficient alternative to the homogenized material approach.
  - The issue of producing optimal designs with fully distributed compliance versus lumped compliance was addressed by employing a new frame ground structure for domain discretization and imposing a strength constraint through a buckling limit.

- The topology optimization scheme developed in this thesis is made available for MEMS designers and other researchers with a graphical user interface (GUI).

7.2 Future Research

The new topology optimization method implemented in this thesis provides a flexible ground for expansion and future research. The following directions for future research are recommended:

- It can be used as the basis for design of compliant mechanisms for optimum dynamic responses. The potential applications of optimum dynamic compliant systems are numerous, including the design of resonators and filters for optimum tunability and low power consumption.

- The systematic approach to topology optimization of MEMS presented in this thesis provides a basis for designing compliant MEMS with multiple materials. The discretization scheme with frame ground structure used in this thesis, is specially suited to incorporate multiple materials, since each element of the frame can possess different material properties.

- The focus of the topology optimization scheme presented in this thesis was on electrothermal actuation, as the most common actuation scheme used in MEMS community. However, this optimization package can be extended to include other actuation schemes

(e.g. piezoelectric actuation) using fully coupled resistive circuit and finite element method.

- In this research, the problem of multiple inputs was addressed with a new proposed coupled analysis method; however, the optimization scheme can be expanded to optimized compliant mechanisms with two-phase and multiple outputs.

- The method developed in this thesis for two dimensional in-plane domains can easily be extended to 3D domains with expansion of matrix equations to 3D frame structure.

- In the finite element formulation of thermo-elastic field the assumption of linear small deformations was followed. Although the frame structure may undergo large deformations, individual beams in the frame structure stay in the small deformations regime. The formulation however, can be exteded to include the second order bending terms in the stress-strain equation of the beam to consider the effect of geometric stiffness at large deformations.

- In this thesis, genetic algorithm was employed to improve the convergence of the optimization problem. More improvement in the convergence is possible using multiple objective functions with Pareto optimization to find the optimal compromised solution in the Pareto set.

Appendix A

Designing GUI for Topology Optimization Scheme

In this appendix, a software with graphical user interface (GUI) that provides an automated design route from problem specification to fabrication of fully compliant electro-thermal mechanisms is presented in detail.

The new formulation for multi-criteria objective function with genetic algorithm (GA), proposed in Chapter 5, is employed as the optimization algorithm. The topology optimization GUI described herein is the extended version of the GUI developed for the mechanical domain and the FEA package described in Chapters 3 and 4. The design continuum is presented using ground structures of frame finite elements. As noted in the thesis, these elements are easy and robust in implementation and help provide effortless extraction and transfer of optimal topologies into commercial CAD packages.

An edge detection algorithm is also used with the GUI for boundary extraction of optimal compliant geometries. The resulting data is stored in IGES format for easy portability into commercial modelling and analysis software packages for further investigation. Because the focus of this research is on micro-compliant mechanisms, the program is designed to use the $\mu m - kg - s$ system of units. In this case, dimensions are in $[\mu m]$, forces are in $[\mu N]$, and pressure is in $[MPa]$.

From the findings of this research, it is clear that compliant mechanisms have numerous

advantages in product design especially for newer technologies, such as MEMS. Despite the advances in developing design techniques in the recent past, the broader research community and the commercial arena have not yet utilized them in synthesizing compliant mechanisms. This can be attributed to the lack of access to the synthesis codes developed by various researches. Recently, TOPOPT was made available by Sigmund [96]. TOPOPT is a synthesis software that utilizes SIMP models [97] for topology optimization of compliant mechanisms, yet it neither addresses the MEMS domain nor the coupled field domain design (e.g. electro-thermal). It is limited to a single field of mechanical design and uses the homogenized material topology optimization scheme, which fails to provide designs compatible with MEMS fabrication requirements.

The synthesis software explained here is developed to make the program implementation available to MEMS designers at large. There is an added benefit when this software is used by device designers who are not necessarily familiar with the details of topology optimization techniques. When designers use it in situations not foreseen while developing the software, its generality is challenged providing valuable feedback for further improvement. The base software is a graphical user interface (GUI) implemented in Matlab [75] for the synthesis of optimal compliant topologies. The software provides an interactive and automated design route to synthesis of micro-electro-thermal compliant mechanisms from function specifications to fabrication.

In Figure A-1, the two main menus of the GUI are shown, including the display menu and parent menu, also referred to as the top level design menu. The graphical representation of design domain and results of optimization are presented in the display menu, while the parent menu contains inputs and controls for the optimization scheme.

The top level design menu is shown in Figure A-2. The user interface of this menu is divided into four sections, as follows:

Function specifications where decisions on the geometry and discretization of the design domain are made, and input and output ports with electrical and thermal loading, displacement boundary conditions and output specifications are specified. **Data processing** in which mesh information is made available to the optimization algorithm, specifically, real-coded genetic algorithm via the **Optimization** module. Finally, the **Fabrication** module allows interactive

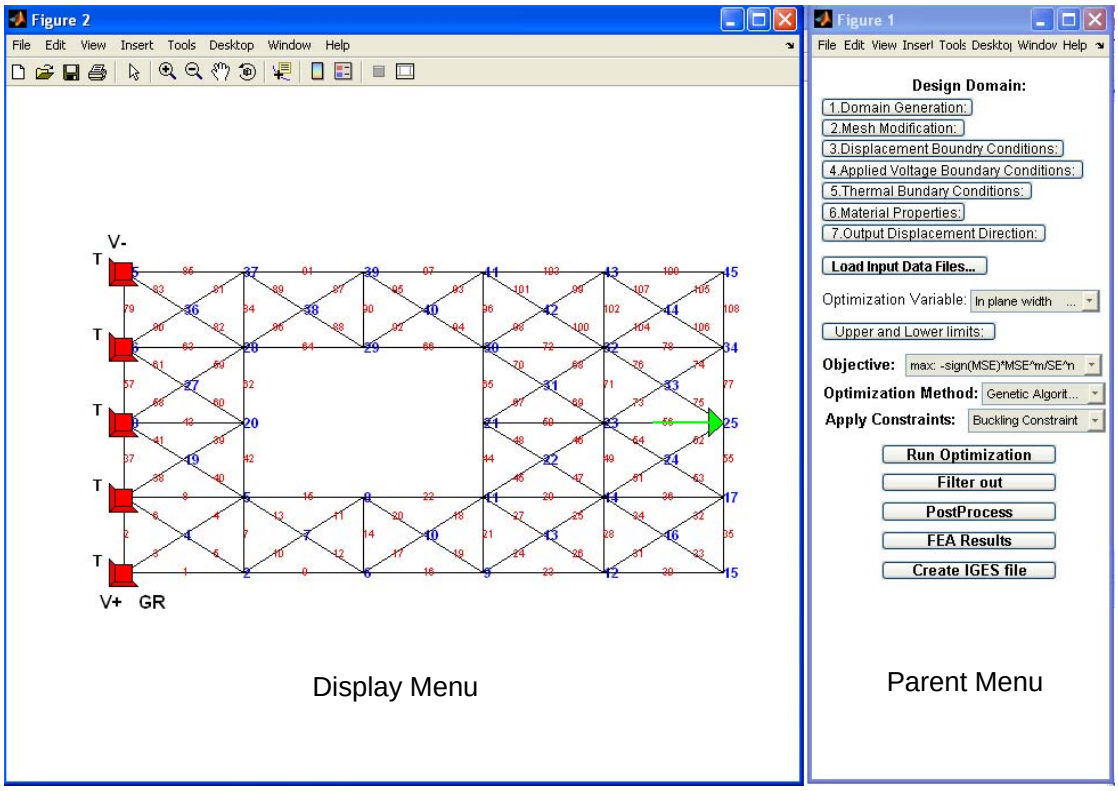

Figure A-1: Two main menus of the GUI, display menu and parent menu.

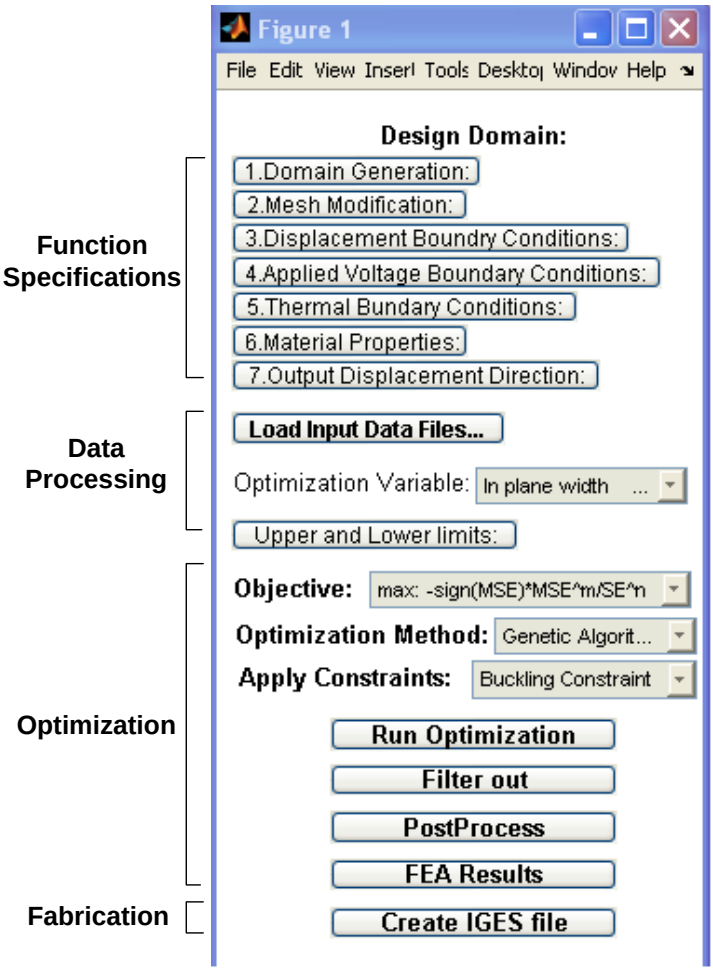

Figure A-2: Parent design menu for the GUI software.

modification of the optimal solutions and helps in creating a CAD interface to transfer the optimal continuum geometry to existing commercial software such as ANSYS [11].

A.1 Designing Compliant MEMS With GUI

The software uses frame element mesh to represent a design region. The optimal geometries are well defined when using these element types, as apposed to implementation with homogenized material elements, in which serrated edges or regions with only a node shared by two elements may be obtained, which are difficult to interpret in a CAD package. With relatively fewer degrees of freedom required to model a design domain, synthesis with frame elements is more robust and results in designs that are feasible for manufacturing, as previously discussed in this thesis.

A.1.1 Function Specification

Figure A-3 shows the details of Function Specifications module. The initial design domain is assumed to be rectangular. The dimensions, specifically, the region's length and width, can be specified using the *Domain Generation* icon in the Function Specifications module but can be modified to any shape, as explained below with *Design Domain Modification*. A full ground structure is ideal for discrete representation of the design region, i.e. nodes are placed at regular intervals in the region, and comprises an array of unit cells, as shown in Figure A-3. Two meshing policies are implemented that allow for control over meshing quality with coarse or fine mesh options. The number of cells along the domain length and width can be specified with the pop-up menu (Figure A-3) that appears when choosing *Domain Generation* option. In Figure A-3, node numbers are annotated with a large font size, while element numbers are shown using a smaller size.

With the *Design Domain Modification* option (Figure A-3), software allows interactive removal of elements from the domain boundary or its interior to define the proper domain shape or specify the void area. The user can select such elements using the left button of the mouse near their mid-points. Selected elements show red in the prompt window, while deselected elements are shown in black. Elements can be deselected using the left mouse button again.

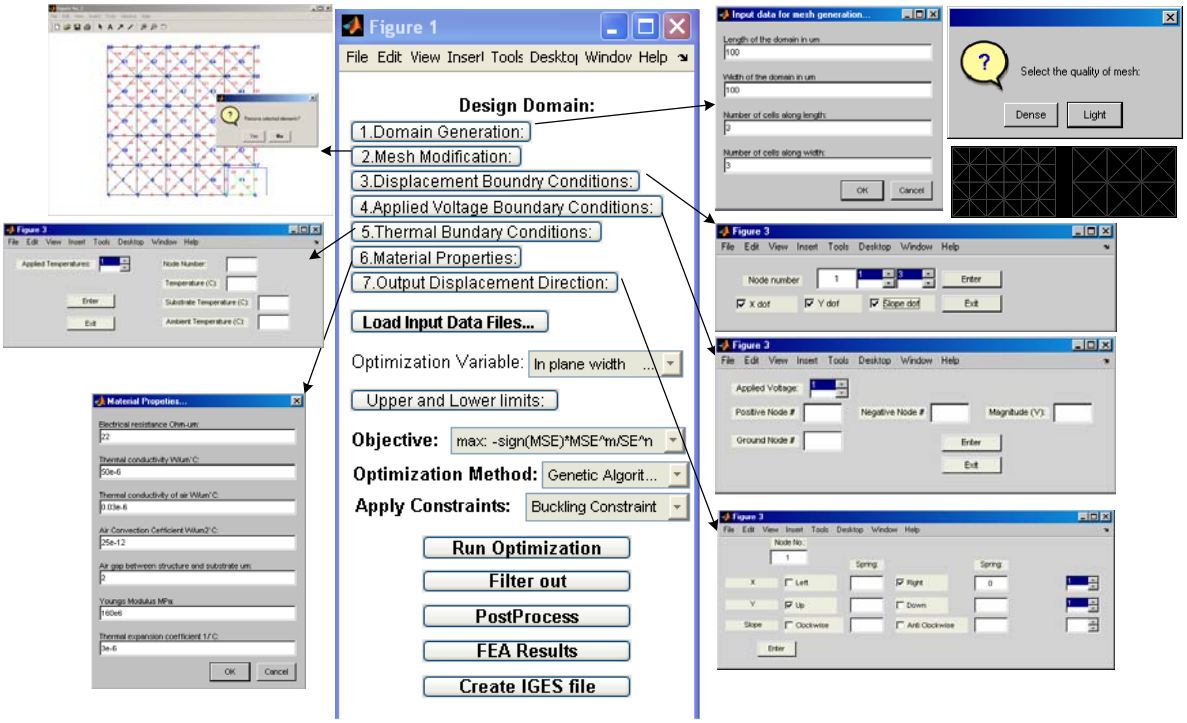

Figure A-3: Function Specification pop-up menus.

The user can register his/her decision by using the right mouse button on the last element to be deleted. Domain geometry can also be modified by selecting a group of elements within a rectangular region. The prompt window is updated and a query on further domain modification is issued. If region modification is not required, this option can be ignored.

The displacement boundary conditions are entered using the *Displacement Boundary Conditions* icon in Figure A-3. For frame elements, three check boxes corresponding to x, y and slope degrees of freedom are depicted. The user is required to enter the node number and check the *dofs* which he/she wants fixed. The list box in the middle shows the number of nodal entries made and the box to its right depicts the total number of degrees of freedom checked. The information is not registered unless *Enter* icon is used. When finished specifying the fixed *dofs*, the *Exit* icon is used.

The electrical boundary conditions are applied using *Applied Voltage Boundary Conditions* icon. The magnitude of the applied DC voltage, the node numbers corresponding to positive and negative DC source connections, and the reference ground node for the voltage source are entered. The list box on the top left shows the total number of DC sources specified for the domain. There is no limit on the number of DC sources connected to one domain. The user is required to hit *Enter* after entering the parameters for each source. When finished, the *Exit* icon is used.

The thermal boundary conditions are applied through the *Thermal Boundary Conditions* window. The temperature imposed on a specific node and corresponding node number are entered in the top right boxes in degrees Celsius. The substrate temperature and ambient temperature are entered in the two bottom boxes in the right. There is no limit on the number of nodal thermal boundary conditions imposed on domain but substrate and ambient temperature are entered once and remain constant for the total domain. The total number of temperature boundaries applied is shown in the top left box and the user needs to hit *Enter* after entering each set. When finished, the *Exit* icon is used.

The output port is specified using the *Output Displacement Direction* icon in Figure A-3. The node number is entered in the top left edit box in the pop up menu and the direction corresponding to x, y and slope *dofs* are checked. Appropriate linear spring constants, k_s , across the checked directions may be provided. They not only help in modelling the reaction

forces but also control the output direction of deformation indirectly. Edit boxes on the extreme right depict unit dummy loads along the direction checked for the MSE and SE calculation. For direct control, these values can be changed in the data files inside program functions. Positive signs, by convention, signify right and upward directions along the horizontal and vertical axes, respectively. When finished, the *Exit* icon is used.

A.1.2 Data Processing

The input requirements generated using the *Function Specifications* module, or generated elsewhere, can be made available to the optimization algorithms using the *Load Input Data Files* icon in Figure A-4. At *Load Input Data Files*, seven data files are generated with the input information, as follows:

- The *node.dat* file contains node numbers in the first column and x and y coordinates in the second and third columns, respectively.
- Element numbers appear in the first column of the *elem.dat* file. The node connectivity information, or the nodes to which elements are connected, appear across appropriate element numbers in the second and third columns, respectively, in *elem.dat* file. Material properties associated with each element are also stored in *elem.dat,* columns 5 to 8 for Young's modulus, electrical resistivity, thermal conductivity and thermal expansion coefficient, respectively.
- In data file *dispbc.dat,* mechanical boundary conditions associated with each node are arranged in columns. The first column is the count, the second column is the node number and the third column carries the associated degree of freedom fixed in that node. By convention, entry 1 in the third column represents the $x\ dof$, 2 denotes the $y\ dof$ and 3 implies the slope.
- Data file *voltbc.dat* contains the applied voltage information, where the first column is the count, the second column is the positive node, the third column is the negative node connection of DC source, the fourth column is the magnitude of applied DC and the fifth column is the ground reference for that DC source.

- Data file *thermbc.dat* contains the information for thermal boundary conditions, where the first column is the count, the second column is the node number, the third column is the imposed temperature and the fourth and fifth columns are the substrate and ambient temperatures, respectively.

- Material properties at reference temperature are stored in *elemprop.dat*. Upon loading data files, they will be copied to *elem.dat* file for each element. If the temperature dependence of material properties is provided for each element, the *elem.dat* columns containing material properties are updated according to the average temperature of that element.

- *forces.dat* contains the data for specified output, where the first column is the count, the second column is the node number for desired output, the third and fourth columns contain the direction of the output, for example [0,1] for x direction displacement, and the fifth column is the value of linear spring for resistance of the workpiece, k_s [$\mu N/\mu m$].

It should be noted that any arbitrary shape planar domain of frame elements generated externally can be used with this GUI, so long as the input information adheres to the format described above. After loading the input data files, boundary conditions appear in the display menu with the domain geometry. The triangles in red depict fixed x or y $dofs$ and the squares represent fixed slopes. The voltage and thermal boundary conditions are noted with text and the arrow in green shows the output direction of displacement.

Either in-plane widths or out of plane thicknesses can be chosen as variable for frame elements. Then the user is required to specify the lower and upper bounds on the chosen design variables for frame elements as shown in Figure A-4.

A.1.3 Optimization Module

Decisions on the optimization function and algorithm are made using the *Optimization* module, as shown in Figure A-5. The multi-criteria objective function proposed in this thesis is used as the primary choice but any other special case of objective function can easily be implemented as well. The user can specify the tolerance limit for convergence and the corresponding exponents of the objective function, as shown in Figure A-5.

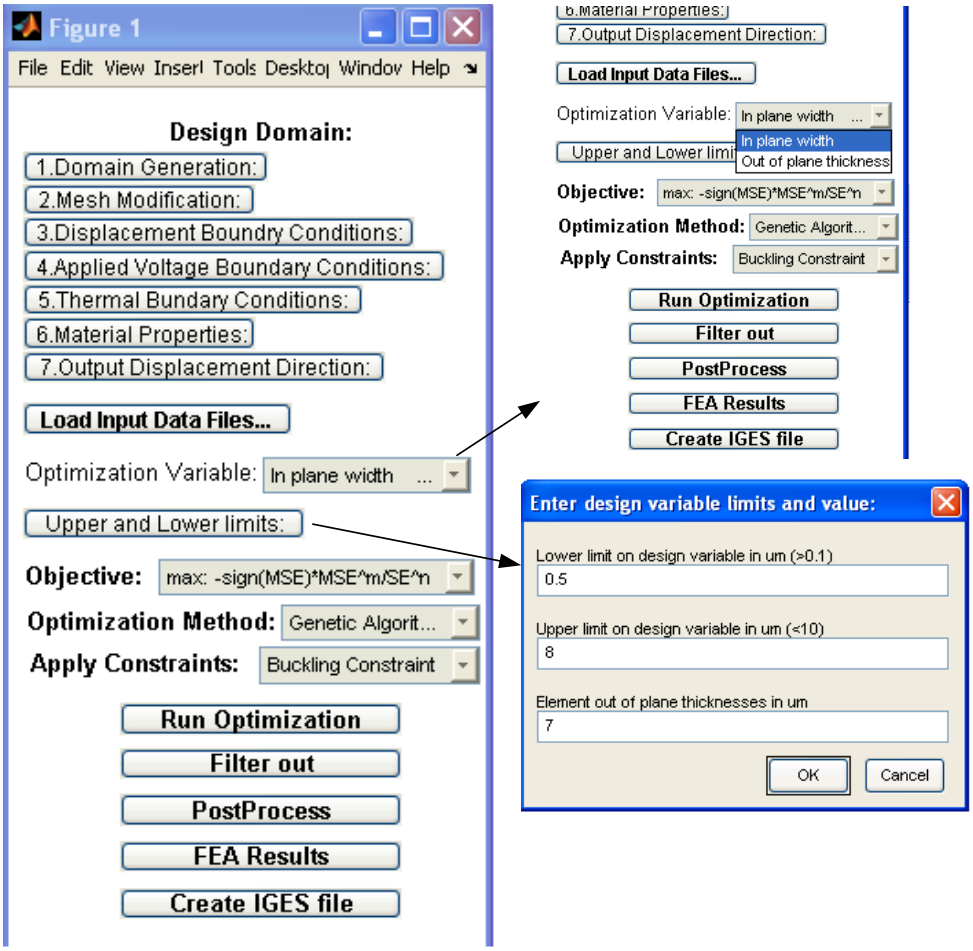

Figure A-4: Data processing module: loading the input data files, optimization variable and its upper and lower bounds.

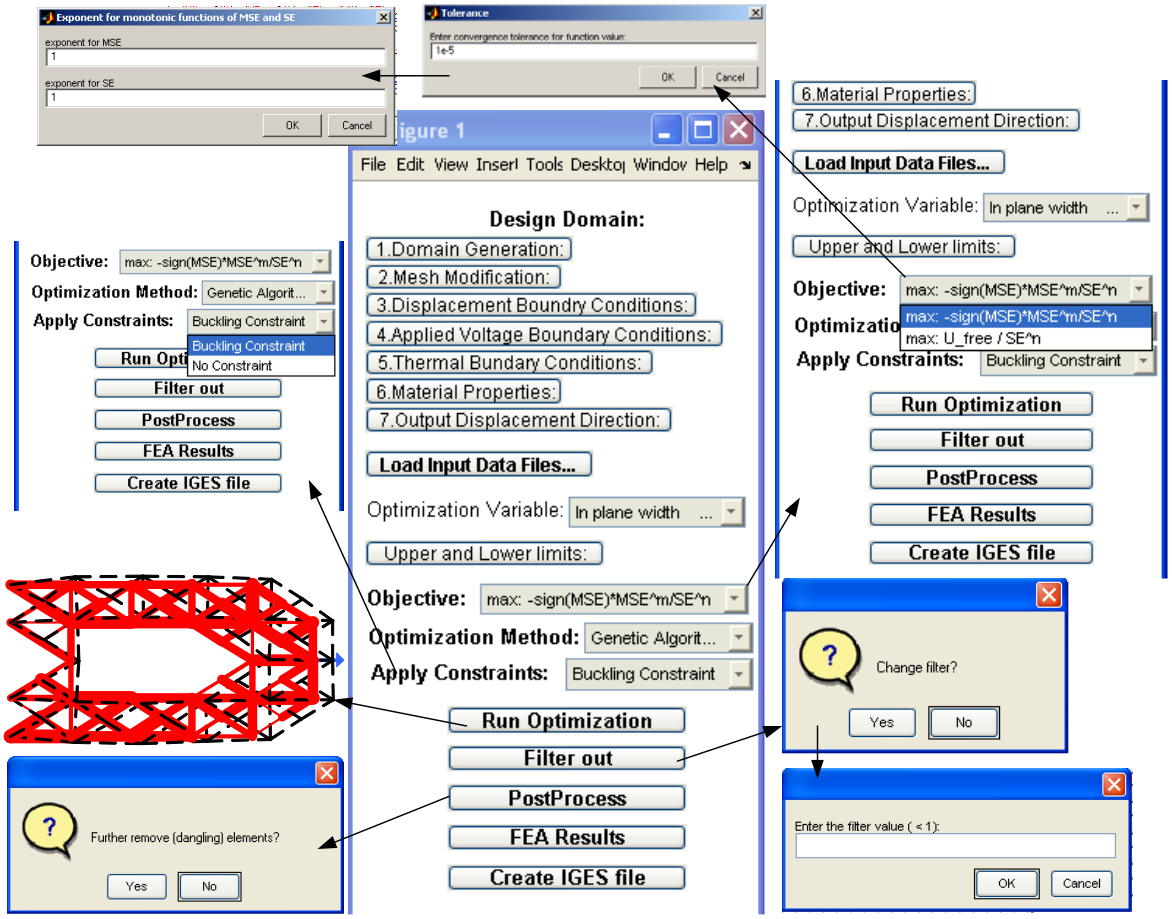

Figure A-5: Optimization module: choosing the optimization objective function, algorithm and applied constraints and also modifying the optimal solution using the post process options.

The preferred optimization algorithm is selected through the drop off menu in *optimization method.* Here, the real-coded GA is implemented but the GUI can accommodate more desired methods (e.g. SQP and optimality criteria method).

The active constraints are specified through selection in the drop off menu of *constraints.* In the default situation, the buckling constraint is active.

By hitting the *Run Optimization* button, the optimization algorithm starts iterating and, after convergence, the optimized configuration is plotted in the display menu. The finite element solution of the optimized design is superimposed in the display with dashed lines. After the algorithm converges, the convergence history is plotted in a graph and new topology data is saved in a new set of data files for further study. The genetic algorithm data for each population is stored in *GA.dat* file where the first column is the generation number, the second column is the fitness of that generation and the third column is the best fitness for each generation.

At this stage the elements on the lower bound are not shown in the display menu but are still not removed from finite element matrices and they can contribute to the stiffness matrix. In the *Filter out* menu, the user can specify the desired filtering coefficient, explained in Equation (5.22), to gauge the removal of elements considering the fabrication tolerances.

Some elements that do not offer significant contribution in improving the design objective may be retained in the optimal solution. They may exist alone without proper material connectivity in their neighborhood. It is then desired to eliminate those entities subject to user's discretion; however, through the study of many cases, it was observed that appearance of such dangling elements is very rare if the domain is properly defined. This is accomplished using the *Post Process* option in this module, as shown in Figure A-5.

If the performance of the modified solution is satisfactory, the final solution is saved in new set of data files. Elements outside specified bounds are permanently removed and node and element numbers are updated. The final design variables are stored in *x.dat* file for each element. The final optimized solution is analyzed using the *FEA Results* option. At this stage, the nodal solutions from the final finite element analysis are stored in the *FEA.dat* data file for further study.

In the *FEA.dat* file, the first column is the node number, x, y and slope of that node are stored in the second to fourth columns, the fifth column is the nodal voltage and the sixth

column is the nodal temperature. The nodal solutions are also plotted in separate graphs if desired. The optimized solution can now be transferred to a CAD or layout software.

A.1.4 Fabrication Module

The layout of the final optimized topology is transferred to IGES format in the *Fabrication* module, as shown in Figure A-6.

Initially, the elements are transported in the form of closed boxes with intersecting ends. This is done to facilitate the extrusion of such boxes if out-of-plane thicknesses are chosen as design variables. However, for in-plane-widths as design variables, for a large number of elements, trimming the edges in CAD software is a tedious task. An alternative, then, is to employ an edge detection algorithm on the image containing the optimal geometry. Such procedures are common and have been widely used as solid modelling interfaces [20]. The edge detection process is accomplished by scanning the binary image from left to right for each row. All pixels that are black in color are compared with neighboring pixels to determine if they lie on an edge. Pixels constituting the edges are retained as black while those in the interior are modified to white. The new image comprising the edge information is now scanned row-wise to locate a black pixel, which is an edge point. From this starting point, neighboring black pixels are located maneuvering clockwise. If the chaining process ends with the starting point, a closed loop is obtained. Otherwise, some open entities are found. Nevertheless, the connectivity information for individual entities is stored for further processing. Arc extraction is preferred over line extraction to avoid some circular arcs being modeled as multiple line segments. First from the connectivity data, three points (start, middle and end) are picked to retrieve the characteristic parameters of the arc, namely, its center and the radius. If a pixel lies on this arc, the arc is extended and the process is continued until the deviation violates a heuristically chosen threshold. The deviation here is the difference between the distance of the pixel from the center point and the radius. These arcs are stored in IGES format (center, start and end points). Second, from the remaining edge points, line extraction is performed by picking two pixels and fitting a candidate line. Deviations of each pixel from the line decide if the pixel lies on it. If so, the line is extended to the pixel and the procedure is continued until the deviation criteria is violated. The output is a collection of lines stored in the IGES

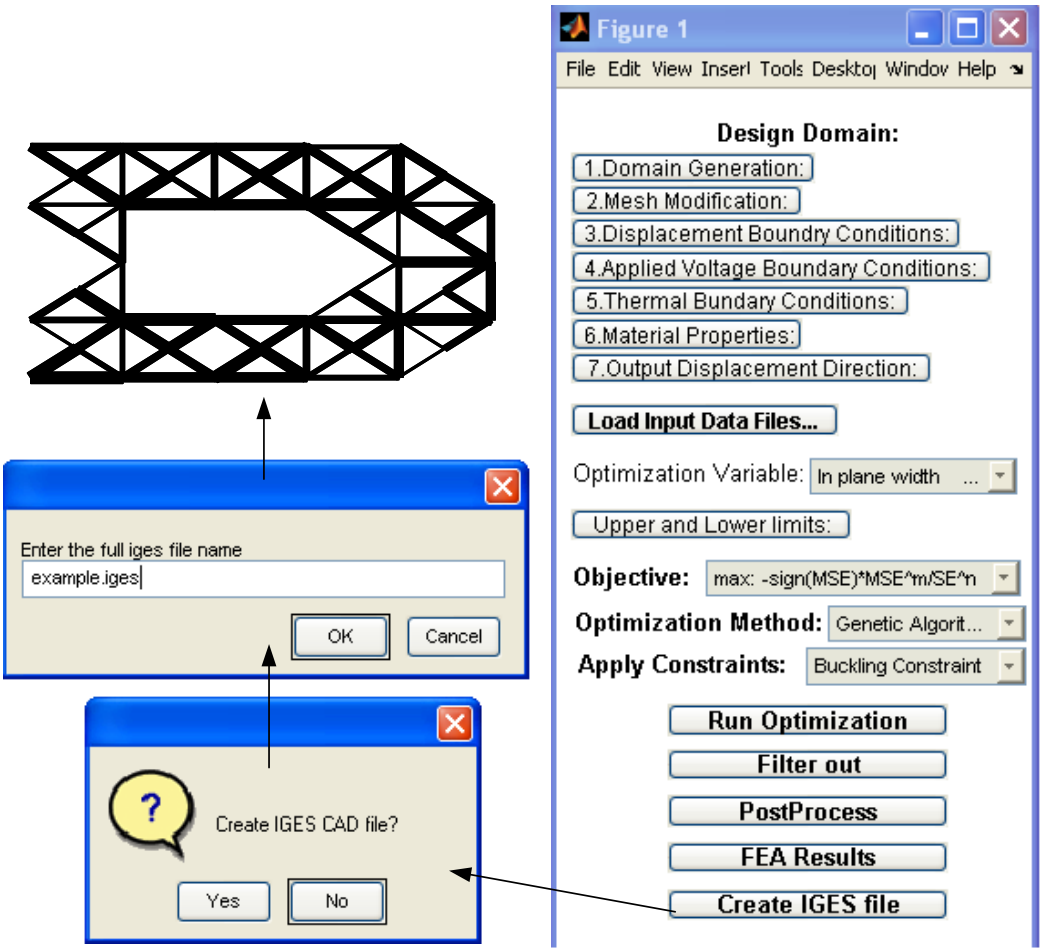

Figure A-6: Fabrication module: creating IGES CAD interface file for the optimal topology.

format (start and end point). Finally, a transportable wire frame for planar objects is obtained. Starting with the binary image, in pixmap or PM format, of the optimal compliant topology, edge detection is performed using the *edgerun* command in the optimization package to obtain a wire frame, as shown in Figure A-6. The corresponding IGES CAD file can be imported into any other package for solid model creation, fabrication and evaluating the performance of the optimized topology.

Bibliography

[1] M. I. Frecker, G. K. Ananthasuresh, S. Nishiwaki, and S. Kota, "Topological synthesis of compliant mechanisms using multi-criteria method," *Journal of mechanical design*, vol. 119, no. 2, pp. 238–245, 1997.

[2] M. I. Frecker, G. K. Ananthasuresh, S. Nishiwaki, and S. Kota, "Topology optimization of compliant mechanisms using the homogenization method," *INTERNATIONAL JOURNAL FOR NUMERICAL METHODS IN ENGINEERING*, vol. 42, pp. 535–559, 1998.

[3] Sridhar Kota, Joel Hetrick, Zhe Li, and Laxminarayana Saggere, "Tailoring unconventional actuators using compliant transmissions: Design methods and applications," *IEEE/ASME TRANSACTIONS ON MECHATRONICS*, vol. 4, no. 4, pp. 396–408, December 1999.

[4] Luzhong Tin and G. K. Ananthasuresh, "Vision based sensing of forces in elastic objects," *Sensors and Actuators A, Physical*, vol. 94, pp. 142–156, 2001.

[5] M. I. Frecker, G. K. Ananthasuresh, S. Nishiwaki, and S. Kota, "Optimal synthesis of compliant mechanisms to satisfy kinematic and structural requirements - preliminary results," in *Proceedings of The 1996 ASME Design Engineering Technical Conferences and Computers in Engineering Conference*, Irvine, California, August 18-22 1996, pp. DETC/DAC–1497.

[6] Ryan Hickey, Marek Kujath, and Ted Hubbard, "Heat transfer analysis and optimization of two-beam mircoelectromechanical thermal actuator," *Journal of vacuum science and technology*, vol. 20, no. 3, pp. 971–974, 2002.

[7] Michael J. Sinclair, "A high force low area mems thermal actuator," in *IEEE International Society Conference on Thermal Phenomena*, 2000, pp. 127–132.

[8] Ryan Hickey, Dan Sameoto, Ted Hubbard, and Marek Kujath, "Time and frequency response of two arm micromachined thermal actuators," *Journal of Micromechanics and Microengineering*, vol. 13, pp. 40–46, 2003.

[9] Luzhong Tin and G. K. Ananthasuresh, "A novel topology design scheme for the multi-physics problems of electr-thermally actuated compliant micromechanisms," *Sensors and Actuators A, Physical*, vol. 97, no. 98, pp. 599–609, 2002.

[10] Ole Sigmund, "Design of multiphysics actuators using topology optimization," *Computer methods in applied mechanics and engineering*, vol. 190, pp. 6577–6604, 2001.

[11] *ANSYS*, www.ansys.com, 11.0 edition, 2007.

[12] L. Que, J.-S. Park, and Y. B. Gianchandani, "Bent-beam electrothermal actuators for high force applications," in *Proceedings of the 1999 IEEE MEMS Conference*, Orlando, FL, January 1999, pp. 31–36.

[13] J. Jonsman, O. Sigmund, and S. Bouwstra, "Compliant electro-thermal micro actuators," in *12th IEEE international conference on MEMS*, Orlando, Florida, January 1999, pp. 588–593.

[14] Seok Heo, Gil Ho Yoon, and Yoon Young Kim, "Minimum scale controlled topology optimization and experimental test of a micro thermal actuator," *Sensors and Actuators A: Physical*, vol. 141, pp. 603–609, 2008.

[15] Larry L. Howell, *Compliant Mechanisms*, John Wiley and Sons, Inc., NewYork, NY, 1st edition, 2001.

[16] H. Samuels, "Single and dual axis micromechined accelerometers," *Analog Dialogue*, vol. 30, no. 4(1), 1993.

[17] F. Byers and A. Midha, "Design of a compliant gripper mechanism," in *Proceedings of the 2nd National Applied Mechanisms and Robotics Conference*, Cincinnati, Ohio, 1991, pp. XC.1–1 – XC.1–12.

[18] M. P. Bendsoe, "Generating optimal topologies in structural design using a homogenization method," *Journal of computer methods in applied mechanics and engineering*, vol. 71, pp. 197–224, 1988.

[19] Mary Irene Frecker, *Optimal Design Of Compliant Mechanisms*, Ph.D. thesis, University of Michigan, Ann Arbor, MI, 1997.

[20] M. Chirehdast, H. C. Gea, and N. Kikuchi, "Structural configuration examples of an integrated optimal design process," *ASME Journal of Mechanical Design*, vol. 116, pp. 997–1012, 1994.

[21] Sridhar Kota, Jinyong Joo, Zhe Li, Steven M. Rodgers, and Jeff Sniegowski, "Design of compliant mechanisms, applications to mems," *Analog Integrated Circuits and Signal Processing*, vol. 29, pp. 1–15, 2001.

[22] N. Yazdi, F. Ayazi, and K. Najafi, "Micromachined inertial sensors," *Proceedings of the IEEE*, vol. 86, no. 8, pp. 1640–1658, 1998.

[23] J. Suh, S. Glander, and R. Darling, "Omni directional ciliary micro actuator array for object positioning and inspection," in *Solid State Sensors and Actuators Workshop*, Hilton Head, South Carolina, June 2-6 1996.

[24] A. Saxena and G. K. Ananthasuresh, "Topology synthesis of compliant mechanisms using optimality criteria," in *7th AIAA/NASA Symposium on multidisciplinary Analysis and optimization*, St. Louis, MO, September 2-4 1998, AIAA98-4953.

[25] R. T. Haftka and Z. Gurdal, *Elements of Structural Optimization*, Kluwer Academic Publishers, Norwell, MA, 3 edition, 1992.

[26] R. T. Shield and W. Prager, "Optimal structural design for given deflection," *Journal of Applied Mathematics and Physics*, vol. 21, pp. 513–523, 1970.

[27] Anupam Saxena, *Topology optimization of gemetricaly nonlinear compliant mechanisms for flexibility stiffness and strenght*, Ph.D. thesis, University of Pennsylvania, 2000.

[28] Gang-Won Janf, Kyng Joo Kim, and Yoon Young Kim, "Integrated topology and shape optimization software for compliant mems mechanism design," *Advances in Engineering Software*, vol. 39, pp. 1–14, 2008.

[29] Kurt Maute and Dan M. Frangopol, "Reliability-based design of mems mechanisms by topology optimization," *Computers and Structures*, vol. 81, pp. 813–824, 2003.

[30] Kongtian Zuo, Yudong Zhao, Yongjun Xie, and Liping Chen, "Design mems actuators with topology optimization method," in *Proceedings of 1st IEEE International Conference on Nano/Micro Engineered and Molecular Systems*, Zhuhai, China, January 2006, pp. 1517–1522.

[31] Ruben Ansola, Estrella Vegueria, Javier Canales, and Jose A. Tarrago, "A simple enolutionary topology optimization procedure for compliant mechanism design," *Finite Elements in Analysis and Design*, vol. 44, pp. 53–62, 2007.

[32] Rajat Saxena and Anupam Saxena, "On honeycomb representation and sigmoid material assignment in optimal topology synthesis of compliant mechanisms," *Finite Elements in Analysis and Design*, vol. 43, pp. 1082–1098, 2007.

[33] Ole Sigmund, "Systematic design of micro actuators using topology optimization," in *SPIE Conference on Smart electronics and MEMS*, San Diego, California, March 1998, pp. 23–31.

[34] Ole Sigmund, "Topology synthesis of two-phase compliant actuators," in *proceedings of the 1999 ASME Design Engineering Technical Conferences*, Las Vegas, Nevada, September 1999, pp. 801–806.

[35] Ying Li, Kazuhiro Saitou, and Noboru Kikuchi, "Topology optimization of thermaly actuated compliant mechanisms considering time-transient effect," *Finite elements in analysis and design*, 2003.

[36] M. P. Bendsoe, *Optimization of structural topology, shape and material*, Springer, 1995.

[37] Ole Sigmund, *Toplogy optimization methods with applications in mechanism, MEMS and material design*, Ph.D. thesis, Technical University of Denmark, Denmark, 2000.

[38] A. Saxena and G. K. Ananthasuresh, "On an optimality property of compliant topologies," *Structural and multidisciplinary optimization*, vol. 19, no. 1, pp. 36–49, 2000.

[39] A. Saxena, "In persuit of optimal global compliant topologies," in *NaCoMM: national conference on machines and mechanisms*, Indian Institute of Technology, Kharagpur, December 21-23 2001.

[40] L. Saggere and S. Kota, "Static shape control of smart structures using compliant mechanisms," *AIAA Journal*, vol. 37, no. 5, 1999.

[41] G. Roach, "An investigation of compliant over running ratchet and pawl clutches," M.S. thesis, Brigham Young University, Provo, Utah, 1998.

[42] J. M. Derderian, L. L. Howell, M. D. Murphy, S. M. Lyon, and S. D. Pack, "Compliant parallel guiding mechanisms," in *Proceedings of the 1996 ASME Design Engineering Technical Conferences and Computers in Engineering Conference*, Irvine, California, August 18-22 1996, pp. DETC96 – MECH 1208.

[43] L. L. Howell, A. Midha, and M. D. Murphy, "Dimensional synthesis of compliant constant-force slider mechanisms," in *23rd ASME Biennial Mechanisms Conference*, 1994, vol. 71, pp. 509–515.

[44] G. K. Ananthasuresh and S. Laxminarayana, "A one piece compliant stapler 197," Tech. Rep. UN-MEAM 95-20, University of Michigan, Ann Arbor, MI, September 1994, Faculty Advisor: S. Kota.

[45] R. Yahya, "One piece compliant disk-drive loading mechanism," Capstone design project report, Mechanical Engineering and Applied Mechanics, University of Pennsylvania, Philadelphia PA, 1999.

[46] L. L. Howell, S. S. Rao, and A. Midha, "The reliability-based optimal design of a bistable compliant mechanism," *ASME Journal of Mechanical Design*, vol. 116, no. 4, pp. 1115–1121, 1994.

[47] S. T. Smith and D. Chetwynd, *Foundations of Ultra precision Mechanism Design, Developments in Nanotechnology*, vol. 2, Gordon and Breach Science Publications, 1994.

[48] A. Midha, T. W. Norton, and L. L. Howell, "On the nomenclature and classification of compliant mechanisms," in *ASME 1992 Design Technical Conference, 22nd Biennial Mechanisms Conference*, Scottsdale, Arizona, September 13-16 1992.

[49] Ole Sigmund, "On the design of compliant mechanisms using topology optimization," *Mechanics of structures and machines*, vol. 25, no. 4, pp. 495–526, 1997.

[50] T. Oden J, *Mechanics of Easatic Structures*, McGraw-Hill, New York, 1967.

[51] R. L. Barnett, "Minimum weight design of beams for deflection," *Journal of the Engineering Mechanics Division*, pp. 75–109, 1961.

[52] L. L. Howell and A. Midha, "A method for the design of compliant mechanisms with small-length flexural pivots," *ASME Journal of Mechanical Design*, vol. 116, no. 1, pp. 280–290, 1994.

[53] L. L. Howell and A. Midha, "Parametric deflection approximation for end loaded, large deflection beams in compliant mechanisms," *ASME Journal of Mechanical Design*, vol. 117, pp. 156–165, 1995.

[54] L. L. Howell and A. Midha, "Parametric deflection approximations for initially curved, large-deflection beams in compliant mechanisms," in *Proceedings of the 1996 ASME design technical conferences*, Irvine, CA, August 18-22 1996, DETC/MECH-1215.

[55] A. Saxena and S. N. Kramer, "A simple and accurate method for determining large deflections in compliant mechanisms subjected to end forces and moments," *ASME Journal of Mechanical Design*, vol. 120, no. 3, pp. 392–400, 1998.

[56] G. K. Ananthasuresh, *A new design paradigm for Micro-Electro-Mechanical Systems and Investigations on the Compliant Mechanism Synthesis*, Ph.D. thesis, University of Michigan, Ann Arbor, MI, 1994.

[57] G. K. Ananthasuresh, S. Kota, and Y. Ginanchandani, "Systematic synthesis of micro-compliant mechanisms-preliminary results," in *Proceedings of the 3rd national conference on applied mechanisms and robotics*, Cincinnati, November 1993, vol. 2.

[58] G. K. Ananthasuresh, S. Kota, and Y. Ginanchandani, "A methodical approach to the design of compliant micromechanisms," in *Solid state sensors and actuators workshop*, Hilton Head, FL, 1994, pp. 189–192.

[59] G. K. Ananthasuresh, S. Kota, and N. Kikuchi, "Strategies for systematic synthesis of compliant mems," in *Proceedings of the 1994 ASME Winter Annual Meeting*, Chicagi, IL, November 1994, pp. 677–686.

[60] U. D. Larsen, O. Sigmund, and S. Bouwstra, "Design and fabrication of compliant mechanisms and material structures with negative poisson's ratio," *Journal of Microelectromechanical Systems*, vol. 6, no. 2, pp. 99–106, 1997.

[61] N. Huang, "Principle of stationary mutual complementary energy and its application to optimal structural design," *Journal of applied methods in physics*, vol. 22, pp. 609–620, 1971.

[62] S. Nishiwaki, S. Min, S. Ejima, and N. Kikuchi, "Structural optimization considering flexibility," *JSME International Journal*, vol. 41, no. 3, pp. 476–484, 1998.

[63] J. A. Hetrick and S. Kota, "An energy formulation for parametric size and shape optimization of compliant mechanisms," *Journal of Mechanical Design*, vol. 121, pp. 229–234, 1999.

[64] A. Saxena and G. K. Ananthasuresh, "An optimality criteria approach for the topology synthesis of compliant mechanisms," in *Proceedings of the DETC'98, ASME Design Engineering Technical Conference*, Atlanta, Georgia, Septmeber 13-16 1998, DETC98/MECH-5937.

[65] J. A. Hetrick, N. Kikuchi, and S. Kota, "Robustness of compliant mechanism topology optimization formulations," in *Proceedings of SPIE conference on mathematics and controls in smart structures*, New Port Beach, California, March 1999, pp. 244–254.

[66] A. Saxena and G. K. Ananthasuresh, "Topology design of compliant mechanisms with strength considerations," *Mechanics of Structures and Machines*, vol. 29, pp. 199–222, 2001.

[67] U. Kirsch and G. I. N. Rosvany, "Design considerations in the optimization of structural topologies," *Optimization of large structural systems*, vol. 1, pp. 121–138, 1993.

[68] M. I. Frecker, S. Kota, and N. Kikuchi, "Use of penalty function in topological synthesis and optimization of strain energy density of compliant mechanisms," in *Proceedings of the ASME Design Engineering Technical Conferences*, Sacramento, California, August 18-22 1997, pp. DETC97/DAC–3760.

[69] G. N. Vanderplaats, *Numerical Optimization Techniques for Engineering Design: with applications*, McGraw-Hill, New York, 1984.

[70] K. Svanberg, "The method of moving asymptotes - a new method for structural optimization," *International journal for numerical methods in engineering*, vol. 24, pp. 359–373, 1987.

[71] David E. Goldberg, *Genetic algorithms in search, optimization and machine learning*, Addison-Wesley Publishing Co., Reading, MA, 1989.

[72] J.a L. Nowinski, *Theory of thermoelasticity with applications*, Sijthoff and Noordhoff International Publishers, Netherlands, 1978.

[73] Tirupathi R. Chandrupatla and Ashok D. Belegundu, *Introduction to Finite Elements in Engineering*, Prentice Hall, New Jersey, 3rd edition, 2002.

[74] M. Asghar Bhatti, *Fundamental Finite Element Analysis and Applications*, Wiley, NewYork, NY, 1st edition, 2005.

[75] *MATLAB*, www.mathworks.com, 7.0 edition, 2004.

[76] O. Sigmund and A. R. Diaz, "checkerboard patterns in layout optimization," *Structural Optimization*, vol. 10, pp. 40–45, 1995.

[77] David A. Koester, Ramaswamy mahadevan, Busbee Hardy, and karen W. Markus, *PolyMUMPs Design Handbook*, MEMSCAP, 10th edition, 2003.

[78] Jiri Vlach and Kishore Singhal, *Computer methods for circuit analysis and design*, Van Nostrand Reinhold, New York, N.Y., 2nd edition, 1994.

[79] Jiri Vlach, *Basic Network Theory with Computer Applications*, Van Nostrand Reinhold, New York, N.Y., 1992.

[80] J. K. Lou, A.J. Flewitt, S. M. Spearing, and N. A. Fleck, "Comparison of microtweezers based on three lateral thermal actuator configurations," *Journal of Micromechanics and Microengineering*, vol. 15, pp. 1294–1302, 2005.

[81] F. Incorpera et al, *Fundamentals of Heat and Mass Transfer*, Wiley, New York, 1990.

[82] Jack P. Holman, *Heat Transfer*, McGraw-Hill, Columbus, OH, 8th edition, 1997.

[83] Kythe Wei, *An introduction to Linear and Nonlinear Finite Element Analysis, A computational approach*, Birkhauser Boston, Boston, 2004.

[84] Tai-Ran Hsu, *The finite element method in Thermomechanics.*

[85] C. H. Mastrangelo, *Thermal applications of microbridges*, Ph.D. thesis, U. C. Berkeley, Berkeley, CA, 1991.

[86] L. Lin and Mu Chiao, "Electrothermal response of lineshape microstructures," *Sensors and Actuators A*, vol. 55, pp. 34–41, 1996.

[87] Ph. Lerch, C. Kara-Slimane, B. Romanowicz, and Ph. Renaud, "Modelization and characterization of assymetrical thermal micro actuators," *Journal of Micromechanics and Microengineering*, vol. 6, pp. 134–137, 1996.

[88] D. Iesan and A. Scalia, *Thermoelastic Deformations*, Kluwer Academic Publishers, London, 1996.

[89] Robert M. Jones, *Buckling of Bars, Plates, and Shells*, Bull Ridge Publishing, Blacksburg, Virginia, 2006.

[90] Akos Sapkas and Laszlo Kollar, "Buckling of beams with low shear stiffness," in *2nd Internatnal Symposium in Civil Engineering*, Budaest, 1998.

[91] Zbigniew Michalewicz, *Genetics Algorithms + Data Structures = Evolution Programs*, Springer-Verlag, New York, 2nd edition, 1998.

[92] J. Joines and C. Houck, "On the use of non-stationary penlty functions to solve constrained optimization problems with genetic algorithms," in *IEEE International symposium Evolutionary Computation*, Orlando, FL, 1994, pp. 579–584.

[93] J. A. Joines C. R. Houck and M. G. Kay, "A genetic algorithm for function optimization: a matlab implementation," NCSU-IE Technical Report 9509, North Carolina State University, 1995.

[94] J. Jonsmann and O. Sigmund, "Compliant thermal microactuators," *Sensors and actuators A, Physical*, vol. 76, pp. 463–469, 1999.

[95] J. Jonsmann, *Technology development for topology optimized thermal microactuators*, Ph.D. thesis, Technical University of Denmark, Microelektonic Center MIC, December 1999.

[96] Ole Sigmund, *TOPOPT*, http://www.topopt.dtu.dk.

[97] G. I. N. Rozvani, M. Zhou, and O. Sigmund, *Topology Optimization in Structral Design*, Chapman and Hall, London, 1994.